IRAQI JOURNAL OF APPLIED PHYSICS

The *Iraqi Journal of Applied Physics (IJAP)* is a peer reviewed journal of high quality devoted to the publication of original research papers from applied physics and their broad range of applications. IJAP publishes quality original research papers, comprehensive review articles, survey articles, book reviews, dissertation abstracts in physics and its applications in the broadest sense. It is intended that the journal may act as an interdisciplinary forum for Physics and its applications. Innovative applications and material that brings together diverse areas of Physics are particularly welcome. Review articles in selected areas are published from time to time. It aims to disseminate knowledge; provide a learned reference in the field; and establish channels of communication between academic and research experts, policy makers and executives in industry, commerce and investment institutions. IJAP is a quarterly specialized periodical dedicated to publishing original papers, letters and reviews in: Applied & Nonlinear Optics, Applied Mechanics & Thermodynamics, Digital & Optical Communications, Electronic Materials & Devices, Laser Physics & Applications, Plasma Physics & Applications, Quantum Physics & Spectroscopy, Semiconductors & Optoelectronics, and Solid State Physics & Applications

SPONSORED AND PUBLISHED BY

THE IRAQI SOCIETY FOR ALTERNATIVE AND RENEWABLE ENERGY SOURCES & TECHNIQUES (I.S.A.R.E.S.T.)

IRAQI JOURNAL OF APPLIED PHYSICS
" INSTRUCTIONS TO AUTHORS "

CONTRIBUTIONS

Contributions to be published in this journal should be original research works, i.e., those not already published or submitted for publication elsewhere, individual papers or letters to editor.

SUBMISSION OF MANUSCRIPTS

Manuscripts should be submitted to the editor at the mailing address:

Iraqi Journal of Applied Physics
Editorial Board
P. O. Box 55259, Baghdad 12001, IRAQ, submission@ijap.org , editor@ijap.org

MANUSCRIPTS

Two hard copies with soft copy on a compact disc (CD) should be submitted to Editor in the following configuration:

- Double-spaced one-side A4 size with 2.5 cm margins of all sides
- Times New Roman font (16pt bold for title, 14pt bold for names, 12pt bold for headings, 12pt regular for text)
- Letters should not exceed 10 pages, papers should not exceed 20 pages and reviews are up to author.
- Manuscripts presented in English only are accepted.
- English abstract not exceed 150 words
- 4 keywords (at least) should be maintained on (PACS preferred)
- Author(s) should express all quantities in SI units
- Equations should be written in equation form (*italic* and symbolic)
- Figures and Tables should be separated from text
- Figures and diagrams can be submitted in colors for assessment and they will be returned to authors after provide printable copies
- Charts should be indicated by the software used for
- Only original or high-resolution scanner photos are accepted
- For electronic submission, articles should be formatted with MS-Word software.

AUTHOR NAMES AND AFFILIATIONS

It is IJAP policy that all those who have participated significantly in the technical aspects of a paper be recognized as co-authors or cited in the acknowledgments. In the case of a paper with more than one author, correspondence concerning the paper will be sent to the first author unless staff is advised otherwise.

Author name should consist of first name, middle initial, last name. The author affiliation should consist of the following, as applicable, in the order noted:

- Company or college (with department name or company division)
- Postal address
- City, state, zip code
- Country name
- Telephone, and e-mail

REFERENCES

The references should be brought at the end of the article, and numbered in the order of their appearance in the paper. The reference list should be cited in accordance with the following examples:

[1] X. Ning and M.R. Lovell, "On the Sliding Friction Characteristics of Unidirectional Continuous FRP Composites", *ASME J. Tribol.*, 124(1) (2002) 5-13.
[2] M. Barnes, "Stresses in Solenoids", *J. Appl. Phys.*, 48(5) (2001) 2000–2008.
[3] J. Jones, "Contact Mechanics", Cambridge University Press (Cambridge, UK) (2000), Ch.6, p.56.
[4] Y. Lee, S.A. Korpela and R. Horne, "Structure of Multi-Cellular Natural Convection in a Tall Vertical Annulus", Proc. 7th International Heat Transfer Conference, U. Grigul et al., eds., Hemisphere (Washington DC), 2 (1982) 221–226.
[5] M. Hashish, "Waterjet Technology Development", High Pressure Technology, PVP-Vol. 406 (2000), 135-140.
[6] D.W. Watson, "Thermodynamic Analysis", ASME Paper No. 97-GT-288 (1997).
[7] C.Y. Tung, "Evaporative Heat Transfer in the Contact Line of a Mixture", Ph.D. thesis, Rensselaer Polytechnic Institute, Troy, NY (1982).

PROOFS

Authors will receive proofs of papers and are requested to return one corrected hard copy with a WORD copy on a compact disc (CD). New materials inserted in the original text without Editor permission may cause rejection of paper.

COPYRIGHT FORM

Author(s) will be asked to transfer copyrights of the article to the Journal soon after acceptance of it. This will ensure the widest possible dissemination of information.

OFFPRINTS

Authors will receive offprints free of charge and any additional offprints can be ordered.

SUBSCRIPTION AND ORDERS

Annual fees (4 issues per year) of subscription are:

- 50 US$ for individuals inside Iraq.
- 100 US$ for establishments inside Iraq.
- 100 US$ for individuals abroad.
- 200 US$ for establishments abroad.

Fees are reduced by 25% for I.S.A.R.E.S.T. members. Orders of issues can be submitted by contacting the editor-in-chief or editorial office at **subscription@ijap.org** to maintain the address of issue delivery and payment way.

Invited Paper

Generation of Highly-Directed Laser-Driven Plasma Blocks for Light Ion Beam Fusion Applications

Harikawa Hora[1]
Francis Osman[2]
Yu Liang Cang[2]

[1] *Department of Theoretical Physics University of New South Wales Sydney 2052, Australia*
[2] *School of Quantum Methods and Mathematics Science, University of Western Sydney, Penrith 1797, Australia*

It is being clarified why the observations of plane wave geometry interaction within the skin depth of a laser irradiated target are very unique exceptions from the broad stream of the usual experiments of laser plasma interaction. This permits a much more simplified description by plane wave interaction theory for laser pulses of about ps or shorter duration and powers above TW and simplifies computations in contrast to the usual cases with relativistic self-focusing. After establishing theoretically and experimentally the generation of highly directed plasma blocks with ion current densities above 10^{10} A/cm^2 moving against the laser light or into the target, applications for laser fusion, and a completely new improvement of ion sources for the next generation of accelerators are discussed.

Keywords: Laser fusion, Self-focusing, Ponderomotive force, Controlled fusion
Received: 08 January 2010

1. Introduction

It is a rare opportunity how very marginal and very little noted experimental and theoretical developments within the broad stream of the established research may contribute to result in a chance for solving the energy production by nuclear fusion in some alternative ways by application of lasers. The key element for this development is the chirped pulse amplification (CPA) pioneered by Gerard Mourou [1] of laser pulses reaching today more than PW (10^{15}W) power with pulses of ps or shorter duration. Another technique uses excimer lasers pioneered by Fritz-Peter Schäfer [2]. The other ingredients are the unique measurements with TW-ps laser pulses beginning with the observation of Doppler shifts from irradiated targets by Roland Sauerbrey [3], the anomalies of x-ray emission from targets clarified by most precise studies of the influence of prepulses by Jie Zhang et al [4] and the very transparent measurements of ion generation in comparison with longer pulses by Jan Badziak et al [5].

The uniqueness of these observations consists in the discovery of the fundamental difference to the entire broad stream observations leading to relativistic self-focusing dominates the interaction, where MeV to GeV highly ionised ions are generated with intense electron beams of 100MeV and higher energy, electron positron pairs while 10MeV gammas produce unusual nuclear reactions. In contrast to this, the suppression of relativistic self-focusing in the unique experiments permitted a comeback to the transparent and simplified theory of plane wave interaction of the laser pulse as a skin layer process [6]. A consequence is indeed that these unique conditions may lead to a new scheme for laser fusion. The basically new aspects for ion sources for feeding accelerators may provide a one new ingredient for planning the design of the next generation of accelerators after the large hadron collider (LHC) [7].

The struggle with the usual broad stream observations is well known where the discovery of nonlinear effects, of relativistic phenomena and even of a quantum mechanical component to the otherwise classical plasma phenomena was dominating [8,9] apart from several misleading considerations of resonance absorption and overestimation of parametric instabilities which processes could mostly be excluded experimentally by laser beam smoothing and where some explanations were given from the observation of 10-ps stochastic pulsation processes.

2. Historical Summary on Laser Driven Ion Emission

The measurement of ion energies and high current densities from laser irradiated targets in vacuum was the first experience of the very unexpected and extreme anomalies in this new field of laser-plasma interaction physics after the clean Q-switch laser pulses were available in 1962. If laser powers of less than about 1MW

 ISSN 1813-2065 Printed in IRAQ

was incident, all was classical [10], the generated plasmas behaved fully thermodynamically with ion energies between 2 and 5eV according to the generated temperatures of few ten thousand degrees. The electrical current densities of the emitted ions were about 100mA/cm^2 as known form the classical Child-Langmuir space charge limitation which dominates all emission processes including the most advanced MEVVA or ECR sources [6]. In contrast to this, as soon as the laser power P exceeded a threshold P^*

$$P>P^*= 1 \text{ MW} \qquad (1)$$

The electron emission current density was more than ten thousand times higher [12] and the energy of the ions was not few eV but few keV [13]. This was the starting point for the studies of the anomalous processes of laser-plasma interaction [14]. It led finally to the measurement of MeV ions [15,16] where the discovery of Ehler [15] has to be underlined that there were three groups of ions the fastest group the second fastest group and the unavoidably remaining thermal plasma. A clear reproduction of the three groups from irradiated silver can be seen in Fig. (2a). The second group was reported explicitly in the summary of Gitomer [18] where the special property of this type of fast ions found special attention [19] with respect to a proof of the a quantum modification of the collision frequency [20].

2.1 The Fastest Ion Group

The highly charged ions of 10keV and higher energy from laser produced plasmas with laser pulses of higher power than 1MW were separated in groups with linear increase of the ion energy on the charge number *Z*. The measured number of 10^{13} and many more ions is too large than an explanation can be given by an ambipolar acceleration from the Debye surface sheath which could account only to about 10^9 ions at the most. When looking into other acceleration mechanisms, self-focusing was an explanation [21] based on the first derived dielectric modification of the ponderomotive force generalized to the nonlinear force [8,9,22], Three conditions had to combined: (a) the fact that the radial nonlinear force $-\nabla \boldsymbol{E}^2$ with the averaged electric laser field $\boldsymbol{E}$ acting on the plasma radial in the laser beam will be compensated by gas dynamic $-p$ of the pressure p due to depletion of plasma from the beam center, (b) the dielectric bending and total reflection of the plasma beamlets in the filament, and (c) the diffraction conditions of the beam. The result is that self-focusing appears above a laser power *P* of about 1 MW. This process including the beam diameter and the measurements of the plasma depletion in the beam axis was measured in all details in agreement [23] with the theory derived later by a number of authors in a different way and all resulting in the same numbers [8].

This showed how the MW threshold of Eq. (1) led to a laser intensity in the filament such that that the nonlinear force accelerated the whole volume of the electron cloud with the attached ions, but separated by *Z*, to the 10keV energies. This process to the electron cloud with the strong gradient of the electromagnetic laser field energy [22] including the dielectric properties was like gravitation but with differentiating according to *Z*.

Apart from this plasma dynamics driven by the laser field above 1MW, another *instantaneous* self-focusing appeared purely dielectric when the quiver energy of the electrons in the laser field were at least about one thousandth of the relativistic electron energy (mc^2) [20]. The laser beam was shrinking down to a diameter of multiples δ of the laser wavelength (λ). The extremely high laser intensities in the filament resulted than in a nonlinear force acceleration to the MeV energies. This agreed with all the highest ion energies measured all different times at different laboratories [19] before the ps laser pulses were available. The maximum ion energy ε_{ion} is then independent of the wavelength λ and is determined only by the laser power *P* in watts as [24.25]

$$\varepsilon_{trans} = \frac{Zmc^2 Pe^2}{\pi^2\delta^2 m^2 c^5} = 5.7\times10^{-12}(W)Zmc^2\left(\frac{P}{\delta^2}\right) \qquad (2)$$

where δ is a self diffraction factor given in multiples of the wave length which may vary around one wavelength (δ=1) though there were experimental indications that this can be as low as 0.6 [8]. Since we have to compare ion energies differing by orders of magnitude in the following, we do not need to go into the finer accuracy and error bars of the experiments.

One example from recent experiments with the PALS iodine laser [26] are the following. A third harmonics iodine laser pulse of 0.4ns duration and 6x10^{11}W power irradiating tantalum produced fastest 81MeV Ta^{+50} ions. The theory of relativistic self-focusing, Eq. (2) with δ=1 arrives at 89MeV. This is a rather sufficient confirmation that the very fast ions were produced by relativistic self focusing and subsequent nonlinear force acceleration.

2.2 The Second Fastest Ion Group

For the second fastest ion group it was explained before from the observed properties [19] that this may be due to the *partial thermalization* of the high electron quiver energy where a subsequent acceleration process of these

hot plasma electrons will occur. After this thermalization, the ions gain energy by ambipolar acceleration, however, to much higher energies and ion numbers than from the thermal plasma. The ion numbers are still less than that of the fastest ion group due to relativistic self-focusing. In this view, the long known phenomenon of the "hot electrons" discovered from x-ray emission by Eidmann [8,14] led to the consideration of a thermo-kinetic description [6,19] where the nonlinear phenomenon involved is the quiver motion of the electron in the laser field.

The detailed study of this group of ion emission as a "quiver-thermalization" process is of special interest be-cause this leads to another proof of the *quantum modification* of the plasma collisions as it was successful initially to reproduce the measured hot-electron caused x-ray emission [19]. This question is important also for understanding of the mechanisms at magnetic confienement fusion [8]. The degree of thermalization of the energy of the quivering electrons was studied depending on the collision frequency. We used the quantum modified collision frequency [20]

$$\nu = \begin{cases} \nu_c \\ \nu_c T / T^* \end{cases} \qquad (3)$$

where ν_c is the classical electron-ion collision frequency, T is the plasma temperature and

$$T^* = 4Z^2 mc^2 \alpha / 3K = Z^2\ 36.9 \text{ eV} \qquad (4)$$

The use of this result for explaining the measured diffusion in stellarators or the thermal conduction in tokamaks has been show before [8,9,20].

The hot temperature T_x measured also by the high energy x-ray emission in the plasmas at laser radiation during a laser pulse length τ_L is then given in the range of quantum domination [19] by

$$T_x = \text{const. } \tau_L I^{1/2} \qquad (5)$$

while the use of the classical collision frequency arrives at

$$T_x \propto I^{1/2} \qquad (6)$$

The evaluation of the numerous results compiled by Gitomer et al [18] indicated that the measured x-ray temperature followed Eq. (5) with the positive exponent 1/2 and not with the negative exponent of the classical dependence on the laser intensity ***I***.

This result can now be extended to the ps laser plasma interaction experiments by Clark et al [28]. 50TW 0.9-2.3ps neodymium glass laser pulses were focused to 10 wavelength beam diameter at an obliquely arranged target where strong suppression of any prepulse produced plasma in front of the target of less then 10 wavelength thickness. The highest energies of Pb^{+48} was 430MeV while the fastest C^{+6} ions had 60MeV energy. The fact that the lead ions should have 7.1GeV and the carbon ions about 880MeV energy if relativistic self-focusing had been involved (Eq. (2)), indicates that the ions were rather not due to relativistic self-focusing. The conditions of the 10 wavelength focus and the thin pre-plasma may indicate qualitatively that relativistic self-focusing could not have been established but that the quantum modified quiver-thermalization process (hot electron acceleration) is driving the ions.

It is very important to note that the measurement of the intensity dependence (Fig. 4 of Ref. [28]) at the unchanged wavelength showed an increase of the maximum ion energy ε_{imax} of the fastest ions is close to

$$\varepsilon_{imax} \propto I^{1/2} \qquad (7)$$

This is in rather good agreement with Eq. (5) since the pulse duration was constant. This may be a confirmation that the measured fast ions were only due to the quiver-collision-thermalization process as known from the usual second fastest ion group because the relativistic self-focusing relation, Eq. (2) would have had an exponent 1 and not 0.5 as measured [28]. Obviously there was not at all the fastest ion group from relativistic self-focusing but only from the quiver-collision mechanism as known from the usual second fastest ion group.

2.3 Other Usual Observations

The complexity of the laser plasma interaction as observed in all the large number of usual cases in the past can not immediately classified as it was possible with the MeV ion generation. The fact that neither resonance absorption nor the long assumed parametric instabilities are dominating, could be seen when the laser beam smoothing [29] was introduced. This smoothing was reducing the generation of 3/2 harmonics and other parameters which were assumed to be related to the instabilities by more than a factor 100 [30]. On the other hand, smoothing was increasing direct drive fusion gains by more than a factor 10 [31]. It was revealed that the complexity of the interaction was mainly due to a 10 to 30ps stochastic pulsation of the interaction as measured directly [32] and that this was due to nonlinear force produced density ripples by the partial standing waves and their thermal relaxation such that the broad band smoothing of the random phase plate smoothing immediately could lead to the suppression of the phase reflection from the ripples as clearly reproduced numerically [33].

The phenomena at the use of ps and short pulses at laser powers above TW lead to another order of complications where, however, relativistic self-focusing was well of importance. The generation of 30MeV electrons of large

 ISSN 1813-2065 Printed in IRAQ

numbers (10^8) per irradiation with 30TW ps laser pulses [34] could immediately explained by a free wave electron acceleration including relativisitic self focusing [35]. Observations of ions of half GeV energy were just mentioned [28] while the generation of very intense proton beams of 5MeV [36] may be used for spark ignition in laser compressed deuterium-tritium (DT). For the first time, large numbers of positrons were generated [37], the generation of very intense short pulses of gamma radiation led to nuclear photo-effect and radioactive isotopes [38] including reaction for the elimination of long lived nuclear waste [39]. The involvement of relativistic self-focusing in most of these cases did not simplify the theoretical clarification of these processes while in the experiments of fast ignition for laser fusion, the involvement of relativistic self-focusing was an essential ingredient [40].

3. Interaction without Relativistic Self-Focussing

In view of the partially clarified and the unclarified phenomena just mentioned, the following discussion is about few cases out of the usual main stream of the laser plasma interaction research which cases were rare and differ significantly and may be categorized as *unique*. They may even be described as being based on much more simplified conditions of plane geometry mostly due to the fact that relativistic self-focusing could be excluded leading to a more transparent modelling despite all the numerous confusing aspects which are known form the usual research.

The key question is whether there are conditions that the interaction of a focussed laser beam at the surface of a solid target in vacuum is following the conditions of a plane wave interaction described preferably one dimension, or whether the laser beam – as in most of the usual cases enters - a pre-generated plasma in front of the target, performs self -focusing and undergoes a very complicated shrinking to wavelength diameter beamlets with subsequent enormous nonlinear forces for producing MeV to GeV ions and strong x-ray emission. The plane wave interaction was studied by hydrodynamic codes including nearly all realistic and general plasma properties [8,14] of which one of the numerous cases is shown in Fig. (1). Within two ps interaction of a 10^{18}W/cm^2 pulse on a deuterium target with an initially very low reflection (bi-Rayleigh) density profile, the nonlinear force is generating blocks of plasma of several vacuum wave lengths thickness with velocities exceeding 10^9cm/s moving against the laser light and a similar block moving into the target interior.

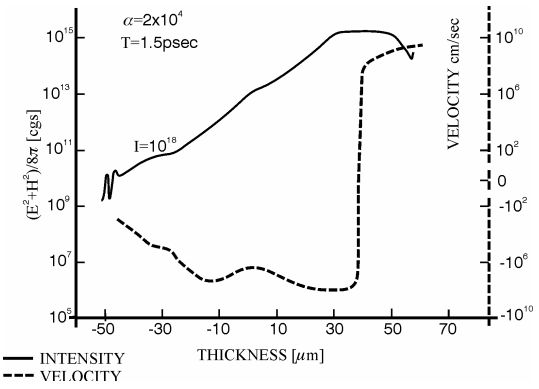

Fig. (1) Generation of blocks of deuterium plasma moving against the neodymium glass laser light (positive velocities v to the right) and moving into the plasma interior (negative velocities) at irradiation by a neodymium glass laser of 10^{18} W/cm^2 intensity onto an initially 100eV hot and 100μm thick bi-Rayleigh profile (Fig. 10.17 of [8]) with minimum internal reflection. The EM energy density $(E^2+H^2)/(8\pi)$ is shown at the same time of 1.5ps after begin of the constant irradiation [8]

It was many years later that such velocities gained by irradiation of similar excimer laser intensities at less than picosecond duration did produce such velocities as measured in all details from the Doppler shift by Sauerbrey [3]. The resulting accelerations were in full agreement with the expectation from the nonlinear force interaction. Another key experiment was that by Zhang et al. [4] where 100fs TW laser pulses were focused to about 30 wave lengths diameter onto a target and the x-ray emission was measured. The laser pulses produced very much lower x-rays than known from other experiments with the same intensities. The uniqueness of the experiment [4] consists in the procedure, that a lower intensity similar pulse was irradiated on the target at varying times between 10 to 100ps *before* the main pulse. At short time pre-irradiation, no change of the low x-ray emission was seen, but as soon as the pre-pulse time reached 70ps and more, suddenly the very high x-ray emission appeared as known from all the usual main stream experiments. The later given explanation was evident: thanks to the clean laser pulse technique [4] where the contrast ratio for the main pulse was 10^8 (ratio of suppression of any pre-pulse). When the 70ps prepulse was incident, a plasma plum was generated of a depth about two times the focus diameter. This was sufficient that the main pulse was shrinking to about one wave length diameter by relativisitc self-focusing such that the then very high x-ray intensities resulted as in the usual cases.

These both experiments [3,4] were a clear confirmation of the plane wave plasma interaction, in agreement with the plane wave interaction theory, Fig. 1, and the exclusion of

the self-focusing theory [8,24,25] would not have been very intriguing. The drastic problems appeared with the experiments by Badziak et al [5] from the studies of ion emission with high contrast ratio ps-TW laser pulses. This mutually confirmed the high contrast ratio of the excimer laser pulses [3] as well as the very clean techniques of the other experiments [4,5]. The experiments [5] with copper target should have led to Cu^{+13} ion of 22MeV due to relativistic self focusing, but only 0.5MeV ions were detected. Furthermore it was strange that the *number of the fast ions did not change* at all when the laser intensity was varying by a factor 30 while the energy of the fast ions was fully linear on the laser intensity as expected from a nonlinear force acceleration. The measured x-ray emission leading to a quiver energy swelled dielectrically by a factor three fully satisfactorily explained the measured ion energies from a plane wave interaction which was taking place within the skin depth of intensity of independent volume. This confirmed the observation of the intensity independence of the fast ions. These experiments were repeated with gold targets confirming all the details of the skin layer mechanism [11] including the generation of the plasma block moving into the target as experimentally confirmed from thin irradiated films [41] and confirming an ion current density in the blocks above $j>10^{10}$A/cm^2.

The measurements confirmed also [11] that the ps-TW interaction resulted only in one narrow ion beam accelerated against the laser light as expected from the nonlinear force acceleration while the use of longer laser pulses as usually resulted in several groups of ions moving into a wide angle against the laser light [25] (see Fig. 4 of Ref. [11]). We report here about some details including recent numerical results [42,43]. It should be mentioned from experiments with sub-picosecond pulses above 5TW power how plasma block generation can directly be recognized from the resulting ion and x-ray emission such that the sufficiently contrast ratio could concluded indirectly [44] such that the usual vague speculations about resonance absorption or parametric effects could be ignored.

The following computations are based on the fact that before the ps main pulse, a less than 50ps earlier acting laser prepulse produces a preplasma layer of the thickness L_{pre} at least several times smaller than the laser focal spot diameter d_f. The main laser pulse interacts most intensively with the plasma in the skin layer near the surface of the critical electron density $n_{ec}=m_e\omega^2/4\pi e^2$ (ω is the laser frequency) and the geometry of the interaction is almost planar ($L_{pre}<<d_f$). The high plasma density gradient in the interaction region produces non-linear ponderomotive forces acting – at the laser beam incidence perpendicular to the target surface – nearly parallel to the target normal. The force density f_{NL} can be expressed approximately as one-dimensional negative gradient of the electromagnetic energy density of the laser field given by its (dielectric modified) electric and magnetic vectors $\boldsymbol{E}$ and $\boldsymbol{H}$ [6]: $f_{NL}=-(\partial/\partial x)(\boldsymbol{E}^2+\boldsymbol{H}^2)/8\pi$. The gradients of the energy density near the critical surface result in two opposite non-linear forces which break the plasma and drive two thin ($\sim\lambda$) plasma blocks towards vacuum and towards the plasma interior, respectively (λ is the laser wavelength). The density of the plasma blocks is high (the ion density $n_i\approx n_{ec}/z$, where z is the ion charge state) but the electron temperature is fairly moderate at subrelativistic laser intensities. Thus, the Debye length, λ_D, is small ($\lambda_D<<\lambda$) inside the block and ions – being closely attached to electrons – move together with the electron cloud driven directly by the ponderomotive force. Since $n_i\sim10^{21}$-10^{22}cm^{-3} at $\lambda\sim0.3$-1μm, even at moderate ion velocities $v_i\sim10^7$-10^8cm/s, the ion current densities can be very high ($\sim10^9$-10^{10}A/cm^2 or higher).

The computation use the genuine two-flud model [8,43] and are performed for a 20-μm hydrogen, inhomogeneous plasma layer of initial density increasing in the direction of the laser beam propagation. Both the linear plasma density profile and the profile described by the function $n_e(x)=2xn_{ec}\{1+\exp[(x-x_c)/05.L_n]\}^{-1}$ were considered as initial values. For both profiles the boundary plasma densities were chosen in such a way that the critical plasma density n_{ec} was placed near the middle of the layer. The initial inhomogeneity of the plasma was characterised by the (relative) plasma density gradient scale length, L_n/λ, where $L_n=n_{ec}(\partial n_e/\partial x)^{-1}$. The initial temperatures of both electrons and ions were assumed to be of 30eV. Most of the calculations were carried out for laser pulses of a Gaussian shape and for a laser wave length λ=1.05μm. Our numerical studies were focused on the influence of the initial plasma inhomogeneity and the laser pulse parameters (intensity, duration) on the plasma characteristics and, particularly, on the current densities and velocities of ion fluxes produced by the laser-plasma interaction. The following results are for the non-linear initial plasma density profile and the results for the linear profile were qualitatively similar. Figure (2) presents spatial distributions of the ion velocity, the ion current density, the ion density and the electron temperature of plasma for the three time intervals after the beginning of the laser-plasma interaction. We see the generation of the

 ISSN 1813-2065 Printed in IRAQ

underdense plasma block moving against the laser (negative velocities and current densities) and the overdense plasma block behind the critical surface moving in forward laser direction (positive velocities and current densities). The plasma density profile is significantly disturbed near the critical surface and the electron temperature is the highest there.

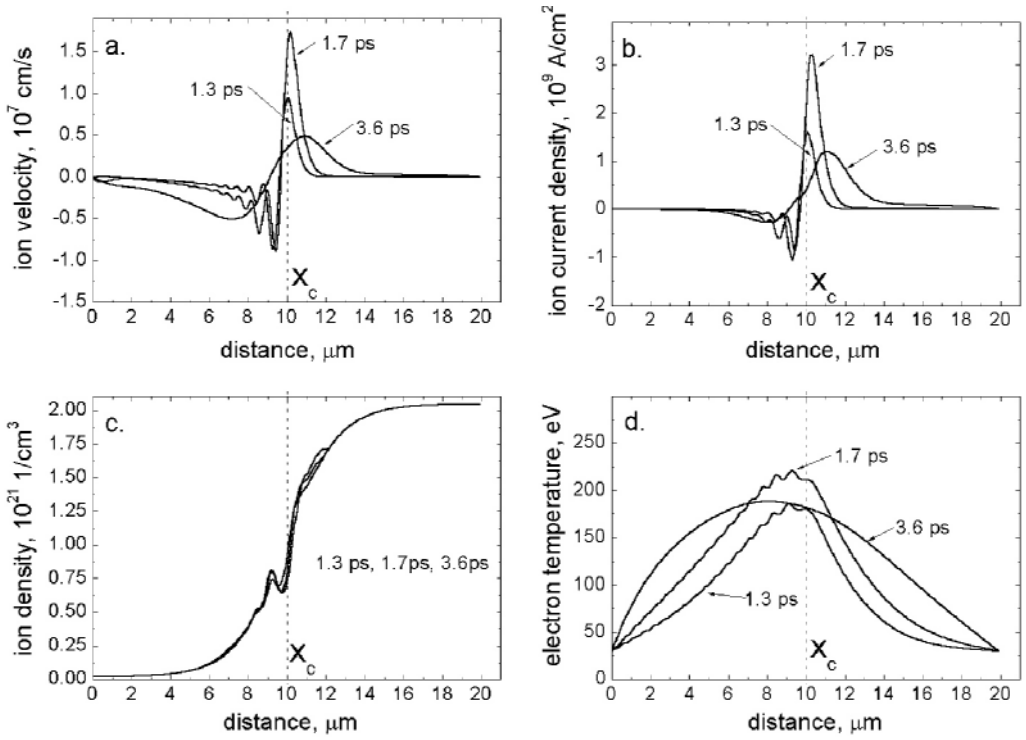

Fig. (2) Spatial distributions of the ion velocity (a), the ion current density (b), the ion density (c) and the electron temperature (d) of plasma for various times measured from the beginning of the laser-plasma interaction. τ_L=1ps, I_L=10^{16}W/cm^2, L_n/λ=2.5

The effect of the plasma density gradient scale length on the maximum ion current densities and the maximum ion velocities of backward- and forward-emitted ion fluxes can be seen in Fig. (3). For both fluxes there exist optimum values of L_n/λ but they are located in essentially different regions of L_n/λ: the highest current densities and velocities for the backward flux are attained at the small density gradients and for the forward flux – at the high density gradients.

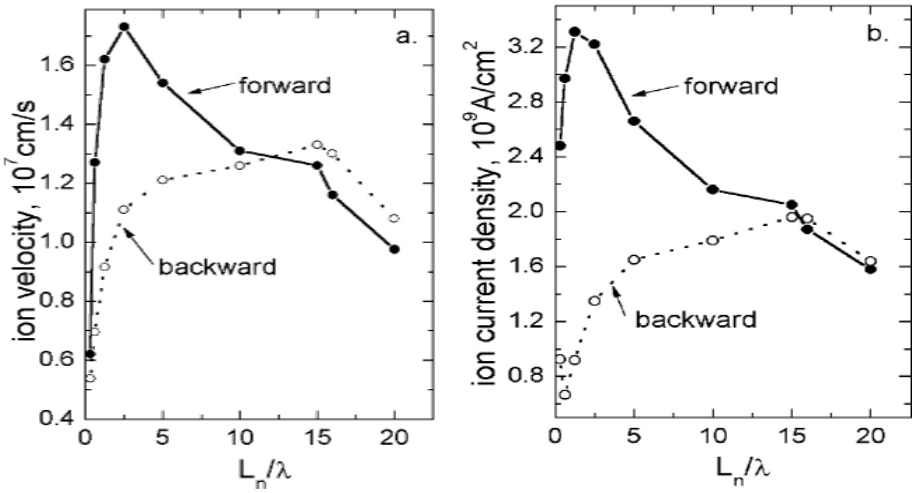

Fig. (3) The dependencies of the maximum ion velocities (a) and the maximum ion current densities (b) on the plasma density gradient scale length. τ_L=1ps, I_L=10^{16} W/cm^2

The dependencies of the maximum ion current densities and the maximum ion velocities on the 1-ps laser pulse intensity, I_L – plotted in the form of power functions – are presented in

Fig. (4). In the case of backward-emitted ions, both the current density and the velocity follow approximately the square-root dependence on I_L in agreement with a simplified theory and measurements [41,45]. However, for the forward flux these quantities increase faster with an increase in I_L and nearly linear dependence of the velocity on I_L is observed.

The influence of laser pulse duration (τ_L) on characteristics of ion fluxes is illustrated in Fig. (5). For the forward-emitted ions, the maximum ion velocity and the maximum ion current density continuously increase with an elongation of the laser pulse. Contrary to that, in the case of backward-emitted ions distinct maxima of these quantities occur at τ_L from the subpicosecond range.

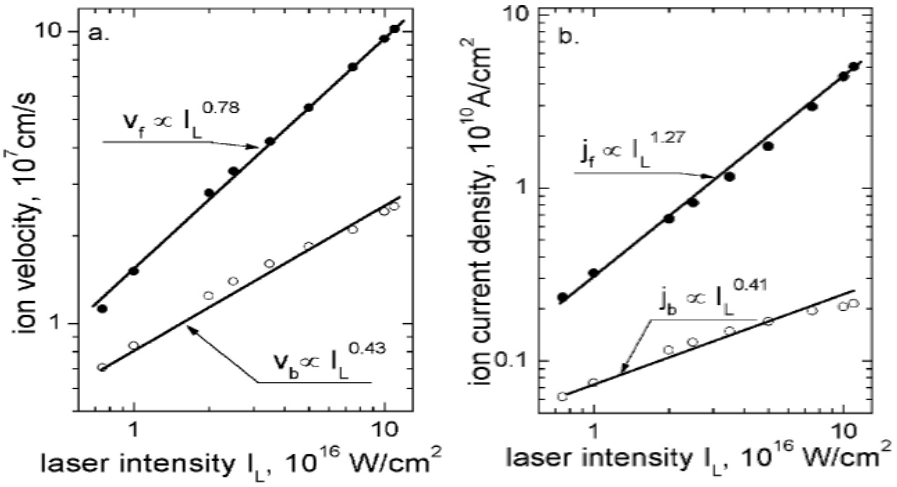

Fig. (4) The maximum ion velocities (a) and the maximum ion current densities (b) for backward-emitted (v_b,j_b) and forward-emitted (v_f,j_f) ions as a function of laser intensity, τ_L=1, $L_n\lambda$=1

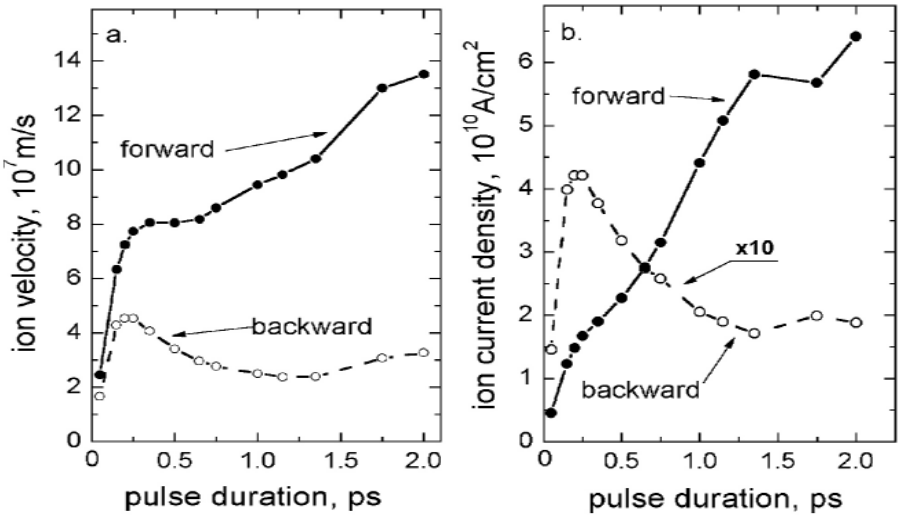

Fig. (5) The maximum ion velocities (a) and the maximum ion current densities (b) as a function of the laser pulse duration. I_L=10^17 W/cm^2, L_n/λ=1

One of the characteristic features of the dependencies presented in Figs. (3-5) are essential differences in the run of these dependencies for forward- and backward-emitted ion fluxes. These differences can be understood better when we consider the dielectric swelling factor S=1/|n| which is a measure of increase in the electromagnetic energy density of the laser field in plasma in relation to its vacuum value (n is the plasma refractive index) [6]. The necessary condition for the acceleration of plasma (ions) by the ponderomotive force in the backward direction is S>1 and, usually, the higher S, the higher backward-directed ponderomotive force. The swelling factor depends not only on the plasma density gradient but also on parameters of a laser pulse and particularly on its intensity and the pulse duration. As it results from our numerical simulations, the swelling factor (its maximal value) decreases when the plasma density gradient λ/L_n, the intensity or the pulse duration increase (within the ranges of these

 ISSN 1813-2065 Printed in IRAQ

parameters shown in the figures). For instance, at $L_n/\lambda=1$, $I_L=10^{17}$W/cm^2, the swelling factor decreases from $S\approx2$ for $\tau_L=0.2$ps down to $S\approx1.3$ for $\tau_L=2$. Thus, at high values of the above three parameters (λ/L_n, I_L, τ_L), the forward-directed force from the usual light pressure predominates the backward-directed one and, as a result, the velocities and current densities of forward-emitted ions are considerably higher than the ones for backward-emitted ions. The decreasing swelling factor is also the main reason for the faster increase in v_f and j_f (than v_b and j_b, respectively) when the laser intensity increases (Fig. 4).

In conclusion, the numerical simulations based on the two-fluid hydrodynamic plasma model confirmed both qualitatively and quantitatively the idea of production of ultrahigh-current-density ion beams with the use of ponderomotive forces induced at the skin-layer interaction of a short laser pulse of subrelativistic intensity with a thin inhomogeneous plasma layer. The results of the computations were found to be consistent with the simplified theory and measurements.

4. Aims for Laser Driven Fusion Energy

The most expensive attempts to harness fusion energy of a clean, very low cost, safe and nearly infinite energy source on earth began 70 years ago with the discovery of the nuclear reactions of isotopes of hydrogen discovered by Mark Oliphant, Paul Harteck and Lord Rutherford [46]. These reaction were absolutely different form the usual nuclear reactions where the colliding nuclei hat to energies of several MeV to reach distances of about fm. For the fusion reactions, only keV energies were necessary and the reactions happened in distances about 100 times the nuclear size. The initial hope of Oliphant [46], to produce fusion energy from particle beams on targets was fully destroyed by Spitzer in 1950 by indicating that the beam of deuterium (and tritium) irradiating a cold target low their energy to heat electrons and less the 1/300 goes into the desired fusion reactions. Therefore, one had to confine the plasma by magnetic fields to equilibrium temperatures of several dozens of million degrees such that electron collision do not count and only fusion reaction will of DT will lead to the desired energy gain.

Laser fusion with inertial confinement (ICF) reached similar high gains [46] and the goal was experimentally confirmed by compression and ignition of DT pellets using 50MJ x-radiation pulses in the Centurion-Halite experiments (see Broad [8]). With more sophisticated laser beams the irradiation by 10MJ laser pulses of ns dureation was elaborated [47]. One disappointing result was that the compression of deuterated polyethylene by laser to 2000 times the solid state density [31] arrived at rather low temperatures of 3 Million Kelvin only. To overcome this problem, the fast ignitor (FI) was invented [40] where a ns laser pulse compresses the DT fuel to few thousand times the solid state and an additional heating follows with the new type of PW-ps laser pulses according to Mourou [1].

It should be mentioned that the many MJ laser systems as NIF and the MJL [48] with ns laser pulses may not only be used for studying other nuclear fusion reactions, that the solution of a power station by compression to several 1000 solid state and temperatures of several hundred eV are sufficient in a one step process to produce very high gain fusion energy using the scheme of volume ignition [46]. This is a scheme of a fusion reactor based on present days physics where there is no physics limitation that the necessary technological development can lead to a competitive solution of a power station.

5. PW-ps Laser Pulses for Controlled Ignition of Solid DT

The here presented results of the TW or PW laser pulses of ps duration may open an alternative option for laser fusion where the complicated compression of the DT fuel to several 1000 times the solid state may be avoided and the irradiation on uncompressed solid state DT may lead to the solution of the fusion power station as a possible option for a much lower cost competitive technological solution.

The result (8) of ion current densities above 10^{10}A/cm^2 for ion energies above 50keV up to higher values from fast blocks driven into a target by the nonlinear (ponderomotive) force at laser interaction may permit an application to beam fusion as discussed before [49,50]. Light ion beams for igniting nuclear fusion reactions in uncompressed solid deuterium-tritium targets were considered since years and the necessary conditions turned out to be far above the available technology for generating the ion beams. Nevertheless this scheme was studied in various experiments [51]. The difficulties with the necessary conditions were the following two limits. The ion beam current density j had to be above the threshold $j>j^*=10^{10}$A/cm^2 [52] and the energy density the for generating a reaction front (flame propagation) into uncompressed solid DT was derived theoretically [53] to be above the threshold $E^*=4\text{x}10^8$J/cm^2. Even more pessimistic higher thresholds E^* were considered which however may be upper bonds only as long the very extensive details for the derivation of the threshold (18) are not found to be incorrect.

It may be even that the value (10) is too pessimistic as there were indications from the theory how the interpenetration of the igniting energetic ions into the cold uncompressed DT fuel may reduce the threshold E^* to $E^*_1=2\text{x}10^7\text{J/cm}^2$ [54].

How unexplored these beam fusion conditions are, may be seen from the experiments [55,56] where 2MeV electrons of an estimated current density of $3\text{x}10^6\text{A/cm}^2$ interacting with a CD_2 target showed a penetration of 0.3cm only. The single electron penetration would have been more than 40 times longer. The disagreement with the Bethe-Bloch-Bohr binary collision theory for the stopping length could be clarified by applying the collective interaction process which fully reproduces the measured 0.3cm [55]. The collective interaction was initially studied by Gabor 1953 [57] and based on the independently derived theory [58] for the successful explanation [56] of the experiments [55]. Such reduction of the collective stopping length combines with the not yet applied anomalous plasma resistivity and electric double layer effects with reduced thermal conductivity [59] points into the further decrease of the threshold (11).

Thanks to the recent results on interaction of clean TW-ps laser pulses it was possible to show experimentally [11], Eq. (8), that the rather extremely high threshold j^*, Eq. (9), for ion beam fusion has been fulfilled [45,50]. The skin layer interaction mechanism accelerates a plasma layer or block initially of 30 wavelength width and several vacuum wave lengths thickness with a critical density of $10^{21}\text{electrons/cm}^3$ highly directed against the laser light whose velocity from 20keV/nucleon at $8\text{x}10^{16}\text{W/cm}^2$ intensity could be understood in the case of DT plasma to be $1.23\text{x}10^8\text{cm/s}$. This results in a block motion with an ion current density at the target of $1.9\text{x}10^{10}\text{A/cm}^2$.

From this result it was concluded that the compressing block may be used as requested for light ion beam fusion for a power station. A 10kJ laser pulse could then produce more than 10MJ fusion energy where the exclusive use for the controlled reaction was confirmed by a declassification procedure by the authorities involved [50,60].

For the physics – within many more problems to be clarified – it has to be shown that at least the condition has to be fulfilled where we are aware that this even may be considered as a pessimistic conclusion in view of the not yet exhausted theory about the threshold E^* towards lower values. For the compressing block, the whole maximum quiver energy of the electron is converted into translation energy of the ions. The aim for the DT interaction, we use the oscillation energy of 80keV of the resonance maximum of the DT reaction may not necessarily be the best choice. Since this is close to the [9] relativistic threshold intensity I_{rel} we have to use the general case

$$\varepsilon_{osc}=m_oc^2[(1+3SI_{vac}/I_{rel})^{1/2}-1] \qquad (8)$$

where the maximum intensity $I_{max}=SI_{vac}$ due to the dielectric swelling near the critical density is expressed by the factor S with the laser intensity I_{vac} in vacuum at the target surface.

For the general analysis we have to be flexible about the chosen values of the applied maximum (dielectrically swelled) oscillation energy ε_{osc} into the translation DT ion energy ε_{trans} in adjustment to fusion cross sections. We further let open the value of the energy flux density $E^*=I_{vac}\tau_L$ for the reaction conditions or possibly even a lower value depending on the future research to find the correct value E^* where the laser pulse duration t_L will have to be in the range of ps. According to our numerical studies [43] in agreement with summarizing estimations, this value could well be a few ps

$$I_{vac}=E^*/\tau_L \qquad (9)$$

We arrive at the function for the laser wavelength

$$\lambda(\varepsilon_{trans},E^*,\tau_L,S)= \sqrt{\left(\frac{\tau_L I^*_{rel}}{3SE^*}\right)\left[\left(\frac{\varepsilon_{trans}}{m_0c^2}+1\right)^2-1\right]} \qquad (10)$$

Using as a special case $\tau_L=3\text{ps}$, $E^*=2\text{x}10^7\text{J/cm}^2$, $\varepsilon_{trans}=80\text{keV}$, we arrive at $\lambda=0.516/S^{1/2}\ \mu\text{m}$

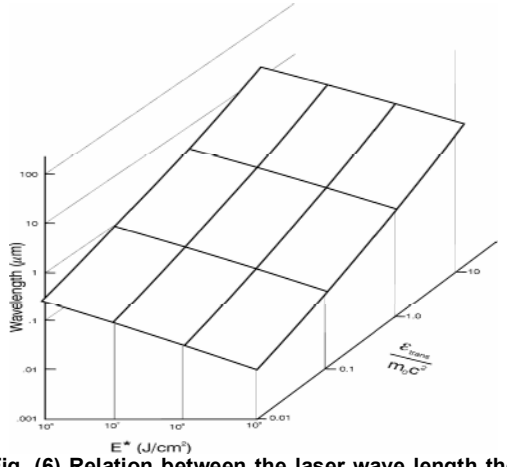

Fig. (6) Relation between the laser wave length the aimed ion energy ε_{trans} in multiples of m_oc^2 and the necessary energy flux density for ignition of uncompressed DT for S=1 and a laser pulse length of 3ps

The nonlinear force driven two-block skin layer interaction model works for swelling S considerably large than 1, as it was the case

automatically from the detailed analysis of the measurements [6,11] with S=3. The lowest possible case with S=1, is that without any dielectric swelling where the whole laser pulse energy is transferred as in the simple case of radiation pressure [9] to the absorbing plasma. We conclude that the conditions could well be fulfilled for the ignition of uncompressed solid DT fuel when applying shorter laser wave length than that of the neodymium glass laser which are well in the reach of present technology. For the pessimistic case of Bobin and Chu [53], the numerical factor is 0.105 such that with S=1 just the borderline of higher harmonics CPA or of excimer lasers would be covered. Further research on lower values of E^* and numerical studies for a little bit longer laser pulses may further relax the conditions, and longer laser wave lengths would be possible. No discrepancy was found in the detailed analysis [53] when followed up recently [61]. Figure (6) shows the dependence of the necessary laser wave length for a pulse length of 3ps and swelling S=1 which one needs for a desired ion translative energy in multiples of m_oc^2 (m_o is the rest mass of the electron) if the threshold E^* is given. Maybe there is a narrow gap for successful conditions as A. Sakharov realized [62].

References

[1] G. Mourou and T. Tajima, *Inertial Fusion Science and Applications 2001*, K.A. Tanaka, D.D. Meyerhofer and J. Meyer-ter-Vehn eds., (Elsevier, Paris 2002) p. 831; M.V. Perry and Mourou G., (1994) Science 264, 917

[2] F.P. Schäfer, *Appl. Phys.*, B39 (1986) 1.

[3] R. Sauerbrey, *Phys. of Plasmas*, 3 (1996) 4712.

[4] P. Zhang *et al.*, *Phys. Rev.*, E57 (1998) R3746.

[5] J. Badzziak *et al.*, *Laser and Particle Beams*, 17 (1999) 323.

[6] H. Hora *et al.*, *Opt. Commun.,* 207 (2002) 333.

[7] O. Thomas, *Physik Journal*, 3(7) (2004) 14.

[8] H. Hora, **"Plasmas at High Temperature and Density",** Springer (Heidelberg, 1991), paperback: S. Roderer, Regensburg (2000).

[9] H. Hora, **"Laser Plasma Physics - Forces and the Nonlinearity Principle"**, SPIE Books (Bellingham WA, 2000).

[10] J.F. Ready, **"Effects of High Power Laser Radiation"**, Academic Press (New York 1971).

[11] J. Badziak *et al.*, *Phys. Lett.*, A315 (2003) 452.

[12] R.E. Honig, *Appl. Phys. Lett.*, 3 (1963) 8.

[13] W.I. Linlor, *Appl. Phys. Lett.*, 3 (1963) 210.

[14] H. Hora, **"Physics of Laser Driven Plasmas"**, Wiley (New York, 1981).

[15] A.W. Ehler, *J. Appl. Phys.*, 46 (1975) 2464.

[16] B. Luther-Davies, and J.L. Hughes, *Opt. Commun.*, 18 (1976) 351.

[17] E. Woryna *et al.*, *Rev. Sci. Instrum.*, 71 (2000) 949.

[18] S.J. Gitomer *et al.*, *Phys. Fluids*, 29 (1986) 2679.

[19] H. Haseroth and H. Hora, *Laser and Particle Beams*, 14 (1996) 393.

[20] H. Hora, *Nuovo Cimento*, B64 (1981) 1.

[21] H. Hora, *Zeitschr. Physik*, 225 (1969) 156.

[22] H. Hora, *Phys. Fluids*, 28 (1985) 3706.

[23] M.C. Richardson and A.J. Alcock, *Appl. Phys. Lett.*, 18 (1971) 357.

[24] H. Hora, *J. Opt. Soc. Amer.*, 65 (1975) 882.

[25] T. Häuser, W. Scheid and H. Hora, *Phys. Rev.*, A45 (1992) 1278.

[26] J. Wolowski *et al.*, *Plasma Phys. Control. Fusion*, 45 (2003) 1097.

[27] J. Badziak *et al.*, *J. Phys. D: Appl. Phys.*, 34 (2001) 1855.

[28] E.L. Clark *et al.*, *Phys. Rev. Lett.*, 85 (2001) 1654.

[29] Y. Kato, *et al.*, *Phys. Rev. Lett.,* 53 (1984) 1057.

[30] A. Giuletti et al, *Laser Interaction with Matter*, J.M. Martinez-Val et.al eds., World Scientific (Singapore, 1989) p.208; S.P. Obenschain *et al.*, *Phys. Rev. Lett.*, 62 (1989) 768.

[31] H. Azechi *et al.*, *Laser and Particle Beams*, 9 (1991) 167.

[32] R.A.M. Maddever *et al.*, *Phys. Rev.*, A41 (1990) 2154.

[33] H. Hora and M. Aydin, *Phys. Rev.*, A45 (1992) 6123.

[34] R. Umstadter, *Laser Focus*, 32(2) (1996) 101.

[35] H. Hora *et al.*, *Laser and Particle Beams*, 18 (2000) 135.

[36] M. Haegelich *et al.*, *Phys. Rev. Lett.*, 89 (2002) 085002.

[37] M.H. Key, *Nature*, 412 (2001) 775.

[38] I. Spencer *et al.*, *Nucl. Instr. Meth.*, 183 (2001) 449.

[39] I. Magill *et al.*, *Appl. Phys.*, B77 (2003) 387.

[40] R. Kodama *et al.*, *Nature* 418 (2002) 933; M. Tabak *et al.*, *Phys. of Plasmas*, 1 (1994) 1626.

[41] J. Badziak *et al.*, *Appl. Phys. Lett.,* 85 (2004) 3041-3043.

[42] G. Glowacz *et al.*, *Czechoslovak J. Phys.*, 54 (2004) Supplement SPPTO.

[43] Y. Cang *et al.*, *J. of Plasma Phys.*, 70(6) (2004) 25-36.

[44] Yu-Qiu Gu, Presentation at Meeting 21 April 2004 in Mianyang/China.

[45] J. Badziak *et al.*, *Inertial Fusion Science and Applications* 2003, edited by B.A. Hammel *et al.*, American Nuclear Society (LaGrange Park Ill, 2004), p. 441.
[46] H. Hora, "Laser and Particle Beams", R.A. Mayers ed. Encyclopedia of Physical Sciences and Technology, Academic Press (San Diego), Vol.7 (1987) 99-128.
[47] H. Hora *et al.*, *J. Plasma Phys.*, 69 (2003) 413-430.
[48] M.Q. Tran, Colloquium, Sydney University 8 Sept. 2004.
[49] G. Yonas, *Scientific American*, 239(5) (1978) 50.
[50] H. Hora *et al.*, *Plasma Sci. and Technol.*, 6(1) (2004) 2172.
[51] D.D. Ryutov, M.S. Derzon and M.K. Matzen, *Rev. Mod. Phys.*, 22(1) (2000) 199-222.
[52] K.A. Brueckner and S. Jorna, *Rev. Mod. Phys.*, 46 (1974) 325.
[53] J.L. Bobin, *Phys. Fluids*, 14 (1971) 2341; M.S. Chu, *Phys. Fluids*, 15 (1972) 413.
[54] H. Hora *Atomkernenergie,* 42 (1983) 7.
[55] J.R. Kerns, C.W. Rogers and J.G. Clark, *Bull. Am. Phys. Soc.*, 17 (1972) 692.
[56] E.R. Bagge and H. Hora, *Atomkernenergie*, 24 (1974) 143.
[57] D. Gabor, *Proc. Royal Soc. London*, A213 (1953) 73.
[58] P.S. Ray and H. Hora, *Nucl. Fusion*, 16 (1976) 535.
[59] S. Eliezer and H. Hora, *Phys. Repts.*, 172 (1989) 339.
[60] H. Hora *et al.*, *ECLIM Moscow 2002 conference*, *SPIE Proc.*, O.N. Krokhin *et al.* eds., SPIE Vol.5228 (2003) 295.
[61] R. Kishony and D. Shvarts, *Phys. of Plasmas*, 8 (2001) 4925.
[62] V.E. Fortov, *from private discussions with Andrei Sakharov*.

 ISSN 1813-2065 Printed in IRAQ

SPIE *Scientific Calendar*

6 - 8 April 2010
❖ **SPIE Defense, Security, and Sensing**
Orlando, Florida, USA

13 - 15 April 2010
❖ **SPIE Photonics Europe**
Brussels, Belgium

13 - 15 April 2010
❖ **Photomask and NGL Mask Technology XVII**
Yokohama, Japan

19 - 21 April 2010
❖ **7th International Conference on Optics-Photonics Design and Fabrication**
Pacifico Yokohama, Japan

26 - 29 April 2010
❖ **5th International Symposium on Advanced Optical Manufacturing and Testing Technologies**
Dalian, China

17 - 19 May 2010
❖ **SPIE Scanning Microscopy**
Monterey, CA, USA

23 - 26 May 2010
❖ **Optical Data Storage**
Boulder, Colorado, USA

24 - 30 May 2010
❖ **26th** Symposium **on Photonics and Web Engineering, Electronics for Astronomy and High Energy Physics Experiments**
Warsaw, Poland

1 - 3 June 2010
❖ **Photonics North 2010**
Niagara Falls, Ontario, Canada

6 - 11 June 2010
❖ **Optical Interference Coatings Topical Meeting and Tabletop Exhibit**
Tucson, Arizona, USA

7 - 9 June 2010
❖ **Mirror Technology SBIR/STTR Workshop**
Boulder, Colorado, USA

9 - 10 June 2010
❖ **7th Annual Solid-State Lighting Conference, Exhibition and Gala Dinner**
West Midlands, United Kingdom

9 - 11 June 2010
❖ **International Conference on Laser Applications in Life Sciences**
Oulu, Finland

14 - 18 June 2010
❖ **International Optical Design Conference**
Jackson Hole, Wyoming, USA

14 - 15 June 2010
❖ **32nd Annual Review of Atmospheric Transmission Models Meeting**
Lexington, MA, USA

29 June - 1 July 2010
❖ **SPIE Astronomical Telescopes and Instrumentation**
San Diego, California, USA

28 June - 2 July 2010
❖ **14th International Conference on Laser Optics 2010**
St. Petersburg, Russian Federation

3 - 5 August 2010
❖ **SPIE Optics + Photonics Sub-conferences**
SPIE NanoScience + Engineering
SPIE Optical Engineering + Applications
SPIE Photonic Devices + Applications
SPIE Solar Energy + Technology
San Diego, California, USA

8 - 10 August 2010
❖ **International Symposium on Instrumentation Science and Technology**
Hangzhou, China

23 - 27 August 2010
❖ **International Conference on Coherent and Nonlinear Optics and International Conference on Lasers, Applications and Technologies**
Kazan, Russian Federation

26 - 29 August 2010
❖ **Advanced Topics in Optoelectronic, Microelectronics and Nanotechnologies**
Constanta, Romania

30 August - 3 September 2010
❖ **XVIII International Symposium on Gas Flow and Chemical Lasers and High Power Lasers**
Sofia, Bulgaria

ISSN 1813-2065 Printed in IRAQ

Walid K. Hamoudi [1]
Adel K. Hamoudi [2]
Saad A. Salih [3]

[1] *School of Applied Sciences, University of Technology, Baghdad, Iraq*
[2] *Department of Physics, College of Science, University of Baghdad, Baghdad, Iraq*
[3] *Department of Physics, Faculty of Science, Alnahrain University, Baghdad, Iraq*

Modeling of 3-D Keyhole CO_2 Laser Welding of Steel

A mathematical 3-D model for keyhole CO_2 laser welding of thick C/Mn steel sheets under variety of laser material processing conditions is presented. The analysis yields profile of the melt pool and compare it with experiments. The model combines a moving point source for the top part of the weld and a moving line source for the parallel sided region of the weld (stem). This concept produces weld profiles that have good qualitative agreement with the experiments. Mathematical model and computer program were constructed to solve two basic heat conduction equations for the moving point and line sources. The excellent match of theoretical and experimental weld profiles will make this work a good candidate for laser welding prediction in robotic networks.

***Keywords*:** Laser welding, Keyhole welding, C/Mn steel, Modeling
Received: 18 October 2009, **Revised**: 13 March 2010, **Accepted**: 20 March 2010

1. Introduction

Laser beam welding provides a unique means of joining materials at high speeds with minimum thermal distortion and metallurgical damage to the work piece [1,2]. Laser welding is a contactless tool that can be automated and controlled easily. In deep-penetration welding the material is melted with high laser intensity to form a long and thin, almost cylindrical, cavity called a keyhole surrounded by a molten region most of which flows round the keyhole and re-solidifies in the rear to form the weld. The keyhole is kept open by the excess vapor pressure as a whole over the sum of the hydrostatic pressure in the liquid metal and the surface tension force tending to close the keyhole [3]. Analytical and numerical solutions can be used to model keyhole shape, laser absorption within the keyhole, heat flow and temperature profiles of laser welds, metallurgical phases within the weld, and weld properties [4]. It is too difficult to set up a single mathematical model that comprehends all the parameters involved in laser welding. However, relationships between weld speed, keyhole size, laser power absorbed by the material and the weld width can add extra analysis to any experimental results.

The choice of laser welding parameters depends, mainly, on the material's thermal characteristics [5]. The main part of the weld is nearly parallel sided with gradual narrowing from top to bottom. At the top of the weld is a wider region of roughly semicircular shape [6]. The laser energy is absorbed by the keyhole as well as by the plasma plume above the mouth of the keyhole. The plume is formed as a result of the shielding gas and the ablated metal from the keyhole [7,8]. In spite of the complexity of the problem it is possible to construct a reasonably simple model which retains the essentials of the problem and produces results that are in good qualitative agreement with the observations.

2. Literature Review

Rosenthal's solutions represent the starting point of analytical solutions applied to welding techniques [9,10]. It was not until 1973 when Swift-Hook and Gick developed the first heat transfer model for continuous laser welding [11]. In a similar manner to Rosenthal, the laser beam was modeled as a moving line source. It was assumed that the melting temperature isotherm may determine the location and shape of the fusion zone. The width and depth of the laser fusion zone were then related to the laser power and velocity of the work piece. In their work, the formation of a keyhole was neglected and, as a result, their model produced only a partial agreement with the experimental results. In 1976, Klemens produced a model that assumes a plasma - filled keyhole, which is held open by a balance between vapor pressure within the keyhole and the surface tension in the molten region surrounding it [12].

In 1976, a three–dimensional convective flow in the weld pool was extensively investigated by Andrews and Atthey [13]. In their model they assumed a vapor pressure inside the keyhole equal to the atmospheric pressure and 100% absorption of the incident laser beam at the surface of the work piece. In practice, the former assumption is valid only for shallow keyholes, whereas the latter simplification is unjustified. In 1977, Cline and Anthony [14] presented a model in which they integrated the point source over the work piece surface to yield a Gaussian power distribution. The model assumed 100 % absorption and calculated an exponential decrease of temperature in the vertical direction. Conduction limited and keyhole welding

conditions were both considered, whereas weld pool convection was not included in the model. In 1986, convective flow was examined by Davis, et al. [15]. Their model assumed two-dimensional convective flow, independent of the keyhole depth, to solve the Navier-Stokes equations of motion. A model for two-dimensional numerical analysis of a pulsed laser welding process was presented by Russo, et al [16]. It assumes a lineally varying surface temperature and an exponential variation of kinematic viscosity with temperature respectively. Vishnu, et al, developed a three-dimensional solution for the temperature distribution due to an instantaneous stationary Gaussian heat source [17]. This solution was then extended to consider a single moving heat source and a series of heat pulses. The theoretical calculations were then compared with empirical results for gas tungsten arc (GTA) welds, but used to describe pulsed laser welding.

Gellert and Egli [18] developed a basic one-dimensional model that describes the melting of copper by a pulsed heat source. Jette and Benson [19] constructed a one-dimensional model of pulsed laser heating of optical surface, while Arutyunyan, et al. [20], developed a general hydrodynamic model of the interaction of pulsed radiation with matter. Kaplan [21] calculated the keyhole profile using a point by point determination of the energy balance along the keyhole wall by solving the energy balance equation. Frewin and Scott [22] used a finite element model of the heat flow during pulsed laser beam welding to calculate the transient temperature profiles and the dimensions of the fusion zone and the HAZ.

Sudnic et al [23] presented a numerical simulation of stationary laser welding taking into account the laser induced channel formation, the multiple laser reflections in the channel and the plasma generation. They later introduced a linear correlation between the depth and the length of the weld pool with varied laser powers and constant welding speed [24]. X He et al used a transient numerical model to study the heat transfer and fluid flow during laser spot welding of 304-stainless steel [25]. After 2002, many models have concentrated on the computational field of robotics in laser welding [5, 25, 26, 27, 28, 29, 30, 31, 32, 33] and laser welding optimization [34, 35].

The present work presents a computational modeling of laser welding phenomena within an analytical framework. The aim is to predict a three dimensional representation of heat flow in laser welding based on combing moving point and line sources to achieve an approximated model of the keyhole that agrees well with the experiments. Despite the decreasing value of the line source with depth, our model assumed a fixed value to avoid complex mathematics, however this point will be considered in the future work.

3. Mathematical Model

In order to obtain more realism and accuracy in the shape of the laser weld we modify the old model of references [9, 11] by the inclusion of a point source term near to the surface of the work-piece in addition to the line source. The present computation involves solving 3-dimensional differential heat conduction equations for carbon steel by adjusting point and line heat source strengths (λ and μ) under certain conditions and parameters for the sample until the calculated weld pool profiles match those of experimental profiles as closely as possible. In order to simplify the model and create practical relationships, we assumed that we have a perpendicular laser beam to the work piece and the 3-D system is at a steady state condition after the keyhole initiation. We also ignored the material loss due to vaporization and put the weld zone (WZ) equals to the sum of fusion zone (FZ) and the HAZ. The values of thermal conductivity and thermal diffusivity were assumed constant and equal in both solid and liquid states. Ignoring the inclusion of the distorting effects of the phase change and the effects of latent heat do not significantly alter the solutions [7, 34]. The weld pool was assumed to be bounded by an isothermal surface "isotherms" at the melting point of the metal [36, 37, 38, 39]. A three dimensional model has been constructed to represent a laser beam directed along the positive z'-axis of the work-piece where a keyhole is created. The work-piece initially at room temperature moves at a uniform speed U in the direction of the positive x´-axis along the length of the work-piece. The y'-axis is perpendicular to both other axes of coordinates. The system configuration is diagrammatically shown in Fig. (1).

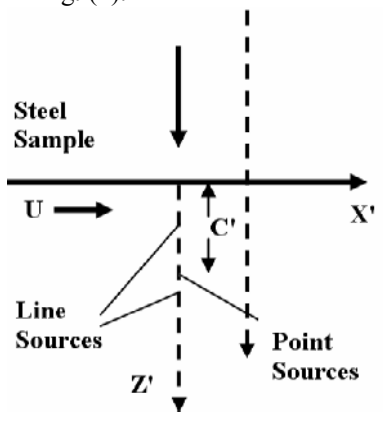

Fig. (1) Laser point and line sources. y' coordinate is perpendicular to x' and z'

The absorption processes of laser welding that occur at and in the keyhole can be described by means of a combination of point and a line sources. Then, for a line source on the axis x′ = y′=o, z′ ≥ o and a point source on the axis located at a distance c` at or beneath the surface of the work-piece, the preliminary boundary condition to be satisfied at the surface of the work-piece is,

$$\frac{\partial T}{\partial z'}=0 \quad \text{at } z'=0 \tag{1}$$

The general heat conduction equation for the temperature T as a function of x', y', z' and time t is, [9,10,22,40]

$$\frac{\partial}{\partial x}\left(k\frac{\partial T}{\partial x}\right)+\frac{\partial}{\partial y}\left(k\frac{\partial T}{\partial y}\right)+\frac{\partial}{\partial z}\left(k\frac{\partial T}{\partial z}\right)+Q=\rho\, c\frac{\partial T}{\partial t} \tag{2}$$

or

$$k\left(\frac{\partial^2 T}{\partial x^2}+\frac{\partial^2 T}{\partial y^2}+\frac{\partial^2 T}{\partial z^2}\right)+Q=\rho\, c\,\frac{\partial T}{\partial t} \tag{3}$$

Here $\boldsymbol{Q}$ is the rate of the internal heat generation per unit volume, $\boldsymbol{k}$ is the thermal conductivity, $\boldsymbol{\rho}$ is the density, and $\boldsymbol{c}$ is the specific heat per unit mass. If $\boldsymbol{Q}$ is considered to be zero, $\boldsymbol{k}$ is already assumed constant then dividing by $\boldsymbol{\rho.c}$ equation (2) is reduced to the Fourier equation,

$$\left(\frac{\partial^2 T}{\partial x^2}+\frac{\partial^2 T}{\partial y^2}+\frac{\partial^2 T}{\partial z^2}\right)=\frac{1}{K}\frac{\partial T}{\partial t} \tag{4}$$

where $\boldsymbol{K=k/\rho.c}$ is the thermal diffusivity of the work-piece. Thus when a steady-state has been reached, the equation satisfied by the temperature distribution is, [3,22,37,41]

$$K\nabla'^2 T=\frac{\partial T}{\partial t}$$

where

$$\nabla'^2=\frac{\partial}{\partial x'^2}+\frac{\partial}{\partial y'^2}+\frac{\partial}{\partial z'^2} \tag{5}$$

Inserting the system velocity $U=\dfrac{\partial x'}{\partial t}$, then substituting in (5) we get,

$$K\nabla'^2 T=U\frac{\partial T}{\partial x'} \tag{6}$$

In laser welding, the two fundamental solutions of interest for equation (6) in 3-D heat flow are chosen from [42], where

i. the first is corresponding to a point source of heat strength q_p at position $(0,0,c')$ in a medium whose ambient temperature T_0 (far from the heat source) and is given as

$$T-T_0=\frac{q_p\exp\left\{\frac{1}{2}Ux'/K-\frac{1}{2}U\left[x'^2+y'^2+(z'-c')^2\right]^{\frac{1}{2}}/K\right\}}{4\pi k\left[x'^2+y'^2+(z'-c')^2\right]^{\frac{1}{2}}} \tag{7}$$

ii. the second is corresponding to a line source of heat strength q_l per unit length on the z'-axis and is given as

$$T-T_0=\frac{q_l K_0\left[\frac{1}{2}U\left(x'^2+y'^2\right)^{\frac{1}{2}}/K\right]\exp\left(\frac{1}{2}U\,x'/K\right)}{2\pi\, k} \tag{8}$$

where K_0 is modified Bessel function of the second kind and zero order. The straightforward superposition of equations (7) and (8) will not satisfy the condition in equation (1), instead, we use a method of "images" to solve the problem. If the work-piece is extended to fill region $z'<0$ and continue the line source to place a hypothetical point source of equal strength at the image position $(0,0,-c')$ of the original, then the resulting temperature distribution will satisfy Eq. (1) and all the conditions imposed on $z'>0$. It is suitable to write the solution in dimensionless terms therefore we scale all lengths with $2K/U$ and then drop the primes by using $x'=2Kx/U$. Besides, we scale the temperature by using $\tau_p=\dfrac{T-T_0}{T_m-T_0}$. Adopting the method of images and dividing both sides of Eq. (7) by $(T-T_0)$ we obtain

$$\tau_p=\lambda\left[P(x,y,z,c)+P(x,y,z-c)\right] \tag{9}$$

Where $P(x,y,z,c)$ and $P(x,y,z,-c)$ are the dimensionless form of Eq. (7) for the point source and are given, respectively, by

$$P(x,y,z,c)\equiv P_+=\frac{\exp\left[x-\left(x^2+y^2+(z-c)^2\right)\right]^{\frac{1}{2}}}{\left[x^2+y^2+(z-c)^2\right]^{\frac{1}{2}}}$$

$$P(x,y,z,-c)\equiv P_-=\frac{\exp\left[x-\left(x^2+y^2+(z+c)^2\right)\right]^{\frac{1}{2}}}{\left[x^2+y^2+(z+c)^2\right]^{\frac{1}{2}}}$$

The parameter λ presented in Eq. (9) is given by

$$\lambda=\frac{q_p U}{8\pi k K(T_m-T_0)}$$

This can be written as

$$q_p=\frac{8\pi kK(T_m-T_0)\lambda}{U}$$

Similarly, dividing both sides of Eq. (8) by $(T-T_0)$, the temperature distribution for the line source is obtained as

$$\tau_l=\mu l(x,y) \tag{10}$$

where the temperature distribution for the line source τ_l, the dimensionless form of Eq. (8) $l(x,y)$ and the parameter μ are given, respectively, by

$$\tau_l=\frac{T-T_0}{T_m-T_0},$$

$$l(x,y)=K_0\left[\left(x^2+y^2\right)^{\frac{1}{2}}\right]\exp(x),$$

$$\mu=\frac{q_l}{2\pi k\left(T_m-T_0\right)}$$

ISSN 1813-2065 Printed in IRAQ

where $q_l=2\pi k(T_m-T_0)\mu$ is the power absorbed by the line source per unit length in Watts/mm

Adding equations (9) and (10), the total temperature distribution is obtained as

$$\tau = \tau_p + \tau_l \equiv \lambda(P_+ + P_-) + \mu l(x,y) \quad (11)$$

4. The Weld Profile and Boundary Conditions

In a keyhole laser welding, an almost long and thin cylinder is formed surrounded by molten metal which freezes at the rear to form the weld. The keyhole contains partially ionized vapor flowing parallel to its axis [43]. The maximum weld width of the molten region occurs when, τ=1 and

$$\frac{\partial \tau}{\partial x} = 0 \quad (12)$$

The corresponding value of (y) is half the weld width (keyhole radius) and can be used to obtain the weld profile as a function of depth (z). Therefore

$$\frac{\partial \tau}{\partial x} = \lambda\left(\frac{\partial p_+}{\partial x} + \frac{\partial p_-}{\partial x}\right) + \mu\frac{\partial \ell}{\partial x} \quad (13)$$

Let

$$r_+ = \left[x^2 + y^2 + (z-c)^2\right]^{\frac{1}{2}}$$

and

$$r_- = \left[x^2 + y^2 + (z+c)^2\right]^{\frac{1}{2}}$$

with some manipulations, Eq. (13) becomes

$$\frac{\partial \tau}{\partial x} = \lambda\left[\left(\frac{1}{r_+} - \frac{x}{r_+^2} - \frac{x}{r_+^3}\right)\exp(x-r_+) + \left(\frac{1}{r_-} - \frac{x}{r_-^2} - \frac{x}{r_-^3}\right)\exp(x-r_-)\right] + \mu\left\{K_0\left[\left(x^2+y^2\right)^{\frac{1}{2}}\right] - \left(x^2+y^2\right)^{-\frac{1}{2}} * K_1\left[\left(x^2+y^2\right)^{\frac{1}{2}}\right]\right\}\exp x \quad (14)$$

The weld profiles can then be investigated numerically with specific choices of strengths of the point and line sources (λ and μ) and specific locations of the point source (c). Equation (12) is solved numerically for sequence values of (z). Increasing λ will widen the top part of the weld while increasing μ increases the stem width. Increasing the value of (c) lowers the position of the point source and in most cases, a value of (c) close to zero is to be expected. A computer simulation program was constructed to predict the formability of laser welds in thick carbon-steel sheets, see Table (1). This simulation may be used to automate laser welding process in the current sophisticated systems for 1, 2 and 3-D modeling and monitor robotic welding machines.

5. Experiment

A CO_2 laser beam with two different powers was used to perform butt-welding of 12mm thick (BS4360) C/Mn steel. Full and partial penetrations were obtained using the laser parameters shown in Table (2). The laser source was operating in the TEM_{01} mode so that a maximum output power could be achieved. The experimental parameters and physical constants of the laser beam and relevant material adopted in this work are shown in Table (3).

Table (1) Theoretical λ, μ and c values and experimental data used

Sample	Laser Power (kW)	Scan Speed (mm/s)	Welded Depth (mm)	λ	μ	C
1	7.0	7.5	12.0	0.395	1.61	0.0
2	7.0	12.5	10.0	1.570	1.985	1.0
3	10.0	10.0	12.0	0.587	1.297	0.0
4	10.0	15.0	12.0	0.251	1.371	0.0
5	10.0	20.0	12.0	0.367	1.689	0.0

Table (2) Laser and welds parameters used in the five experiment

Sample No	Laser Power (kW)	Travel Speed (mm/s)	Laser Intensity W.cm^{-2}	Welded Depth (mm)	Max. width (mm) Expt-Cal.	Stem width (mm) Expt-Cal	Welded Area (mm^2) Expt-Cal
1	7.0	7.5	2.8×10^6	12.0	8.0-8.06	6.5-6.52	87-87.51
2	7.0	12.5	2.8×10^6	10.0	6.0-6.02	4.5-4.5	53-/52.64
3	10	10	4×10^6	12.0	6.0-6.04	4.0-4.02	60-60.37
4	10	15	4×10^6	12.0	3.5-3.5	2.8-2.84	38-38.04
5	10	20.0	4×10^6	12.0	3.0-3.05	2.5-2.53	33-33.48

Table (3) Laser data and material parameters

Laser and material parameters	Description
Laser	CO_2
Power (kW)	7.0, 10
Mode	TEM_{01}
Focal spot (mm)	0.5
Shielding gas jet	He, flow 50 l/min
Steel type	BS43660 C/Mn Steel.
Thickness (mm)	12.0
Thermal conductivity k (W/mm.°C)	0.019385
Thermal diffusivity K (mm^2/s)	12.5
Melting point (°C)	1547
Ambient Temp. (°C)	27

6. Results and Discussion

The present model and its experimental data have provided simple ways of representing what has actually happened in a given weld once information about the weld profile has been obtained. The point and line sources model in this work is considered to deal with complex physical processes in the keyhole involving the sum total of effects due to the direct absorption of laser light incidence on its walls, the effects of plasma formation there and complex effects due to multiple scattering of laser light in the vapor of the keyhole. The model has been applied to a series of completed weld pairs of mild carbon steel sheets. The prediction of the top maximum width and the width of the parallel-sided section (stem width), depending on a certain experimental depth of the laser melted zones, is the base for drawing the weld profile map that will be discussed as well as the other predictions of the main model.

Although the shapes of the weld samples vary considerably, this model produces profiles which have sufficient qualitative agreement with actual welds. Besides, this model makes it possible to estimate the powers absorbed in the upper part of the weld as well as the parallel-sided section. On the other hand, it is possible that some of the effects observed in these welds are partly or wholly caused by flow or upwelling in the liquid metal at the rear of the weld pool [44]. These mechanisms which occur in deep penetration welds may lead to differences in the overall shape of the observed keyhole from that predicted by methods such as presented here. It is unlikely however that this would make a very big difference between the actual and theoretically estimated total power absorbed.

The results from the model can either be represented in real units to simulate a particular run or shown as generalized curves. The ways in which the theory makes a good contact with the experiment are of prime interest. The prediction of the top maximum width, stem width, welded area and the thermal input that have proved to be comparable with experiments or very close to. The theoretical model described here can be extended using a 3-D graphic program to show the profiles of the whole weld pool. This would give more than just the cross-sectional shape which is the main subject of this study. Figure (2)) shows the excellent fit between profiles of the experimental welds (solid dark) and those obtained by computation (solid blue). For comparison, cross-section of real laser welds is presented in Fig. (3).

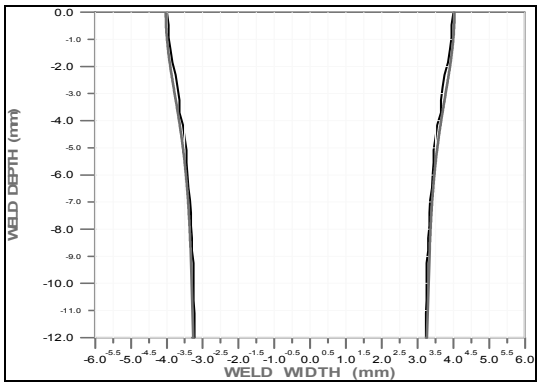

Sample (1)

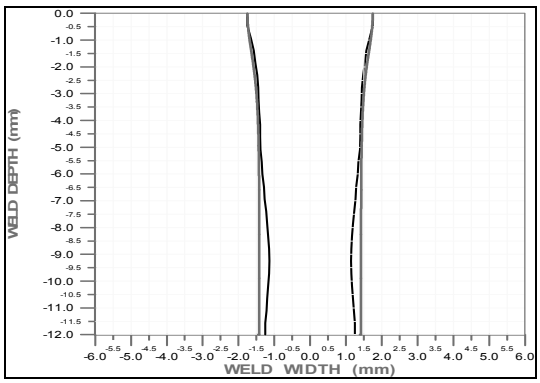

Sample (3)

Fig. (2) The experimental (solid dark) and calculated (solid light) weld profile

Sample (1) **Sample (3)**

Fig. (3) Cross-section of real laser welds

Surface tension force, also known as Marangoni force, is generated by spatial surface tension gradient. Fluid under this force alone will have a direction of flow and shape depending on

the sign value of the thermal coefficient of surface tension. The latter for pure metals is negative, and the fluid flow moves radially outward giving the pool a wide and shallow shape. When there is a significant amount of sulfur or oxygen in the alloy, the value is positive. In this case, the fluid flow and weld pool shape is different resulting in a short width and deep depth. The direction of the flow is the results of the surface tension being high in the center of the pool and low near the weld pool edge, causing the liquid to move toward the heat source and the surface tension to decrease resulting in the pulling of the liquid inward. This fluid flow causes a narrow and deep pool shape.

In the partial penetration welding, sample 2, we considered the stem width as a radius of a circle, then subtracted this radius value from the depth of the keyhole in order to find the center of this circle. Using the equation of the circle we could blind the keyhole and close its terminals to approach approximately the real closing envelope.

7. Conclusions

A general modified model of deep-penetration laser welding has been constructed by the addition of a point source to the original line source model whose strengths vary with position. In this way, the problems associated with the earlier models were overcome. This model provides a simple representation of a laser weld without being involved in the complicated nature of the energy interchange in the keyhole. The theory was applied to butt welds between pairs of thick carbon-steel sheets and it was possible to describe the way in which the power is absorbed through the work-piece giving interesting insights into the nature of the process. The present modified model has demonstrated relatively excellent laser welding results as there are a coincidence between experimental and theoretical maximum weld top width, stem width and welded area. The melt pool interface ($T=T_0$) is defined which in turn gives the seam cross-section. It can produce profiles that have sufficient qualitative agreement with actual welds.

Furthermore, this model was used to calculate the laser power absorbed in the upper part of the weld and in the parallel-sided section. However, the details of few shapes predicted do not entirely agree. The main reason is that some weld pools in depth are not parallel sided. We have started the model by choosing two fundamental solutions (point and line sources) for the Fourier equation that Rosenthal and others had obtained. The unique advantage of the present model lies in its flexibility to simulate specific weld pool shapes and its wide range of applications for different materials. It is very easy to vary the input data, i.e., laser power, travel speed, solid constants, the path of the heat source, depth as well as λ, μ and c, so that the shape of the weld pool can easily be calculated.

References

[1] S. Chakraborty and P. Dutta, *Current Science, India*, 78(7), 887-891, (2000).

[2] W. Duley, **"Laser Welding"**, Wiley-Inter Science Publication, ISBN, (1998).

[3] C. Lampa and A. Kaplan, *Lasers in Engineering*, 7, 241-252, (1998).

[4] P.L. Moore, "Investigation into the microstructure and properties of laser and Laser/Arc Hybrid welds in pipelines steels", PhD dissertation, Darwin College, University of Cambridge, UK, Aug.11, (2003).

[5] Wei Han, "Computational and experimental investigation of laser drilling and welding for microelectronic packaging", Ph.D. dissertation, Worcester Polytechnic Institute, Cambridge, May 10, (2004).

[6] Nazmi Postacioglu, *J. Phys. D: Appl. Phys.*, 20, 340-345, (1989).

[7] R. Akhter et al., *J. Phys. D: Appl. Phys.*, 21, 23-28, (1989).

[8] Walid K. Hamoudi and R. Ducharme, *Int. J. for Joining of Mater.*, 8(1), (1996).

[9] D. Rosenthal, *Welding J.*, 20, 220-s to 234s, (1941).

[10] D. Rosenthal, *Transactions of the ASME*, 849-866, (1941).

[11] D.S. Hook and A. Gick, *Welding J.*, 52, 492-s to 400-s, (1973).

[12] P.G. Klemens, *J. Appl. Phys.*, 47(5), 2165-2174, (1976).

[13] J.G. Andrews and D.R. Atthy, J. Phys. D: Appl. Phys., 9 (1976) 2181-2194.

[14] H.E. Cline and T.R. Anthony, *J. Appl. Phys.*, 48(9), 3895-3900, (1977).

[15] M. Davis, P. Kapadia and J. Dowden, *Welding J.*, 65(7), 167s to 174s, (1986).

[16] A.J. Russo, R.L. Akau and J.L. Jellison, *Welding J.*, 169(1), 23-s to 29-s, (1990).

[17] P.R. Vishnu, W.B. Li and K.E. Eastring, *J. Mater. Sci. Tech.*, 7(7), 6649-659, (1991).

[18] B. Gellert and W. Egli, *J. Phys. D: Appl. Phys.*, 21(12), 1721-1726, (1988).

[19] A.N. Jette and R.C. Benson, *J. Appl. Phys.*, 75(6), 3130-3141, (1994).

[20] R.V. Arutrunyan V.Y. Baranov and V.Y. Bolshov, *Sov. J. Quantum Electron.*, 17(2) 163-168 (1987).

[21] A. Kaplan, *J. Phys. D: Appl. Phys.*, 27, 1805-1814, (1994).

[22] M.R. Frewin and D.A. Scott, *Weld. Res. Suppl.*, 15-s to 22-s, (1999).

[23] W. Sudnic, D. Radaj and W. Erofeew, *J. Appl. Phys.*, 29, 2811-2817, (1996).
[24] W. Sudnic, D. Radaj and W. Erofeew, *J. Appl. Phys.*, 33, 662-671, (2000).
[25] X. He, P.W. Fuerschbach and T. DebRoy, *J. Phys. D: Appl. Phys.*, 36, 1388-1398, (2003).
[26] J. Weston, "Laser welding of aluminum alloys", Ph.D. Thesis, University of Cambridge, UK, (2003).
[27] J.D. Majumdar and I. Manna, *Sadhana Acad. Proc. in Eng. Sci., India*, 28 (3&4), June/Aug. (2003).
[28] Y. Lin and F.G. Shi, *J. Lightwave Technol.*, 23(2), (2005).
[29] D. Berglund, "Simulation of welding and stress relief heat treating in the development of aerospace components", Licentiate Thesis, Lulea Univ. of Technology, (2000).
[30] J. Xie, *Welding J.*, 223s to 230s, Oct. (2002).
[31] T. Jokinen, "Novel ways of using Nd:Yag laser for welding thick section stainless steel", Ph.D. thesis, Lappeenranta Univ. of Tech. Finland, May (2004).
[32] X. He, T. DebRoy and P.W. Fuerschbach, *J. Phys. D: Appl. Phys.*, 36(12), 1388-1398, (2003).
[33] Z. Yang, "Modeling weldment macro and micro-structure form fundamentals of transport phenomena and pulse transformation theory", Ph.D. thesis, The Pennsylvania State University: 13-16, May (2002).
[34] A. Ancona1 et al., *J. Phys. D: Appl. Phys.*, 39 563-574 (2006).
[35] K.Y. Benyounis, A.G. Olabi and M.S.J. Hashmi**,** *Opt. Laser Technol.*, 40(1) pp.76-87 (2008).
[36] B.R. Finks, P.D. Kapadia and J. Dowden, *J. Phys. D: Appl. Phys.*, 23, 643-653, (1990).
[37] Sindo Kou, **"Welding Metallurgy"**, John Wiley & Sons INC Publications, 2nd ed., (2002).
[38] H.J. Anderson, "Sensor based robotic laser welding/Based on feed forward and gain scheduling algorithms", Ph.D. thesis, Aalborg Univ., Denmark, Jan. (2000).
[39] J. Dowden, P. Kapadia and N. Postacioglu, *J. Phys. D: Appl. Phys.*, 22, 741-749, (1989).
[40] W.K. Hamoudi and R.A. Ismail, *Int. J. of Joining of Mater.*, 7, 124-128, (1995).
[41] M. Jakob and G.A. Hawkins, **"Elements of Heat Transfer"**, John Wiely and Sons, (1957).
[42] W.M. Steen et al., *J. Phys. D: Appl. Phys.*, 21, 1255-1260, (1988).
[43] J. Dowden, *Fluid Mech.*, 110, 149-159, (1981).
[44] J. Magee, P. Okon and J. Dowden, "The relation between spot size and penetration depth in laser welding", IIW Doc. IV-764 (2000), Doc.212-975 (2000).

 ISSN 1813-2065 Printed in IRAQ

IOP *Scientific Calendar*

Annual Plasma Physics Conference

The 37th IOP Annual Conference on Plasma Physics is an ideal opportunity for plasma physicists from all areas such as Magnetic and Inertial fusion, High energy density plasmas, Laser plasmas, Astrophysics, Low temperature, Technological and Dusty plasmas to meet and discuss ideas and recent developments.
Mon, 29 Mar – Thu, 1 Apr 2010
4 Days
The Low Wood Hotel, Ambleside Road, Windermere, LA23 1LP

Novel Aspects of Surfaces and Materials (NASM-2010)

An interdisciplinary and interactive conference delivered in a format that highlights new developments and promotes opportunities for new collaborations on funding applications and networking.
Sun, 11 Apr – Thu, 15 Apr 2010
5 Days
Chancellors Hotel and Conference Centre, The University of Manchester, Oxford Road, Manchester, M13 9PL

IOP Nuclear Physics Conference

The UK Institute of Physics Nuclear Physics Conference will take place in Edinburgh 19 - 21 April 2010. The Conference will feature plenary and parallel oral contributions as well as a poster session.
Mon, 19 Apr – Wed, 21 Apr 2010
3 Days
The University of Edinburgh, Pollock Halls, 18 Holyrood Park Road, Edinburgh, EH16 5AY

Combustion and NOx in the Environment (Formely known as Low NOx Combustion)

Nitrogen oxides are major pollutants from combustion and their emission is strictly regulated by law and technologically challenging to reduce. This meeting will focus on the fundamentals and practical aspects of low NOx technologies and will be of interest to academics and industrialists alike. A series of invited talks will provide high quality reviews of the combustion processes and the impacts of combustion products on human health and on the environment.
Wed, 21 Apr 2010
East Midlands Conference Centre, Beeston Rd, Nottingham, NG7 2QD

Quantum Dots 2010

The 6th International Conference on Quantum Dots aims to provide a forum for scientists from different research branches including physics, chemistry, materials science and engineering to discuss optical, transport and structural properties as well as applications of quantum dots.
Mon, 26 Apr – Fri, 30 Apr 2010 (5 Days)
East Midlands Conference Centre, Beeston Rd, Nottingham, NG7 2QD

Plasmonics UK Meeting

This conference aims to capture the state of the art of UK strength in plasmonics, and to brainstorm where it is heading in the next 5 years.
Mon, 10 May 2010
Institute of Physics, 76 Portland Place, London, W1B 1NT

Tribology of Touch & Feel

A meeting of invited talks focused on the complex tribological stimuli produced at the skin surface by touching or rubbing objects, and their role in tactile perception.
Wed, 12 May 2010
Institute of Physics, 76 Portland Place, London, W1B 1NT

4th International Conference on: Preservation and Conservation Issues in Digital Printing and Digital Photography

The Printing and Graphics Science Group and the University of the Arts London (Materials and the Arts Research Centre - MATAR) are staging a two-day international conference for conservators, digital photographers and printers
Thu, 27 May – Fri, 28 May 2010 (2 Days)
Institute of Physics, 76 Portland Place, London, W1B 1NT

36th Stirling Physics Meeting

- The largest meeting of the physics teaching community in the UK
- A mixture of information, simulation and communication
- An effective meeting, bringing you into contact with the latest thinking in physics and physics education, and with colleagues from throughout Scotland.

Wed, 9 Jun 2010
University of Stirling, Stirling, FK9 4LA, Scotland

Conference, Dinner and AGM 2010

This meeting is organised by the Institute of Physics in Scotland in association with the Stirling Physics Teachers' Meeting.
Wed, 9 Jun 2010
Stirling Management Centre, University of Stirling, Stirling, FK9 4LA

Plasmas Surfaces and Thin Films

This one day meeting is a popular annual event providing a forum for those involved in using plasmas and ion beams for surface modification, surface analysis and thin film deposition. Topics covered include modelling of fundamental atomic collisions in solids through to new techniques for high throughput industrial processes.
Wed, 16 Jun 2010
Institute of Physics, 76 Portland Place, London, W1B 1NT

Metrology and Characterisation of Nanoparticles

This one-day meeting will provide a forum for the presentation of recent results and for discussion of how electron microscopy and scanning probe techniques can be applied to more accurately measure the dimensions and properties of nanoparticles.
Mon, 28 Jun 2010
Institute of Physics, 76 Portland Place, London, W1B 1NT, UK

Perspectives on Photovoltaic Materials and Technologies

The one day workshop will be a forum to discuss major issues relevant to current and emerging photovoltaic materials and technologies. A combination of oral presentations by invited speakers from Europe and the UK, and poster sessions, will review recent advances in new materials, new processes, technologies and process characterisation techniques.
Wed, 30 Jun 2010
Institute of Physics, 76 Portland Place, London, W1B 1NT

IOP Superconductivity Group Summer Science Meeting

The annual scientific meeting of the IOP superconductivity group brings together researchers in fundamental and applied aspects of superconductivity. The day will include invited and contributed talks and the group prize lecture. There will also be a poster session.
Mon, 5 Jul 2010
Institute of Physics, 76 Portland Place, London, W1B 1NT

Photon10

Photon10 is the largest optics conference event in the UK and the fifth in the series; following Photon02 (Cardiff), Photon04 (Glasgow), Photon06 (Manchester) and Photon08 (Edinburgh).
Mon, 23 Aug – Thu, 26 Aug 2010 (4 Days)
University of Southampton, University Road, Southampton , SO17 1BJ

13th IMEKO TC1-TC7 Joint Symposium

The 13th IMEKO TC1-TC7 Joint Symposium will take place at the City University London, United Kingdom in September 2010. For the first time this Symposium will also include the IMEKO Technical Committee 13 (TC13) - Measurements in Biology and Medicine.
Wed, 1 Sep – Fri, 3 Sep 2010 (3 Days)
London

Physics Meets Biology

Biologically inspired Physics is an extraordinarily wide field, covering the behaviour of systems from single molecular machines to organisms and even ecosystems. Physics Meets Biology 2010 will provide a broad view of the most recent and exciting research across a broad range of topics and scales: its scope includes physical probes and imaging, bionanotechnology, molecular machinery, cytoskeletal mechanics, signalling, control, neural systems, development, evolution and ecology.
Wed, 1 Sep – Fri, 3 Sep 2010 (3 Days)
St. Catherine's College, Manor Road, Oxford, OX1 3UJ

Wind Energy - Challenges for Materials, Mechanics and Surface Science

Wind energy is now an established means of alternative energy generation. Wind energy farms are a regular feature of the landscape in many countries, and large off shore wind turbine farms are being raised in many places as well. However, the hunt for more efficient means of wind energy generation continues.
Thu, 28 Oct 2010
Institute of Physics, 76 Portland Place, London, W1B 1NT

ISSN 1813-2065 Printed in IRAQ

Low Temperature Techniques Course

This one-day meeting is held primarily for newcomers to the field of experimental research at low temperatures. A series of talks are given by experts in the fields of cryogen handling, thermometry, measurement and control, and cryogenic techniques below 1 Kelvin. There is also an introduction to commercially available low temperature equipment. The basic methods are discussed along with useful tips on how to design experiments more specific to your own research. The talks are accompanied by an extensive set of notes for future reference.
Wed, 3 Nov 2010
East Midlands Conference Centre, University Park, Nottingham, NG7 2RJ

Bad Breath: Etiology, Diagnosis and Treatment

Bad breath is a common condition, affecting some 20% of adults worldwide. Recent advances include new theories of the etiology of breath odors, novel diagnostic methods and treatment regimens.
Mon, 15 Nov 2010
Institute of Physics, 76 Portland Place, London, W1B 1NT

Electrospinning - Principles, Practise and Possibilities

Electrospinning is a platform technology for producing novel nanofibrous materials with a high surface to volume ratio, significant fibre interconnectivity and microscale interstitial spaces. Electrospun fibres are of high interest in a diverse range of applications ranging from cell biology and tissue engineering, through filtration to power and optoelectronic devices. This one day meeting will reflect the multidisciplinary nature of the science involved with and supported by electrospinning. It will be of interest to scientists from the life and physical sciences, engineering and application technologists.
Wed, 24 Nov 2010
Institute of Physics, 76 Portland Place, London, W1B 1NT, UK

Experimental Techniques in Semiconductor Research

This one-day course is aimed primarily at new researchers working in the fields of experimental semiconductor physics and semiconductor technology.
Wed, 24 Nov 2010
East Midlands Conference Centre, The University of Nottingham, University Park, Nottingham, NG7 2RJ

CMMP 10

CMMP10, with a wide range of symposia will reflect the breadth of condensed matter and materials physics - this series of conferences attracts the highest quality invited and plenary talks, and offers a forum for student presentations.
Tue, 14 Dec – Thu, 16 Dec 2010
3 Days
University of Warwick, Coventry, CV4 7AL

Parvez A. Riza Khan
Sakhi M. Butta
Suheel A. Malik

Department of Electronic Engineering, Faculty of Engineering and Technology, International Islamic University, Islamabad, Pakistan

Modeling of Transport Properties of Amorphous Silicon Solar Cells

In this report we present the status of three projects; amorphous silicon solar cell characteristics and modeling, hole drift mobility measurements in microcrystalline and amorphous silicon, and hole-conducting polymers as p-layer materials for amorphous and crystal silicon solar cells. The work described herein was actually done on c-Si substrates, and is preliminary to work on a-Si:H based n/i structures. Fairly good c-Si/polyaniline diodes were fabricated; the open-circuit voltage under illumination was about 0.4V. The solar conversion efficiency of as-deposited pin a-Si:H solar cells can be explained surprisingly well from hole mobility and optical absorption measurements on the intrinsic layer material. We first realized this fact about 18 months ago.

***Keywords*:** Solar cells, Amorphous silicon, Interface, Transport properties
Received: 01 November 2009, **Revised**: 20 February 2010, **Accepted**: 28 February 2010

1. Introduction

We believe that we can demonstrate that the low hole drift-mobility of a-Si:H largely determines the electrical properties of as-deposited a-Si:H cells at solar illumination intensity and near room-temperature. We think it is fair to say that, despite 20 years of work on the characterization of amorphous silicon and amorphous silicon solar cells, there has been no definitive, quantitative model for how the cells work – even under restricted conditions such as the as-deposited state. Our hope for future work is that we can leverage the success of this model to gain deeper insight into the light-soaked state. The main activities in the last year have been to: (i) Obtain an improved set of J-V measurements on as-deposited a-Si:H solar cells to serve as the target for cell modeling, and (ii) to explore the range of validity of the "hole drift-mobility only" model for the as-deposited properties.

The improved set of measurements involves the use of a thickness series of cells and of a near-infrared laser to obtain uniformly absorbed illumination. Measurements were recorded over a wide range of illumination intensities. The more definitive set of measurements shows good agreement with the "hole mobility only" model for intensities ranging from 1% of AM1.5 up to AM1.5. For low intensities, this model is not very successful. It seems likely that measurements in this regime are more sensitive to deep levels such as dangling bonds.

In prior work we have obtained open-circuit voltages up to 0.73V using "PEDOT:PSS," which is a commercially available hole-conducting polymer. PEDOT:PSS uses water as its solvent; we generally deposit the polymer onto a-Si:H, and we have been concerned that oxide formation has led to reduced V_{OC}. In our present work we have been exploring doped polyaniline as the hole-conducting polymer, which uses a non-aqueous solvent.

2. Experiment

We have fabricated a simple device by spin coating a layer of conductive polyaniline onto a silicon substrate. We have considered the following relation:

$$\mu_D \equiv \frac{d^2}{2(V+V_{bi})t_T} \qquad (1)$$

where d is the i-layer thickness, V the applied voltage, V_{bi} is a correction for the internal field, and t_T is the transit-time corresponding to a charge collection of 50%

Two kinds of silicon substrates were used in this experiment: (i) n-type, orientation (100), R=2Ωcm and (ii) n-type, orientation (111), R>3000Ω.cm. We evaporated a large area, 50nm thick aluminum contact to the back (unpolished) side of the wafer. Immediately before the polymer film was applied, the silicon wafers were etched in a 2.5% HF solution.

The polyaniline base was obtained from Sigma-Aldrich Company. The solvent is dichloroacetic acid (DCA); the dopant is 2-acrylamido-2-methyl-1-propanesulphonic acid (AMPSA). The polyaniline solution was made following previous procedure [1]. The area of the spin-cast doped polyaniline film was around 0.5cm^2. The films were annealed in air at 80°C for 24 hours after casting. A circular, gold contact (50nm thick) was then evaporated onto the polyaniline film. The polyaniline films were typically 5μm thick; the resistivity of the doped

films was about $10^{-1}\Omega$.cm. The current-voltage characteristics were measured at room temperature with a Keithley 2400 source meter.

3. Results and Discussion

The work described herein is actually done on c-Si substrates, and is preliminary to work on a-Si:H based n/i structures. We were able to fabricate fairly good c-Si/polyaniline diodes; the open-circuit voltage under tungsten halogen illumination was about 0.4V. The solar conversion efficiency of as-deposited pin a-Si:H solar cells can be explained surprisingly well from hole mobility and optical absorption measurements on the intrinsic layer material. We first realized this fact about 18 months ago; at the right, we have reproduced a figure illustrating the agreement between measurements (on United Solar cells) and the model [2].

The surprise in this model is its simplicity. As has been summarized not long ago in the monograph of Schropp and Zeman [3], the standard model for undoped a-Si:H incorporates four (or more) classes of electronic states: valence bandtails, conduction bandtails, and two or more dangling bond levels. Perhaps 20 or more parameters are required if all possibly relevant electronic transport and trapping processes are treated, and veteran scientists might well despair of gaining insight from the daunting exercise of matching so many parameters to such simple measurements.

The hole drift-mobility in a-Si:H can generally be explained satisfactorily using an electronic density-of-states model with an exponential valence bandtail; these bandtail parameters are the main ones in the model. In Fig. (1), we illustrate the density-of-states; note that no defect levels are incorporated. Additionally, the conduction bandtail in this model is sufficiently narrow that it is unimportant near room-temperature; only the conduction band "effective density-of-states" N_C has a noticeable effect on the solar cell parameters, and even this effect is weak.

The relative simplicity of the proposed model is certainly refreshing, and we decided to make a more stringent comparison of cell properties with this model's predictions. As experts will no doubt recognize, graphs of power vs. thickness such as we did for Fig. (2) depend heavily upon optical properties, and one doesn't know for sure that mistakes in estimating optical effects are not being cancelled by mistakes in estimating electronic properties. For this purpose we wanted to obtain a set of cell measurements using intense, near-infrared, monochromatic laser illumination that was uniformly absorbed in the cell. Under white-light illumination, a good deal of the power generated by a single-junction cell is due to strongly absorbed illumination; models for such cells are quite sensitive to the absorption spectrum of the intrinsic and p-layers, but are less sensitive to transport and recombination properties of the intrinsic layer than are measurements with uniformly absorbed illumination.

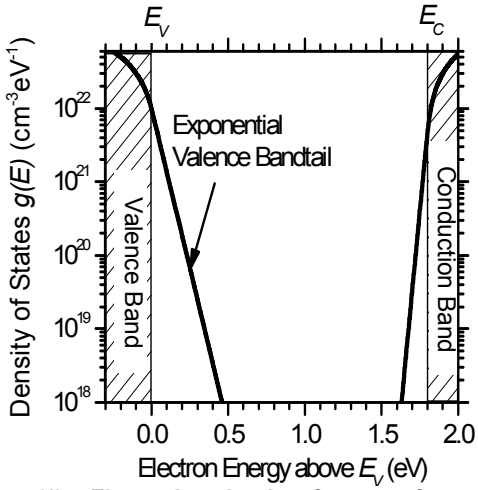

Fig. (1) Electronic density-of-states for the "bandtail" only model. The most important parameters are those of the exponential valence bandtail, since these control the (small) magnitude of the hole drift mobility

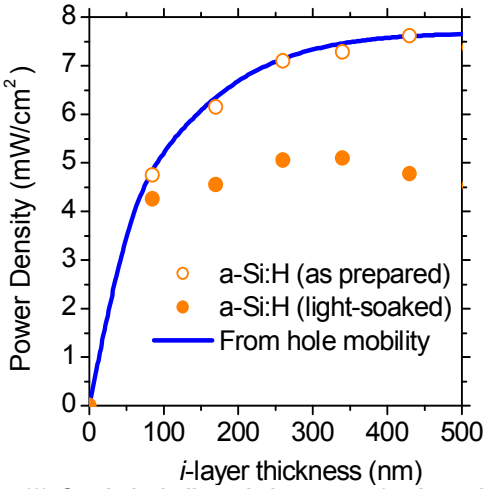

Fig. (2) Symbols indicated the power (under solar simulator illumination) for a-Si:H solar cells with varying absorber-layer thickness. The line is a model calculation encompassing hole drift-mobilities (through valence bandtail parameters), but neglecting dangling bonds and other intrinsic layer defects altogether

United Solar Ovonic LLC agreed to collaborate on these experiments, and sent us a series of samples with thickness varying from 200nm to 900nm. AM1.5 measurements were done at United Solar before the samples were sent to Syracuse. At Syracuse, we have done intensity-dependent cell measurements using illumination from a 685nm laser (absorption length about 1500nm). The model calculations used the AMPS-PC engine developed by Steve

Fonash's group at Penn State University; we used exactly the same electronic modeling parameters that we proposed previously [2]. Temperature-dependent measurements are underway as well, but will not be reported here.

In Fig. (3), we show quantum efficiency measurements as a function of i-layer thickness (i.e. the short-circuit (particle) photocurrent density J_{sc}/e normalized by the incident photon flux F). The laser wavelength λ=685nm). The solid lines are the results of "bandtail only" simulation. The simulations indicate that, for the lowest flux $F=6\times10^{13}cm^{-2}s^{-1}$, J_{sc} corresponds well to the integrated absorption of photons throughout the intrinsic-layer. The curvature noticeable for larger thicknesses is the effect of the finite absorption coefficient $\alpha=6.2\times10^{3}cm^{-1}$. As the flux is further increased (a few hundred times), there is a small additional decrease in the quantum efficiency for the thickest samples. This effect is due to recombination inside the i-layer, and is consistent with the poor fill-factors we measured (and predicted) for these thicker samples at large flux.

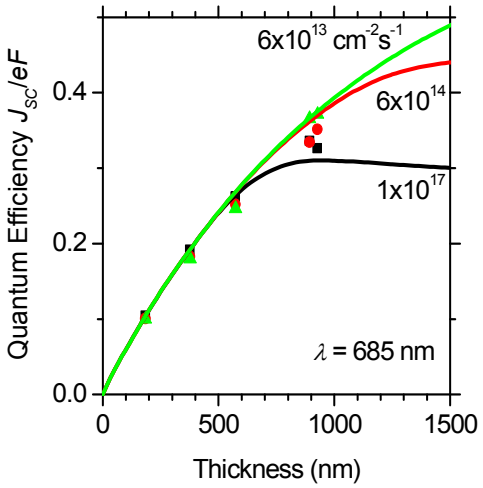

Fig. (3) The symbols indicate quantum efficiency (J_{sc}/eF) measurements for a-Si:H pin solar cells with varying thickness; results are shown for three different fluxes F. The solid lines are results from a bandtail-only calculation. (Intrinsic-layer optical parameters were =6.2×10^{3}cm^{-1}, reflectivities R_f and Rb both 0.2)

In Fig. (4), we have graphed the fill-factor and open-circuit voltage measurements (symbols) and simulations (solid lines) as a function of the incident photon flux. For the fill-factors, results are shown for four different cell thicknesses. We have not shown fill-factor results for the thickest sample; although this sample was only slightly thicker than the thickest one in the illustration, it had a markedly lower fill-factor, and was plainly below the trend of the thickness series.

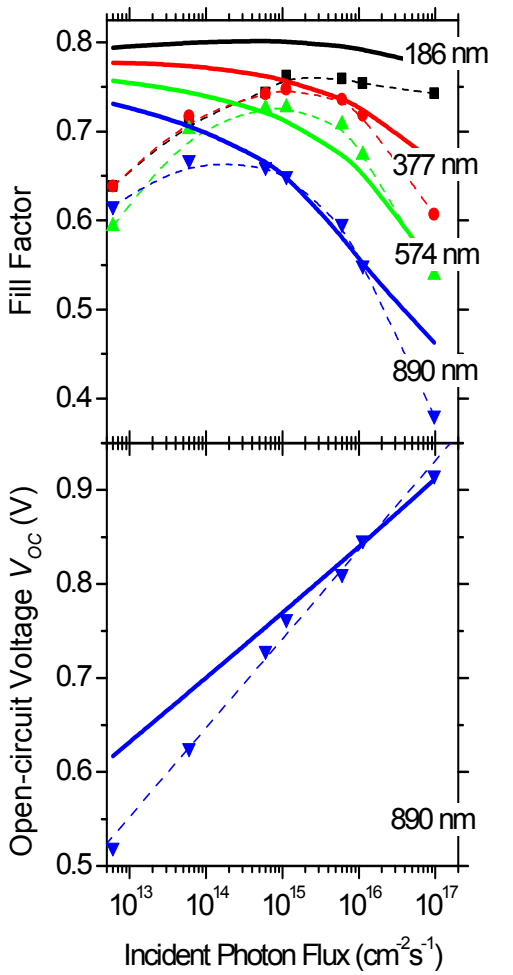

Fig. (4) Symbols indicate the intensity-dependence of the fill-factor and open-circuit voltage V_{OC} measured with uniformly absorbed illumination (685 nm) for a-Si:H pin solar cells. For the fill-factor, results for cells with four different thicknesses are illustrated. The solid lines are the cpredictions for a "valence bandtail only" model; only the optical absorption coefficient was fitted to these measurements

We have shown only a single sample to illustrate the intensity-dependence of the open-circuit voltage V_{OC}; the V_{OC} measurements have very little dependence on thickness, and for simplicity, we have shown these results separately in Fig. (5). For the higher intensities, the fill-factor declines markedly with thickness (from 0.76 to less than 0.4). The decline corresponds fairly accurately with the results of the simulations, and we are therefore fairly confident in the following qualitative explanation for the effect of thickness [3]. We start with the fact that holes have far smaller drift-mobilities than electrons; it thus takes much longer (following their photogeneration) for them to drift to the p/i interface than it takes for electrons to drift to the n/i interface. However, for thin cells, the internal electric field remains fairly large throughout the cell (even under maximum power conditions and at larger intensities). Even

ISSN 1813-2065

holes that are photogenerated close to the n/i interface are rapidly collected – both because of the larger internal field, and because of the relatively small distance between the n/i and the p/i interfaces. It is worth noting that the model predicts slightly larger fill-factors for thin cells than we measured; we don't know the reason for this (small) discrepancy.

For thicker cells, the internal electric field no longer extends across the cell, and some holes photogenerated in the "back" of the cell (i.e. closer to the n/i interface) are lost to recombination. This "collapse" of the field [4] is just a consequence of the buildup of slowly-moving, positively charged holes near the p/i interface. We gain some confidence in this view because we find that reducing the incident flux by a couple of orders of magnitude noticeably improves the fill-factor. The qualitative explanation for this effect is that, for lower incident flux, there are fewer drifting holes, and less positive space-charge to collapse the voltage. The simulations agree fairly well with the measurements for fluxes in the range 10^{15}-10^{17}.

For lower flux ($<10^{15}$cm^{-2}s^{-1}), the measured fill-factors become smaller; this is counter to the trend at high intensities, where the fill-factor decreases with increasing intensity. Furthermore, there is little difference in fill-factor for varying thickness. We do not presently have a successful model for these low-flux effects.

The bottom panel of Fig. (4) shows the intensity-dependence of the open-circuit voltage V_{OC}. The "bandtail only" model provides a good description of the measurements down to a flux of about 10^{15}cm^{-2}s^{-1}; this is essentially the same range over which the model describes the fill-factor. The corresponding photogeneration rates range from $5\text{x}10^{18}$ to $5\text{x}10^{20}$cm^{-3}s^{-1}. For lower intensities, the bandtail model deviates markedly from the measurements. Previous work by the Penn State group has shown that this low-intensity region is quite strongly affected by light-soaking [4]; we presume that a full description of the solar cell behavior will require the addition of defects to the present "bandtail only" model.

In Fig. (5), we show the thickness-dependence of the open-circuit voltage V_{OC} at several flux levels. V_{OC} is nearly independent of thickness; this essential result also emerges from the bandtail-only simulations, although there are some subtle differences in the behaviors. For thicker samples, it is relatively easy to understand thickness-independence in terms of a "quasi-Fermi level" model [2,4]. In this model, the center region of the intrinsic layer has no drift or diffusion currents; the center region is essentially a neutral photoconductor with distinct electron and hole quasi-Fermi levels E_{Fn} and E_{Fp}, respectively. The sample zones near the p/i interface essentially acts as an electrode to measure the hole quasi-Fermi level of the middle, and the n/i interface serves the same role for the electron quasi-Fermi level.

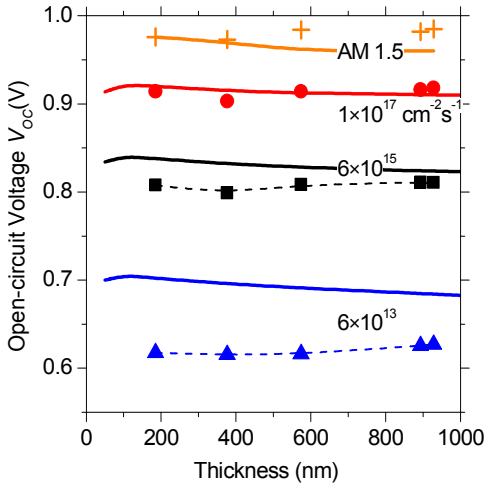

Fig. (5) The symbols represent open circuit voltages V_{OC} measured as a function of thickness for several incident flux levels (white light and 685nm). The solid lines are the results of a "bandtail" only calculation

For the moment, let us accept the validity of the basic idea proposed here: that hole drift mobilities and valence bandtails are the main elements determining the solar conversion efficiency of a-Si:H based solar cells in their a-deposited state. It is also plain that the conversion efficiency in the light-soaked state is markedly reduced from the as-deposited state, and an understanding of the light-soaked state is the ultimate goal for this research.

The role of the present work is to give a solid foundation for exploring the light-soaked state. In the third phase of this project we are making measurements on the same series of solar cells in various states of light-soaking. Surprisingly, we are unaware of any comparable series of published measurements.

We presume that we shall need to incorporate a density of dangling bonds that grows with light-soaking in order to account for the decline in conversion efficiency. We also presume that as-deposited defects will be required to accommodate the low-intensity measurements we have already made. In the spirit of the "bandtail-only" model, we shall be seeking a model with the bare minimum of additional complexity.

There have been several reports of drift-mobility measurements [4-7] in microcrystalline silicon in the last decade or so since it became clear that this material could be prepared with properties that are interesting for solar cells [4].

There is, of course, an enormous range of possible structures in microcrystalline silicon materials. For each sample there is a spectrum of sizes for the component nano and microcrystallites. Even more poorly understood, for each sample there is also a jumble of non-crystalline material that lies between the crystallites. Unsurprisingly, there has also been a very large spread in reported drift mobilities and transport properties.

In this paper we shall first summarize our recent hole drift-mobility measurements in a particular form of microcrystalline silicon that has been developed at Forschungszentrum Jülich as a solar cell absorber, and for which cells with 8.7% conversion efficiency have been reported [6]. We shall not offer a detailed defense of the measurements here, nor shall we offer an extended review and comparison with previous work on microcrystalline silicon; these will be presented elsewhere. Instead, we emphasize an unexpected aspect of the present measurements, which is that they exhibit the features of "exponential bandtail multiple-trapping."

Since its first successful application to amorphous semiconductors in the early 1980's [7], exponential-bandtail multiple-trapping (usually abbreviated as simply "multiple-trapping" or "MT") has become the standard approach to analyzing most transport experiments in hydrogenated amorphous silicon (a-Si:H) and related materials such as amorphous silicon-germanium alloys. The model assumes an exponential bandtail of localized states lying at the bottom of the conduction band, or at the top of the valence band. The application to transport also assumes the existence of a "transport edge," with the property that the only carriers that contribute to electrical transport are those occupying electronic states lying above this edge (for electrons) or below it (for holes); it has generally been assumed that this edge is the "mobility-edge" dividing localized and extended electronic states.

In the present work we have found that multiple-trapping obtains for our measurements in a predominantly crystalline form of microcrystalline silicon. This form of microcrystalline silicon is apparently a far more ordered material than amorphous silicon, and certainly X-ray measurements, Raman scattering, and direct microscopy indicate that most of the volume is associated with small crystallites. One is naturally drawn to models for electrical transport that are based on the effective-mass theory, which would seem to apply at least within a crystallite. Indeed this approach has been applied recently to Hall mobility measurements in n-type microcrystalline silicon [4]. It is thus a bit of a shock to discover that the multiple-trapping model taken from amorphous semiconductors is a better description of microcrystalline silicon than is an effective-mass based approach – but this is the implication of our measurements. The multiple-trapping parameters in the microcrystalline material do differ in interesting ways from those that have been reported for a-Si:H, and we shall return to this comparison in the concluding section of this paper.

The samples used for our measurements were pin structures prepared in designated chambers of a multi-chamber system using plasma-enhanced chemical vapor deposition at frequencies of 95MHz (VHF-PECVD) [8]. We used ZnO coated glass as a transparent, conductive substrate. The μc-Si:H(B) p-layers are about 20nm thick; the films were doped by adding trimethylboron to the silane-hydrogen gas mixture. The intrinsic μc-Si:H layers were prepared using a silane-hydrogen mixture of 5-6%. The n-layer (phosphine doped) was an amorphous a-Si:H(P) layer 30nm thick. As top contacts we used sputtered ZnO dots with diameters of 1-2mm; we plasma-etched (SF_6-gas process) the top surface of these structures to remove the n-layer from regions not under the ZnO.

In this paper we present measurements on three samples summarized in Table (1). To determine the extent of crystallinity, Raman spectra were recorded from the i-layer at spots right next to the ZnO contacts. The integrated intensity ratio $I_C^{RS} = I_C/(I_A+I_C)$ was determined by deconvoluting the spectra into three signal peaks at $480cm^{-1}$, $500cm^{-1}$ and $520cm^{-1}$. The first one can be attributed to a disordered structure like an amorphous phase or grain boundaries (I_A), and the latter two are attributed to the crystalline phase (I_C) [4].

Table (1) Sample Properties

Sample	Raman Ratio I_C^{RS}	i-layer thickness d (μm)
B	0.71	4.0
D	0.60	3.4
E	0.61	4.3

The transient photocurrents were measured in the pin diodes following illumination by a 3ns laser pulse (wavelength of 500nm) through the n-layer. The photocurrent transients were consistent with a conventional interpretation in terms of hole time-of-flight. In particular, the photocharge was independent of the applied voltage, and a transit-time was discernible in the transient. Additionally, the photocurrent at short times was linear in the applied voltage, which is consistent with transport that is linear with electric field.

 ISSN 1813-2065 Printed in IRAQ

In Fig. (6), we present our temperature-dependence measurements of the hole drift-mobility for 3 samples [5] corresponding to a particular "displacement/field" ratio ($d^2/2V$) of $7x10^{-8}cm^2/V$ of sample thickness d and applied field (V/d). The activation energy (0.13eV) is illustrative only, and does not indicate any particular depth for the bandtail traps. These average drift-mobilities, determined using $\mu_D=d^2/(Vt_\tau)$, are much larger than typically obtained in a-Si:H [6], although a direct experimental comparison at the same value for d^2/V is not possible. We compare multiple trapping fitting parameters shortly.

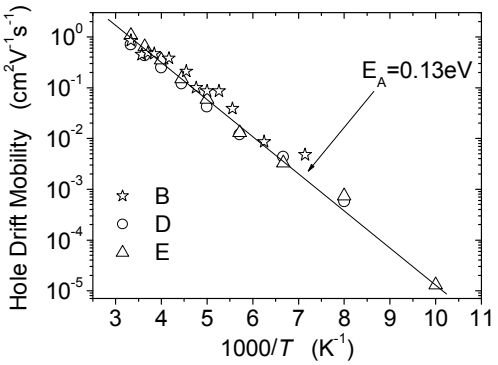

Fig. (6) Hole drift-mobilities measured for three microcrystalline silicon materials (Table 1) determined with a displacement/field ratio $d^2/2V=7.8x10^{-8}cm^2/V$

Our procedure for fitting to the multiple-trapping model starts with the transient photocharge $Q(t)$ (the time-integral of the photocurrent $i(t)$). In particular, we fit to the time-dependence of the normalized photocharge $Q(t)d^2/Q_0(V-V_{bi})$, where Q_0 is the total photocharge of holes generated by the laser pulse, V is the bias voltage, d is the i-layer thickness, and V_{bi} is a correction for the internal field. We have illustrated the photocharge measurements in Fig. (1) for seven temperatures. For clarity, we have removed sections of the transient for $Q(t)>Q_0/2$; these portions of the transient are past the "transit time," and are not used in our multiple-trapping fitting procedure. We have also removed early-time portions of the transients that are clearly dominated by response-times of the measurement.

The solid lines in Fig. (7) are the multiple-trapping fittings. The actual equation that was fitted to the normalized photocharge is [1]:

$$L(t)/E = K\left(\frac{\mu_0}{\nu}\right)(\nu t)^{\alpha(T)} \qquad (1)$$

where $L(t)$ is the mean displacement for photocarriers after a delay time t and with electric field E. The dispersion parameter $\alpha=KT/\Delta E_V$, where ΔE_V is the width of the exponential, valence bandtail, μ_0 is the valence band-mobility, and ν is an "attempt-to-escape" frequency characterizing the rate of release of holes from the bandtail traps. The constant $K=\sin(\alpha\pi)/(\alpha\pi(1-\alpha))$ is of order unity. The multiple-trapping parameters we chose (and that are the basis for the solid lines shown in Fig. 1) are given in Table (2) below, along with some results for a-Si:H [1,7].

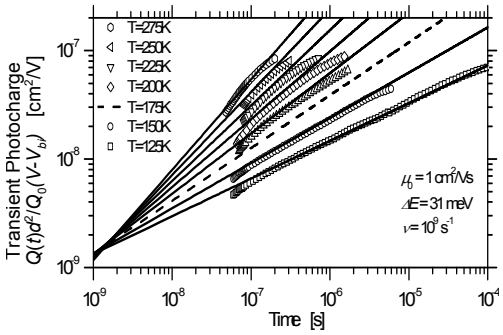

Fig. (7) The symbols are normalized photocharge transients measured in one microcrystalline silicon sample ("D" in Table 1); the solid lines are the corresponding calculations using the exponential bandtail multiple-trapping model with the parameters indicated

Table (2) Multiple-trapping fitting parameters

Multiple-trapping parameter	μc-Si:H (this work)	a-Si:H [17]	a-Si:H [18]
Valence band-mobility μ_0 (cm^2/Vs)	1.0	0.7	0.3
Bandtail width ΔE_V (meV)	31	45	48
Attempt-frequency ν (s^{-1})	$9x10^8$	$1x10^{12}$	$8x10^{10}$

One approach to analyzing mobilities in polycrystalline materials is to invoke the effective masses that would obtain for electrons and holes in the single crystal, and assume that the grain boundaries act as scatterers or barriers and as the locus for traps for the carriers [9]. It is instructive to use this approach crudely to calculate an "effective-mass carrier mobility" for holes $\mu_h^{e.m.}$ utilizing the expression $\mu_h^{e.m.}=v_{th}l/(kT/e)$, where v_{th} is the "thermal velocity" for holes (about 10^7cm/s in c-Si near room-temperature) [1] and l is a scattering length. If the scattering length is identified with a typical crystallite size of 3nm, we infer $\mu_h^{e.m.}=120cm^2/Vs$, or about 100 times larger than the estimate in Table (1). The effects of traps and barriers seem unlikely to explain the discrepancy for our samples, since these were already (implicitly) incorporated in the analysis that led to the estimate $\mu_0=1cm^2/Vs$.

We suggest that, for our samples of microcrystalline silicon, the disorder is sufficient to strongly alter the bandedge states from their

crystalline counterparts. In particular, we suggest that the bandedge states of the crystal have been transformed into a bandtail (i.e. that the density-of-states $g(E)$ has been altered), and that a mobility-edge has formed within the bandtail [10] (i.e. states lying deeper in the energy gap are localized).

The mobility-edge has been widely applied to amorphous semiconductors [11,12], and has recently been applied to microcrystalline samples with a larger fraction of amorphous "tissue" [13]. Here we are suggesting that it be applied to samples that are predominantly crystalline. In the mobility-edge model, hole states with energy levels below the mobility-edge ($E<E_V$) are completely delocalized (by definition), although with very different wavefunctions than the effective-mass states of crystals. Hole states lying above the mobility-edge ($E>E_V$) are localized. Both analytical and computational studies of mobility-edges [14,15] indicate that the localization radius for a hole state grows very rapidly, and may even diverge, as the state's energy approaches the mobility-edge. It isn't clear theoretically how particular atomic-scale features such as "strained bonds" are incorporated into the bandtail states.

With this perspective, we first discuss the bandtail width ΔE_V. The estimate of 31meV for the microcrystalline material seems unremarkable in the context of work on holes in amorphous silicon, which yield values in the range 40-50meV. It is worth noting that disorder affects holes and electrons very differently. The conduction bandtail in amorphous silicon has a width around 22meV [12,16]. Electron properties in samples quite similar to the present ones have been studied using post-transit time-of-flight [17]; bandtail multiple-trapping did not apply for these transients. An interesting possibility is therefore that electron transport may be governed by effective masses in exactly the same material for which holes require a mobility-edge approach.

The fact that the hole band-mobility μ_0 is about the same in the present microcrystalline samples and in amorphous silicon seems to support the mobility-edge interpretation, and more broadly suggests that a value near 1 cm^2/Vs may be a universal property of a mobility edge. Such "universality" is also suggested by the fact that electron band-mobilities in amorphous silicon are also around $1cm^2/Vs$ [12,16]. Interestingly, a band mobility of $1cm^2/Vs$ is not an obvious implication of the existing theoretical treatments of mobility-edges.

Finally, we turn to the attempt-frequency ν. It is quite interesting that the value for microcrystalline silicon is substantially (about 100 times) smaller than the lower values reported for a-Si:H. However, even for a-Si:H, there is no well-accepted physical interpretation for this parameter. One often-mentioned interpretation is that ν be identified as a "typical phonon frequency," but this association fails to explain either the very low magnitudes or the enormous range of magnitudes that have been reported experimentally [12]. Yelon and Movaghar have suggested that multi-phonon effects lead to the variations, and this perspective has been applied by Chen *et al.*, to drift-mobility measurements [18]. Another possibility originating with high-field drift-mobility measurements in a-Si:H has been that ν reflects the bandedge density-of-states $g(E_V)$ [19], which suggests that the present measurements be interpreted as indicating a substantially lower value for $g(E_V)$ in microcrystalline than in amorphous silicon. Plainly, we need more clues from experiment about the meaning of this parameter; it seems possible that its dramatic lowering in microcrystalline silicon could be providing it.

4. Conclusion

In this article, we present the status of three projects; amorphous silicon solar cell characteristics and modeling, hole drift mobility measurements in microcrystalline and amorphous silicon, and hole-conducting polymers as p-layer materials for amorphous and crystal silicon solar cells. In the present work we have found that multiple-trapping obtains for our measurements in a predominantly crystalline form of microcrystalline silicon.

References

[1] S. Dinca, G. Ganguly, Z. Lu, E.A. Schiff, V. Vlahos, C.R. Wronski and Q. Yuan, in Amorphous and Nanocrystalline Silicon Based Films, edited by J.R. Abelson, G. Ganguly, H. Matsumura, J. Robertson, E.A. Schiff (Materials Research Society Symposium Proceedings Vol. 762, Pittsburgh, 2003), 343.

[2] K. Zhu, J. Yang, W. Wang, E. A. Schiff, J. Liang and S. Guha, in Amorphous and Nanocrystalline Silicon-Based Films, edited by J.R. Abelson, G. Ganguly, H. Matsumura, J. Roberstson, and E.A. Schiff (Materials Research Society Proceedings Vol. 762, Pittsburgh, 2003), 297.

[3] R.E.I. Schropp and M. Zeman, "Amorphous and Microcrystalline Silicon Solar Cells: Modeling, Materials, and Device Technology", Kluwer Publishing Ltd. (Boston) (1998).

[4] E.A. Schiff, *Solar Ener. Mater. Solar Cells*, 78 (2003) 567-595.

 ISSN 1813-2065 Printed in IRAQ

[5] Q. Wang, R.S. Crandall and E.A. Schiff, in Conference Record of the 21st Photovoltaics Specialists Conference (IEEE, 1996), 1113.
[6] J. Pearce, R. Koval, A. Ferlauto, R. Collins, C. Wronski, J. Yang and S. Guha, *Appl. Phys. Lett.*, 77 (2000) 19.
[7] T. Tiedje, *Appl. Phys. Lett.*, 40 (1982) 627.
[8] O. Vetterl, A. Dasgupta, A. Lambertz, H. Stiebig, F. Finger and H. Wagner, Mater. Res. Soc. Symp. Proc., 664 (2001) A25.8.
[9] T. Weis, R. Lipperheide, U. Wille and S. Brehme, *J. Appl. Phys.*, 92 (2002) 1411.
[10] G. Juška, M. Viliūnas, K. Arlauskas, N. Nekrašas, N. Wyrsch and L. Feitknecht, *J. Appl. Phys.*, 89 (2001) 4971.
[11] M. Serin, N. Harder and R. Carius, J. Mater. Sci.: Materials in Electronics 14 (2003) 733.
[12] T. Tiedje, in Hydrogenated Amorphous Silicon II, edited by J.D. Joannopoulos and G. Lucovsky (Springer-Verlag, New York, 1984), pp. 261-300.
[13] T. Dylla, F. Finger, E. A. Schiff, *unpublished results*.
[14] J. Meier, R. Flückiger, H. Keppner and A. Shah, *Appl. Phys. Lett.*, 65 (1994) 860.
[15] O. Vetterl, A. Dasgupta, A. Lambertz, H. Stiebig, F. Finger and H. Wagner, Mater. Res. Soc. Symp. Proc., 664 (2001) A25.8.
[16] Q. Wang, H. Antoniadis, E.A. Schiff and S. Guha, *Phys. Rev. B*, 47 (1993) 9435.
[17] S. Reynolds, V. Smirnov, C. Main, R. Carius and F. Finger, in Amorphous and Nanocrystalline Silicon Based Films, edited by J.R. Abelson, G. Ganguly, H. Matsumura, J. Robertson, E.A. Schiff (Materials Research Society Symposium Proceedings Vol. 762, Pittsburgh, 2003), 327.
[18] T. Weis, R. Lipperheide, U. Wille and S. Brehme, *J. Appl. Phys.*, 92 (2002) 1411.
[19] L. Houben, M. Luysberg, P. Hapke, R. Carius, F. Finger and H. Wagner, *Phil. Mag. A*, 77 (1998) 1447.

This Month in Physics History

March 21, 1768
Birth of Jean-Baptiste Joseph Fourier


Jean-Baptiste Joseph Fourier

The human ear splits incoming sound waves into their component frequencies through mechanical means by exploiting natural resonances: namely, different nerve endings in our ears are sensitive to different frequencies. But it is also possible to analyze a sound mathematically to determine its component frequencies. This can be done thanks to a method, devised by an 18th century French mathematician named Jean-Baptiste Joseph Fourier, known as a Fourier transform.

Born on March 21, 1768, Fourier was the son of a tailor in the village of Auxerre. Orphaned by age 10, the young Joseph received an early rudimentary education at a local convent, thanks to a recommendation by the local bishop, and he proved such an apt pupil he went on to study at the Ecole Royale Militaire of Auxerre. There he fell in love with mathematics. By 1790 Fourier was teaching at his alma mater.

Revolution was brewing in France. Fourier was sympathetic at first to the cause, drawn by "the natural ideas of equality," and a hope "of establishing among us a free government exempt from kings and priests." He joined his local Revolutionary Committee, but soon regretted it, as the ultra-violent Reign of Terror gripped France and thousands of nobles and intellectuals fell victim to the guillotine.

Fourier made the mistake of defending the stance of his own Auxerre faction before a rival sect while on a trip to Orleans. In July 1794, he was arrested and imprisoned for the views he'd expressed on that trip, and found himself facing the guillotine. But with the death of Maximilien Robespierre, the Revolution lost steam and Fourier and his fellow prisoners were freed. Fourier was selected for a new teacher-training school to help rebuild France, where he studied under three of the most prominent French mathematicians: Joseph-Louis Lagrange, Pierre-Simon Laplace, and Gaspard Monge. By September 1795, Fourier was teaching at the prestigious École Polytechnique.

A few years after his academic appointment, he joined Napoleon's army as a scientific advisor when Napoleon invaded Egypt, engaging in archaeological expeditions and helping found the Cairo Institute as Napoleon's military fortunes waxed and waned.

By 1801, Fourier was back in France, teaching, until Napoleon appointed him prefect in Grenoble. He promptly stirred up a mathematical controversy with his conclusions about his experiments on the propagation of heat. The culprit was an equation describing how heat traveled through certain materials as a wave. He based his reasoning in part on Newton's law of cooling: the flow of heat between two adjacent molecules is proportional to the difference of their temperatures. Fourier concluded that every wave-like "signal," no matter how complex, can be represented by adding together many different waves. In other words, complicated periodic functions – whether continuous or discontinuous – can be expanded and written out as simple waves mathematically represented by sines and cosines.

Fourier completed his memoir, *On the Propagation of Heat in Solid Bodies*, in 1807 and read it to the Paris Institute on

ISSN 1813-2065 Printed in IRAQ

December 21 of that year. The reception was mixed. Both Lagrange and Laplace objected to the notion of what we now call Fourier series: the expansions of functions as trigonometrical series. Along with another scientist, Jean-Baptiste Biot, they also objected to Fourier's derivation of the equations of transfer of heat. (Biot had written an earlier paper on the topic in 1804, although that paper proved incorrect.)

Nonetheless, when the Paris Institute held a competition on the topic of how heat propagates in solid bodies in 1811, Fourier submitted his memoir for consideration. He won the prize, in part because only one other entry was received. The selection committee (which included Lagrange and Laplace) recorded their reservations in their report: "The manner in which the author arrives at these equations is not exempt of difficulties and… his analysis to integrate them still leaves something to be desired on the score of generality and even rigor."

Because of the controversy, Fourier's memoir was not published until 1822, after his election to the Academie des Sciences in 1817, and the same year he became the Academie's secretary. His work did contain flaws, but it also provided the basis for later work on trigonometric series and the theory of functions of a real variable, most notably the Fourier transform, an operation that turns one function of a real variable into another. It is widely used in digital signal processing, as well as in the physical study of wave motion and optics.

Fourier's other claim to fame is the discovery in 1824 of the "greenhouse effect": namely, that certain gases in Earth's atmosphere could trap heat from the sun instead of having it radiate back into space, thereby increasing the surface temperature of Earth. He was inspired by an earlier experiment with so-called "hot boxes" by Horace-Benedict de Saussure, in which a wooden box lined with black cork was exposed to sunlight. De Saussure then inserted three small panes of glass into the cork, and noted that the temperature rose in those compartments closer to the center of the box. However, de Saussure did not have a solid theory for this observed effect. Fourier rightly surmised that Earth gains energy from numerous sources, most notably solar radiation causing an increase in temperature, and that Earth also radiates energy via infrared radiation (which he called *chaleur obscure*, or "dark heat"), and that a balance must be maintained between heat gain and heat loss. He incorrectly assumed that a significant amount of radiation from interplanetary space contributed to the greenhouse effect, but grasped that the rate of infrared radiation increased with Earth's temperature. This latter insight was mathematically defined 50 years later with the Stefan-Boltzmann law, further refined by Planck's law 20 years after that.

Fourier continued to publish papers on mathematics until his death in 1830, when he tripped and fell down the stairs at home. His tomb is in the Pere Lachaise Cemetery in Paris, decorated with an Egyptian motif in honor of his position as secretary of the Cairo Institute.

Edited by
Oday A. Hamadi
IJAP, Managing Editor

Extraction of Doping Profile in Substrate of MNOS capacitor Using Fast Voltage Ramp Deep Depletion C-V method

Abdulghefar K. Faiq

Department of Physics,
College of Science,
University of Salahaddin,
Erbil, Kurdistan Region, Iraq

Two MNOS C-V profiling methods are presented; the conventional C-V profiling, and deep depletion (DD) C-V, the former shows a lack of information at the onset of inversion mode, while the latter can be achieved by the application of high speed voltage ramp of sweep rate equals 1MV/s on the MNOS gate, meanwhile monitoring the current response of the time varying voltage, the entire DD C-V curve is traced on CRO screen with suitable DC voltage bias. The results show that doping profile can be extended 1μm deeper inside the silicon, i.e., ten times of Debye's length, hence more accurate results can be achieved. Interface states densities have small effect on final doping profile, and doping reaches approximately a constant value deep inside the silicon compatible with experimental part.

***Keywords*:** Semiconductor devices, Doping profiling, MNOS, Deep depletion
Received: 30 October 2009, **Revised**: 4 March 2010, **Accepted**: 11 March 2010

1. Introduction

Metal-Nitride-Oxide-Semiconductor (MNOS) capacitor is the essential part in non-volatile memory, it is also used as a passive coating due to its high resistivity, and higher dielectric constant compared to silicon dioxide [1,2]. The calculation of doping profile is important to understand the characteristics of shrunken device, such as the device conductivity which is very sensitive to doping variation near the silicon substrate [1,3]. There are several methods to extract impurity distribution pattern, the simplest, and the non–destructive one is the Capacitance-Voltage (C-V) method [4].

Over the years many researches on C-V profiling has, in general, remained limited to MOS [5]. In this work we try, to examine the suitability of C-V technique to deduce doping distribution under the oxide of MNOS structure, and to obtain deep depletion C-V curve in such devices in order to extend the profile deep inside the silicon substrate.

The C-V profiling is essentially a measurement of free hole concentration $p(x)$ -for p-type silicon- rather than of the real doping concentration $N_a(x)$ of semiconductor. Whenever space charge are present, the two are not the same, but deep inside the semiconductor substrate, $p(x)$ will eventually become flat, and $p(x) \rightarrow N_a(x)$ [6]. It is worth to note that in spite of the above mentioned limitation concerning the validity of the C-V profiling, this technique proves to be very useful for determining various doping profiles in semiconductors [7].

2. Theoretical bases

The typical MNOS structure and its C-V curves at low frequency, high frequency, and deep depletion (DD) are shown in Fig. (1). C-V curves span the accumulation to the depletion modes [8]. The capacitance of MNOS structure at high frequency can be represented by two capacitors in series [9]:

(1) The insulator capacitance (C_i) which in turn is composed of a series combination of two capacitances; silicon nitride capacitance (C_n), and silicon dioxide capacitance (C_o).
(2) The silicon depletion-region capacitance C_d.

In our MNOS structure, the oxide thickness is 2nm and silicon nitride thickness is 171nm, the C_i of MNOS structure is given by:

$$C_i = \frac{C_o C_n}{C_o + C_n} \quad (1)$$

$$C_o = \frac{\varepsilon_{ox}\varepsilon_o}{d_o} \quad (2)$$

where ε_{ox} is the relative dielectric constant of silicon dioxide (=3.9) and d_o its thickness

$$C_n = \frac{\varepsilon_n \varepsilon_o}{d_n} \quad (3)$$

where ε_n is the relative dielectric constant of silicon nitride which is between 6 and 7 [10], and d_n is the nitride layer thickness

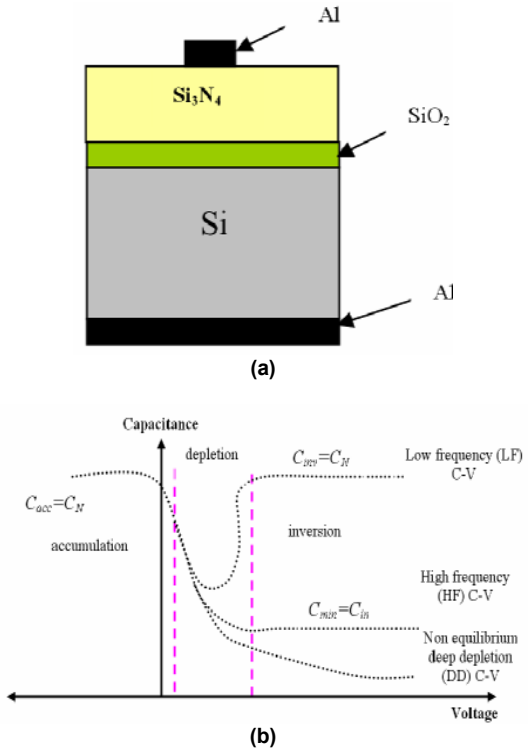

Fig. (1) (a) ideal MNOS structure, (b) ideal HF, LF and deep depletion (DD) C-V curves

In our case, the nitride layer thickness is about 50 times greater than silicon dioxide layer thickness; we can approximate Eq. (1) to:

$$C_i = C_n \tag{4}$$

Hence, the measured MNOS capacitance (C_m) is equal to:

$$C_m = \frac{C_n C_d}{C_n + C_d} \tag{5}$$

$$C_d = \frac{C_m + C_n}{C_n - C_m} \tag{6}$$

where C_d is the depletion capacitance and given by:

$$C_d = \frac{\varepsilon_s \varepsilon_o}{w} \tag{7}$$

where w is the depletion width and ε_s is silicon relative dielectric constant (=11.9)

The depletion capacitance changes with voltage from a maximum at which the total capacitance is equal to C_n, toward a minimum of C_{min} when the depletion depth is maximum w_m, and the capacitance curve reach its minimum C_{min}, Fig. (1b). We can calculate C_{dmin} from the C-V curve at C_{min} by substituting the value of C_{min} in Eq. (6) and calculating C_d equals to C_{dmin} [11].

The depletion approximation method of doping profile is [7]:

$$N(w) = 2[q\varepsilon_s\varepsilon_o \frac{d(\frac{1}{C_m^2})}{dV}]^{-1} = -\frac{C_m^3}{q\varepsilon_o\varepsilon_s}(\frac{dC_m}{dV})^{-1} \tag{8}$$

This equation shows that the doping concentration $N(w)$ can be calculated from the slope of $(1/C_m^2)$ *vs.* V curve. The above relation is considered to be the free carrier concentration, more specifically, when the true hole concentration $p(x)$ varies by an appreciable fraction over a distance less than an extrinsic Debye length:

$$L_D = (\frac{\varepsilon_s\varepsilon_o kT}{q^2 p})^{\frac{1}{2}} \tag{9}$$

where q is the electron charge, and the measured apparent hole concentration is an average $p(x)$ taken over a distance of this order [6]

Rewriting Eq. (8), replacing w with x, and $N(w)$ with p(x) to mathematically relate the measured capacitance C_m of the MNOS structure and the majority carrier distribution $p(x)$:

$$p(x) = 2[q\varepsilon_s\varepsilon_o \frac{d(\frac{1}{C_m^2})}{dV}]^{-1} \tag{10}$$

Following the derivation in [12], by introducing the effect of stretch out of C-V curve caused by interface states, the interface states corrected hole profile $p'(x)$ is obtained:

$$p'(x) = 2(\frac{1-\frac{C_{LF}}{C_n}}{1-\frac{C_{HF}}{C_n}})[q\varepsilon_s\varepsilon_o \frac{d(\frac{1}{C_m^2})}{dV}]^{-1} \tag{11}$$

Kennedy *et al.* [13] developed a simple mathematical formula which expresses the doping as a function of free carrier concentration in one dimension, following their derivation but for holes rather than electrons because electrons were their majority carriers:

The electric current within this material due to both drift and diffusion of majority holes is given by:

$$J_p = qD_p\frac{dp}{dx} - qp\mu_p\frac{d\Psi}{dx} \tag{12}$$

where J_p is hole current density, D_p is holes diffusion constant, μ_p is holes mobility, and Ψ is the electric potential

Einstein relation states that:

$$\frac{D_p}{\mu_p} = \frac{kT}{q} \tag{13}$$

An electric current of zero implies that the diffusion and drift terms in Eq. (12) are of equal magnitude, but in the opposite direction; hence, from equations (12) and (13), an electric field $E(x)$ is obtained:

$$E(x) = -\frac{d\Psi}{dx} = \frac{-kT}{q}\frac{1}{p(x)}\frac{dp(x)}{dx} \tag{13}$$

where k is Boltzmann's constant, and T is absolute temperature

Equation (14) establishes the electric field distribution necessary to maintain an electric current of zero in p-type material containing local variations of holes density. Assuming

extrinsic semiconductor material (the minority carrier density has negligible influence upon the structure under consideration), we have from Poisson's equation

$$\frac{dE}{dx} = -\frac{q}{\varepsilon_s \varepsilon_o}[p(x) - N_a(x)] \quad (15)$$

The divergence of the electric field, in Eq. (14) is determined by both the impurity atom distribution $N_a(x)$ and the majority carrier distribution $p(x)$, by combining equations (14) and (15) we obtain:

$$\frac{-kT}{q}\frac{d}{dx}\{\frac{1}{p(x)}\frac{dp(x)}{dx}\} = \frac{q}{\varepsilon_s \varepsilon_o}[N_a(x) - p(x)] \quad (16)$$

and therefore

$$N_a(x) = p(x) - (\frac{\varepsilon_s \varepsilon_o}{q})(\frac{kT}{q})\frac{d}{dx}[\frac{1}{p(x)}\frac{dp(x)}{dx}] \quad (17)$$

Equation (17) rigorously relates the desired impurity atom distribution $N_a(x)$ to the measured majority carrier distribution $p(x)$. In order to extend doping profile deeper inside the silicon, we must obtain deep depletion DD C-V curve. When the gate bias is swept from accumulation into the inversion region too fast for minority carrier (electrons) to follow, the charge neutrality must be satisfied by the ionized acceptor alone, therefore, the depletion width become broader than that in thermal equilibrium, and the capacitance decreases below its thermal equilibrium saturation value (C_{inv}). Such a non-equilibrium condition is called deep depletion [14]. Usually deep depletion can be achieved by increasing the voltage bias sweep rate in the C-V measurement (high enough that not allow the creation of minority electrons).

3. Material and experimental technique

The measured device is MNOS structure. p-type (100) silicon wafer of resistivity 5-10 Ω.cm is used with approximately doping of about $2x10^{15}cm^{-3}$. Native SiO_2 layer of thickness ~2nm is formed, Si_3N_4 layer is deposited by using of Low Pressure Chemical Vapor Deposition (LPCVD) method, the thickness is 171nm measured by ellipsometry. Aluminum is used as front and back contacts. The front contact is deposited at low pressure of $5x10^{-6}$ mbar across suitable mask of area $0.01cm^2$ using Edward 306 A coating system. The back contact is deposited without mask.

Two methods of C-V measurements are performed:

(1) The conventional C-V measurement is performed on FLUKE PM 6306 programmable Automatic RLC Meter. The voltage sweep bias is supplied by Keithly Pico-Ammeter/DC Voltage Source Model 6487. Electrical contacts are made by pressing the metallic gate using a spring clip arrangement.

(2) The DD C-V measurement is achieved by the application of high speed saw tooth voltage on MNOS sample provided by TEKTRONIX FG 502-11MHz Function Generator. The DD C-V curve is traced on the screen of TEKTRONIX (1GHz) TDS 5104 Digital Phosphor Oscilloscope, which has the ability of saving and exporting the wave form to MATLAB for mathematical operations. The voltage bias is supplied by the same previous Kiethly DC voltage source for returning flat-band voltage to the origin of the scope's screen. Whole measurements are performed in dark at room temperature 300K. A full description of this circuit with an example of C-V curve as shown on the CRO screen is given in the appendix.

4. MATLAB (6.5) Algorithm

The following MATLAB Algorithm is designed for the determination of doping profile

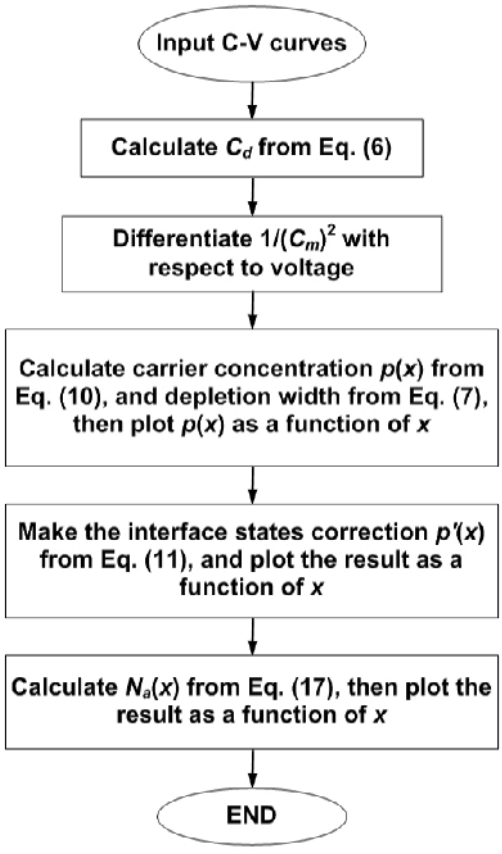

5. Results and Discussion

Figure (2) shows the 1MHz C-V curve of MNOS sample, in which the scan is initiated at voltage of -20V in accumulation mode towards the inversion with sweep rate of α=3V/s. Nitride's capacitance per unit area C_n is calculated from the accumulation and its equal to $2.375x10^{-8}F/cm^2$. The flat-band voltage (V_{FB}) is

also calculated and it is equal to -16.8V using $0.9C_{acc}$ rule. The rule which states that: flat band capacitance C_{FB} is equal to 90% of accumulation capacitance C_n [15].

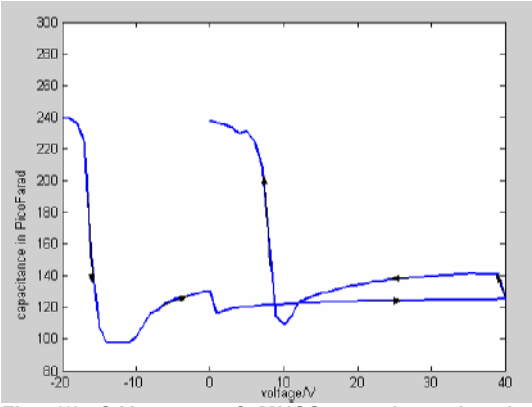

Fig. (2) C-V curve of MNOS sample under the application of voltage ramp of sweep rate (3V/s) from accumulation (-ve voltages) to deep inversion (+ve voltages), and then in the reverse direction

The curve which shows an increase of capacitance in strong inversion as a result of formation of certain amount of interface state tarps because of the large DC field stress ~1.2x10^{6}V/cm [16,17], then we record a constant capacitance till the end of the scan(+40V), like an ideal C-V curve. In the reverse direction we notice two effects: the first one is another increase of capacitance as a result of creation of interface state traps; the second one is that we get the flat–band condition at +7V, this results in a memory window of 23.8V, which indicates that electrons are tunneled across the silicon dioxide and then trapped in the silicon nitride layer [18].

Figure (3) is the conventional C-V curves of MNOS capacitors at frequencies (10 kHz, 100 kHz and 1 MHz), the DC sweep rate is the same for all frequencies α=3V/s.

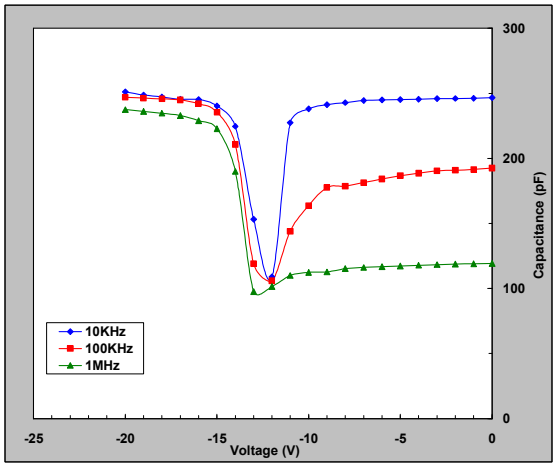

Fig. (3) Three C-V curves at 10 kHz, 100 kHz and 1MHz. The sweep rate is the same (3V/s)

The 10kHz curve shows an increase in the inversion capacitance toward C_n like the case of standard LF C-V curve. The shape of C-V curve, whether it takes HF or LF shape, depends on minority carriers lifetime [9]. When the life time is long, the C-V curve takes LF shape in very low frequencies, as low as possible; to the degree the minority carriers could follow the ac signal, i.e., quasi-static. But as we will show later, it is obvious that minority carrier life time is so small that we have LF C-V curve even at 10 kHz.

5.1 Deep Depletion

It is necessary to extend the profile deeper inside the silicon substrate in order to get more accurate information about doping concentration change with depth, and thus for: first, the conventional doping profile is limited to small depths inside the silicon - that is, calculated in our case as 0.6μm, and valuable information about the exact doping can not be achieved in such small depths. Second, the change in majority carriers, actually measured by C-V profiling, limits the resolution of the differential capacitance method to distances comparable to the local extrinsic Debye length [6,19]. We calculate L_D using Eq. (9) for N_A=2x10^{15}cm^{-3}, as 0.09μm.

Figure (4) shows LF (10 kHz), HF (1MHz), and DD C-V curves. The DD C-V curve is obtained by using the circuit given in the appendix. The transient C-V curve can be achieved directly by measuring MNOS current response to a very fast voltage ramp of sweep rate of 1MV/s, this current response is proportional to the differential capacitance and carries information on the doping density [8]. Thus, as it was mentioned previously, the large sweep rate (α=10^{6}V/s) indicates that the minority carrier life time is very small [12].

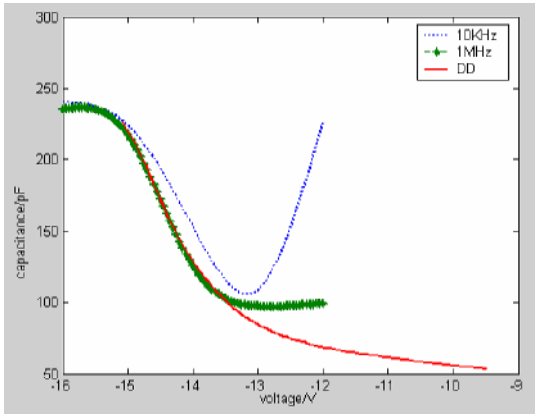

Fig. (4) Three MNOS C-V curves 10 kHz, 1 MHz and DD, the sweep rate for the first two curves is the same (3V/s), while for DD curve it is 1MV/s

5.2 Calculation of Doping Profile

The majority hole profile from the surface toward the bulk of p-type silicon substrate is calculated by Eq. (10) using conventional C-V,

and DD curves as its shown in Fig. (5). DD C-V profile provides additional 1μm deeper inside the silicon compared to the conventional differential C-V profile. At onset of inversion, the calculation of hole profile is not accurate [12], that is why we see a rapid increase of hole density.

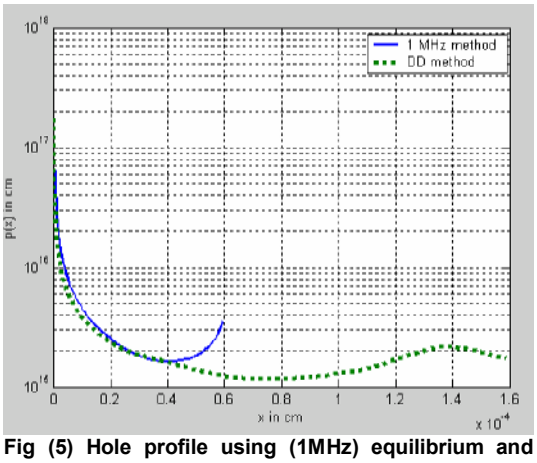

Fig (5) Hole profile using (1MHz) equilibrium and deep depletion (DD) method

Figure (6) shows the comparison between the interface state density correction of hole profile $p'(x)$ using Eq. (11) with hole profile $p(x)$. The two are approximately of the same value, therefore we can ignore the effect of interface state in our calculations. The graph shows a decrease in hole density when we go deeper inside the silicon which is similar to the change in doping density calculated from Eq. (17), as it is shown in Fig. (7).

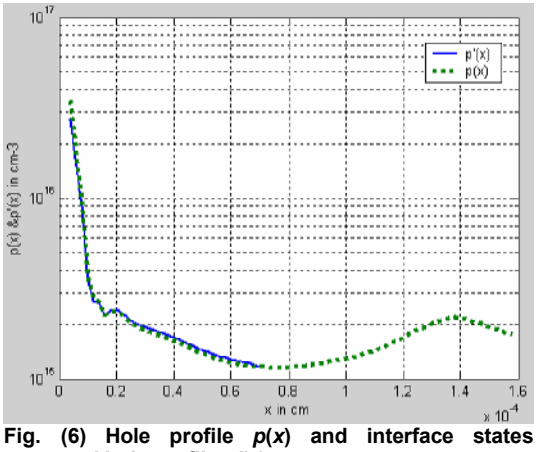

Fig. (6) Hole profile $p(x)$ and interface states corrected hole profile $p'(x)$

In this curve $p(x)$, $p'(x)$ and the doping densities $N_a(x)$ reach approximately a constant value of about $2x10^{15}cm^{-3}$. The reason behind the change in doping at the surface is that thermal oxidation of silicon moves dopant ions from their equilibrium positions [12]. Moreover, the thermal deposition of the Si_3N_4 layer may cause additional rearrangement of the dopant ions. Deeper inside the silicon, the hole density is seemed to be an average of charge density profile. The interface state correction terminates at about 0.6μm because the LF C-V measurement's lowest capacitance is $1.096*10^{-8}$ F/cm^2 corresponds to depletion width of 0.6μm by using equations (5) and (6), while the lowest DD capacitance is at $0.52x10^{-8}F/cm^2$ corresponds to depletion width of 1.5μm, that is why we cannot extend the interface state correction of hole profile $p'(x)$ to distances greater than 0.6μm.

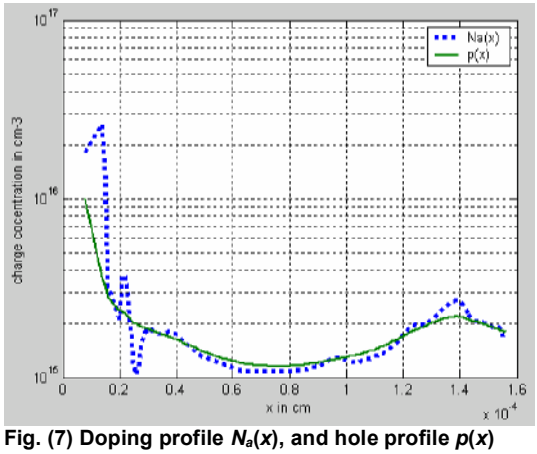

Fig. (7) Doping profile $N_a(x)$, and hole profile $p(x)$

6. Conclusions

C-V technique gives suitable information about impurity charge distribution near and the surface of silicon substrate of MNOS device. A deep depletion DD MNOS C-V curve was obtained by the application of high speed voltage ramp of sweep rate of (10^6V/s), and the current response of such voltage ramp is monitored. It was found that interface states densities have negligible effect on the calculation of doping profile. Doping profile decrease with going deep into the silicon bulk reaching approximately a constant value of $2x10^{15}cm^{-3}$.

References

[1] J.R. Elmiger and M. Kunst, *Appl. Phys. Lett.*, 69(4) (1996) 517-519.
[2] T.P. Ma, *IEEE Trans. Electron Devices*, 45(3) (1998) 680-690.
[3] J. Heo et al., *Mater. Sci. and Eng. B*, 124-125 (2005) 301-304.
[4] A. Pirovano et al., *IEEE Trans. Electron Devices*, 48(4) (2001) 750-757.
[5] F. Recart and A. Cuevas, *IEEE Trans. Electron Devices*, 53(3) (2006) 442-448.
[6] H. Kroemer and W.Y. Chien, *Solid State Electron.*, 24 (1981) 655-660.
[7] A.F. Yaremchuk, *Appl. Phys. A*, 73 (2001) 503-509.
[8] R.C. Hughes, R. Bastasz and W.P. Ellis, *Appl. Surf. Sci.*, 115 (1997) 74-79.
[9] R.F. Pierret, **"Semiconductor Device Fundamentals"**, Addison-Wesley

Publishing Co., Inc. (USA) (1996), Ch. 16, 587-591, 595-598.
[10] S.M. Sze, **"VLSI Technology"**, McGraw-Hill Book Co. (Singapore) (1988), Ch. 6, 259-263.
[11] S.M. Sze and K.N. Kowk, **"Physics of Semiconductor Devices"**, John-Wiley & Sons, Inc. (NJ, USA) (2007), Ch. 4, 202-209.
[12] E.H. Nicollian and J.R. Brews, **"MOS Metal Oxide Semiconductor Physics and Technology"**, John-Wiley & Sons, Inc. (NJ, USA) (2003) Ch. 9, 387-390, 375-380, Ch. 14, 721-731.
[13] D.P. Kennedy and R.R. O'Brien, *IBM J. Res. Develop*., (1968) 212-214.
[14] C.Y. Liu, B.Y. Chen and T.Y. Tseng, *J. Appl. Phys*., 95(10) (2004) 5602-5607.
[15] D.K. Schroder, **"Semiconductor Material and Device Characterization"**, John-Wiley & Sons, Inc. (NJ, USA) (2006), Ch. 6, 328.
[16] S. Minami and Y. Kamigaki, *IEEE Trans. Electron. Devices*, 40(11) (1993) 2011-2017.
[17] C. Bae, "GaN-dielectric interface formation for gate dielectrics and passivation layers using remote plasma processing", Ph.D. Thesis, North Carolina State University, (USA) (2003).
[18] K. Ohnishi, and K. Miura, *Electron. and Commun. in Japan,* part 2, 75(4) (1992) 52-59.
[19] C.L. Wilson, *IEEE Trans. Electron. Devices*, 27(12) (1980) 2262-2267.

Appendix

Fast ramp (1MV/s) C-V tracer circuit with a snapshot of the CRO screen

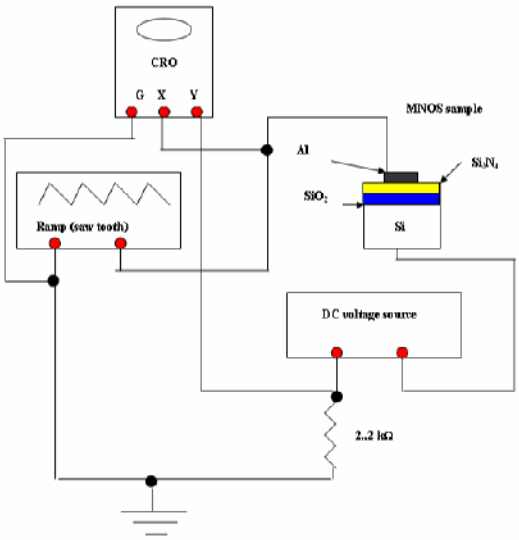

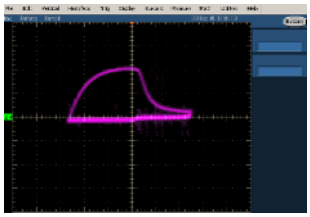

The sweep rate $\alpha = \frac{dv}{dt}$ **=constant** **(a1)**

The capacitance $C = \frac{dq}{dv} = \frac{dq}{dt}\frac{dt}{dv} = \frac{i}{\alpha}$ **(a2)**

Where i is the instantaneous current, hence the i-v curve shown on the CRO screen can be converted into C-V curve using Eq. (a2)

Fabrication and Characterization of InZnO TFTs Grown on Transparent Conductive Oxide Substrate by DC Sputtering Technique

Moath N. Hussain
Jasim M. Abdul-Jabbar

[1] *Department of Electronic and Communications Engineering, College of Engineering, University of Basrah, Basrah, Iraq*

In this work, depletion-mode transistors were made of InZnO thin films prepared and grown on transparent conductive substrates by DC sputtering technique. The SiO_2-In_2O_3-ZnO system and N_2 plasma incorporated InZnO film were grown to get a better controllability of the carrier concentration during the film growth. Hydrogen plasma and oxygen plasma effects on the TCO films and the TFTs were investigated. Devices were simulated in a device model to extract the parasitic parameters. The depletion-mode TFTs have been fabricated successfully on glass by using InZnO films as the channel layers.

***Keywords*:** InZnO films, Thin film transistor, TCOs, DC sputtering
Received: 22 December 2009, **Revised**: 04 February 2010, **Accepted**: 11 February 2010

1. Introduction

Flexible electronics is emerging rapidly [1,2]. Theses devices have the advantages such as low profile, light weight, small size, and better performance. In displays, thin film transistors (TFTs) are used as switching components in the active-matrix over a large area. Currently, liquid crystal displays (LCDs) mostly use amorphous Si as the channel.in TFTs. However, due to the low mobility (<1cm^2/Vs) and high process temperature (350°C), amorphous Si-TFTs are not available for high resolution displays on cheap plastic substrates. Organic TFTs have very low mobility (<1cm^2/Vs) and may have reliability concerns [3]. Oxide-based TFTs have at least 1 order higher mobility (10~50cm^2/Vs) [4] than amorphous Si-TFTs and organic TFTs and can be deposited at room temperature. The high mobility of oxide-based TFTs, make them available for high resolution displays and can integrate switching TFTs in the active-matrix and driver-integrated circuits (driver ICs) on the same plastic substrate, which can reduce cost and provide a more compact display. Besides, oxide-based TFTs have other advantages such as room temperature deposition, higher transparency, better smoothness, etc. [5]. The oxide-based TFTs have a great potential to realize a roll-to-roll display. If this technology can be realized, it may not only replace the current amorphous Si-TFTs for LCDs, but will also create new applications on various sets such as heads-up, windshield, electronic books or light weight computers for soldiers in the battle field and eventually change the whole display industry.

In this study, we fabricated TFTs by sputtering InZnO and InGaZnO on hard (glass) and flexible (plastic) transparent substrates. Depletion mode and enhancement mode field effect transistors will be fabricated. The study will include device designs, materials tuning, process developments, device characterization, device simulation, device reliability test, and device circuit demonstration. The study will cover the whole course of the device development.

TCOs are composed of post-transition metal oxides with outer major quantum number nγ4. These TCOs exhibit n-type carriers [6]. Oxygen vacancies dominate the carrier concentration in these TCO films. For these TCOs, the mobility is still close to that of the polycrystalline even in the amorphous material. It is very different fromα-Si, which has a extremely low mobility (<1cm^2/Vs) in amorphous type comparing to the several orders higher mobility in polycrystalline (30-300cm^2/Vs) or crystalline (>1000cm^2/Vs) [3]. Although there is more than one mechanism explaining the conduction behavior for these TCOs, the most widely accepted theory of carrier transport is the s orbitals overlapping of these transition metal atoms [6].

Many groups reported oxide based TFTs using InZnO, GaZnO, ZnO, SnO_2, In_2O_3 as channel layers fabricated on glass [7-10]. However, few of them are reported on organic flexible transparent substrates. In recent years, α-

 ISSN 1813-2065 Printed in IRAQ

Si TFTs have been fabricated a lot on organic substrate such as PET (polyethylene terephthalate) [11]. Recently, an enhancement mode TTFT using IGZO as the channel layer and Y_2O_3 as the gate dielectric fabricated on a PET substrate was reported [12-14]. The TFT has a field effect mobility of 10cm^2/Vs, threshold voltage 1.2V, on-off ratio >10^6, subthreshold voltage swing ~0.2V/decade. It shows the TCO type TFTs have great potential to beat theα-Si TFTs (low mobility <1cm^2/Vs, high temperature 350°C) and organic TFTs (low mobility <1cm^2/Vs) [3] not only in electrical properties, but also in optical properties, ease of processing, and cost.

Currently, two different technologies are used to fabricate TFTs on plastics. The first one is to deposit films and do processes directly on the plastics [15]. The other one is to fabricate TFTs on rigid glass first, then etch off the substrate glass and paste the flexible plastics onto the TFTs [16]. The second one can avoid high temperature and stress caused by film deposition. However, our InZnO and InGaZnO TFTs are fabricated in a room temperature process, so we can use the direct process approach.

2. Experiment

We plan to fabricate the depletion mode TTFTs as shown in Fig. (1a). The gate dielectrics will be SiO_2, SiN_x or Sc_2O_3. Channel layers will be InZnO or InGaZnO. Device performance will be compared for different structures. Eventually, a fully transparent TFT will be fabricated on a flexible transparent substrate, PET.

We have already fabricated depletion mode thin film transistors using InZnO as the channel layer on glass substrates as depicted in Fig. (1b). This is the first report of depletion mode TFTs made of InZnO film in channel layer [17]. The InZnO films were deposited near room temperature by rf magnetron sputtering using 4in. diameter targets of In_2O_3 and ZnO [18]. The working pressure was varied from 2-15mTorr in a mixed ambient of O_2/Ar. The percentage of O_2 in the mixture was varied from 0-3%. At a percentage of 2.5%, we obtained films with carrier concentration of ~10^{18}cm^{-3} and electron mobility of 17cm^2.V^{-1}.s^{-1} obtained from Hall measurements. The partial pressure of oxygen during the sputter deposition was found to be the dominant factor controlling the conductivity of the films. The sputtering power on the targets was held constant at 125W, leading to compositions of the films measured by x-ray fluorescence spectroscopy of In/Zn=0.5 in atomic ratio. The typical thickness of the InZnO films deposited was 150nm, with a root mean square roughness of 0.4nm measured over a 10x10μm^2 area by Atomic Force Microscopy. The films were amorphous as determined by x-ray diffraction and showed optical transmittance of ~80% in the visible range.

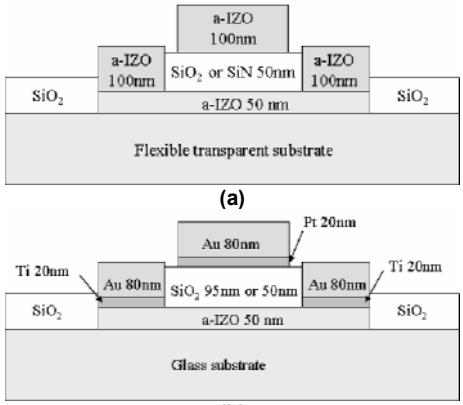

Fig. (1) (a) Schematics of the fully transparent D-Mode TFTs on flexible transparent substrate. (b) D-Mode TFTs on glass

As described in the previous section, the InZnO film was deposited in the sputtering machine with two targets, ZnO and In_2O_3, together with O_2 and Ar gas in the chamber. The O_2/Ar ratio decides the carrier concentration in the InZnO film. Here we plan to use N_2/O_2/Ar gas mixture to deposit InZnO film. The reasons to use N_2 is because in the plasma, N_2 will convert to N_2^+, which may replace O and bond with In. This was investigated in forming p-type ZnO [19]. We know the carriers in the InZnO result from the non-stoichiometry, which means the lack of oxygen allows some indium atoms that are not bonded with oxygen atoms to release electrons to the conduction band. That is why when the O_2/Ar ratio change during InZnO film deposition, the carrier concentration will also change. Higher O_2/Ar ratio leads to a decrease in the number of oxygen vacancies, which also means the carrier concentration decreases [18]. When removing one oxygen atom from the indium, one oxygen vacancy is created. In is a big atom and tends to lose electrons. Oxygen is a small atom and tends to get electrons from the In. ZnO acts as a stabilizer in the In_2O_3 matrix. That's why InZnO and GaZnO both have lower sensitivity of O_2/Ar ratio to carrier concentration than ZnO [10]. Since the oxygen has a higher electronegativity than nitrogen, oxygen can form a strong ionic bond with In. This means when removing or adding a certain amount of oxygen or nitrogen bonded with indium, oxygen will produce a larger change in carrier concentration than nitrogen. This means nitrogen can reduce the sensitivity of O_2/Ar ratio to carrier concentration. The second reason is, due to the previous reason, nitrogen may improve the device reliability. A reliability issue is one of the reasons why GaInZnO was developed [14]. We

may provide another view to do the same thing by an easier method.

Ga_2O_3 introduced into the In_2O_3-ZnO system to form the InGaZnO was reported as providing a better stabilization in TFTs than InZnO [14]. Ga was chosen because it has an atomic radius close to In. The introduction of Ga into the InZnO reduces the electron concentration and mobility. The highest carrier concentration of InGaZnO is around ~10^{19}cm^{-3} [12] which is smaller than that of InZnO (~10^{21}cm^{-3}) [10]. The reduction in carrier concentration is not bad because for the channel layer, 10^{18}~10^{16}cm^{-3} is enough for both depletion and enhancement mode TFTs. Although carrier concentration in InZnO can also be adjusted by O_2/Ar ratio, the carrier concentration change in the InZnO film is dramatic ranging from 10^{18} to 10^{16}cm^{-3} in a small O_2/Ar ratio region [18]. Ga not only reduces carrier concentration, but also reduces the sensitivity of the carrier concentration to the O_2/Ar ratio [10,12]. It is good for controlling the carrier concentration. However, in the mean time, the reduction in mobility is not welcome. It is interesting to introduce another oxide into the InZnO system to stabilize the oxide system and the mobility. The idea is to incorporate a smaller atom and in the mean time, oxide formed by this atom has E_g>3eV. SiO_2 fits these requirements. Si can easily bond with oxygen to reduce sensitivity of the carrier concentration to the O_2/Ar ratio during film deposition. Also, due to the smaller radius of Si than Ga, In atoms still can keep their s orbitals overlapped. This means the mobility may not be degraded too much.

Due to the different interfaces that may form between InZnO and various dielectrics, it is necessary to use different dielectrics such as SiO_2, SiN, and Sc_2O_3 as the gate dielectrics in the TFTs and compare the device performance.

O_2 plasma can obviously decrease the surface carrier concentration of the InZnO film due to the annihilation of the oxygen vacancies. This might help to reduce the surface leakage and then improve on/off ratio if the surface leakage dominates the leakage current, especially for the depletion mode FET. H^+ was reported to be implanted into the CdO-CeO_2 film and act as a shallow donor [20]. We believe that H_2 plasma can also create a donor in InZnO film. One very interesting experiment is that to be easier to control the carrier concentration by hydrogen plasma if we introduce hydrogen into an InZnO film, which had been deposited under a high O_2/Ar ratio. Due to the very small size of the hydrogen, it should not reduce the hall mobility of the InZnO film because it will not inhibit the overlap of the 5s orbitals of In.

After we successfully fabricate the D-mode FETs, we can start to make a ring oscillator using these TFTs. The reliability test will include (i) current stress in room temperature and high temperature (ii) thermal shock and bending test. These tests will be applied to the TCO films and devices on both glass and PET. The device will also be measured for the s parameters and be simulated to extract the parasitic parameters of the D-mode FETs. We have already performed the simulation for the D-mode InZnO TFTs, which will be mentioned in the latter section. TFTs made of InZnO, InGaZnO will be compared and discussed.

An Agilent 4156 parameter analyzer and Agilent E8361 network analyzer will be used to characterize the device dc and rf performance, respectively.

3. Results and Discussion

Top-gate-type TFTs using a-InZnO channels and 50nm or 95nm thick SiO_2 gate insulators deposited by plasma enhanced chemical vapor deposition were fabricated as shown schematically in Fig. (1a). Figure (2) shows the top-view of the TFT. The gate dimension is 36μm×100μm. The InZnO film deposited in 2.5% O_2/Ar ratio has a carrier concentration about 10^{18}cm^{-3} [18]. The whole process was done without heating the substrates, making the entire process consistent with typical continuous-use temperatures of commercial plastic films for electronic devices.

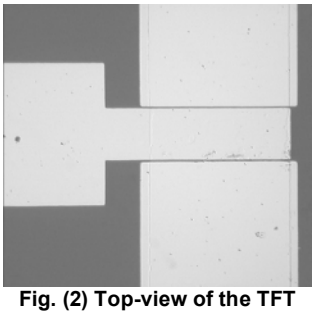

Fig. (2) Top-view of the TFT

Figure (3) shows I_{DS}-V_{DS} characteristics from InZnO transistors with 50nm thick SiO_2 gate dielectric. The transistor operates in depletion-mode with an appreciable drain current at zero gate voltage and exhibits excellent drain current saturation.

Figure (4) shows I_{DS} and g_m as a function of V_{GS} for a device with 50nm SiO_2 gate. The sub-threshold voltage swing was 1.9V/decade and the device had a threshold voltage of -6.5V.The latter is the gate voltage at the onset of the initial sharp increase in current in log(I_D)-V_{GS} characteristics. The drain current on-to-off ratio was >10^6. These results are competitive with past results on TFTs using room temperature sputter deposited amorphous $InGaZnO_4$ as the channel

 ISSN 1813-2065 Printed in IRAQ

material [5]. The field-effect mobility was of ~4.5cm^2.V^{-1}.s^{-1}.

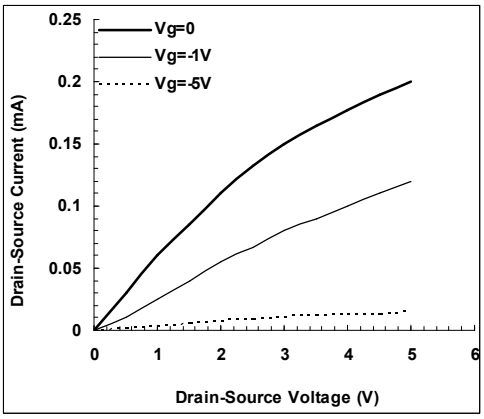

Fig. (3) I_{DS}-V_{DS} characteristics from InZnO transistors with 50nm thick SiO_2 gate dielectric

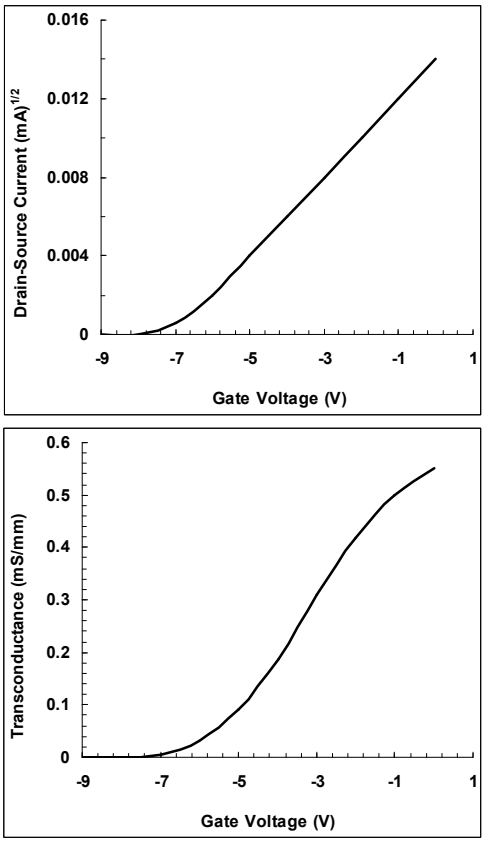

Fig. (4) Drain-source current (I_{DS}) and transconductance (g_m) as a function of V_{GS} for a device with 50nm SiO_2 gate

The gate I-V characteristics from devices with two different gate dielectric thicknesses are shown in Fig. (5). The leakage current is very small, in the 10^{-10}A range, for both gate thicknesses and demonstrates that the low temperature deposition process produces acceptable quality SiO_2 for TFT applications. The threshold voltage was decreased to -5.5V for the thicker dielectric and the slope of the sub-threshold voltage swing was 0.87V/decade for the 95nm thick dielectric.

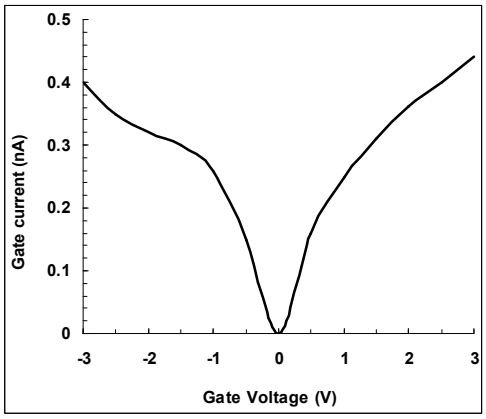

Fig. (5) The gate leakage current characteristics of the devices with two different gate dielectric thicknesses

Top-gate TFTs using 50nm of α-InZnO channels and 12.5nm-thick SiN_x gate insulators deposited by chemical vapor deposition (CVD) were fabricated as shown similarly in Fig. (1b). The gate dimension is 1μm×200μm. The SiN_x layer was deposited without heating the substrates. In addition, the SiN_x gate dielectric provided superior stability of device performance relative to SiO_2 deposited under the same conditions [17]. Specific contact resistance and sheet resistance from the linear transmission line measurements were $7\times10^{-5}\Omega.cm^2$ and 0.9MΩ/sq, respectively. Figure (6) shows typical drain current versus drain voltage, I_{DS}-V_{DS}, characteristics from the InZnO transistors.

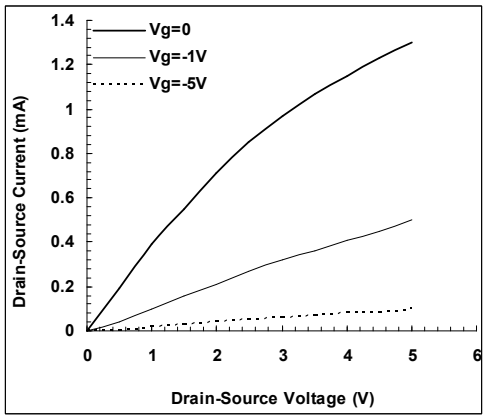

Fig. (6) Typical drain current versus drain voltage, I_{DS}-V_{DS}, characteristics from the InZnO transistors

Figure (7) shows drain current, I_{DS}, and transconductance, g_m, as a function of V_{GS} for an InZnO TFT. A maximum transconductance of 7.5mS/mm was obtained at I_{DS}=1.35mA, V_g=0V and V_d=5V. This is the highest transconductance ever reported for InZnO based TFTs. The transistor has a low threshold voltage of -2.5V. The drain current on-to-off ratio was >10^5. The

gate leakage is about 10^{-10}A~10^{-11}A. The field-effect mobility is 14.5cm^2.V^{-1}.s^{-1}.

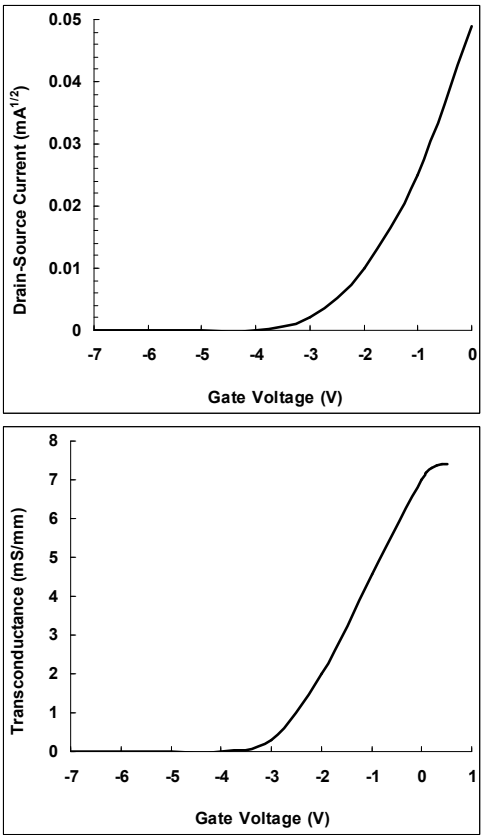

Fig. (7) drain current (I_{DS}) and transconductance (g_m) as a function of V_{GS} for an InZnO TFT

The measured s-parameters, estimated h_{21} and unilateral power gain of a typical InZnO TFT are illustrated in Fig. (8) and Fig. (9), respectively. The TFT was biased at drain and gate voltage of 3V and 0V, respectively during the s-parameter measurements. Unity gain cut-off frequency and maximum frequency of oscillation of 180MHz and 155MHz, respectively, were achieved.

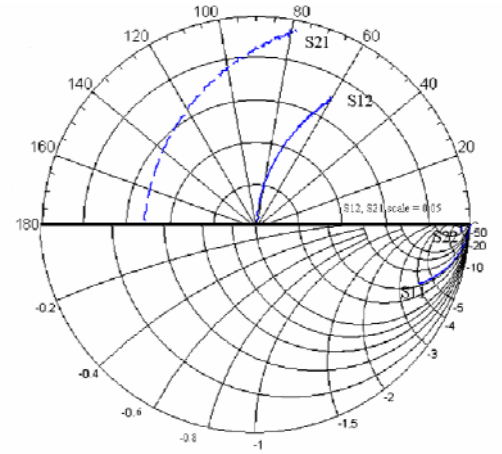

Fig. (8) The measured s-parameters of a typical InZnO TFT

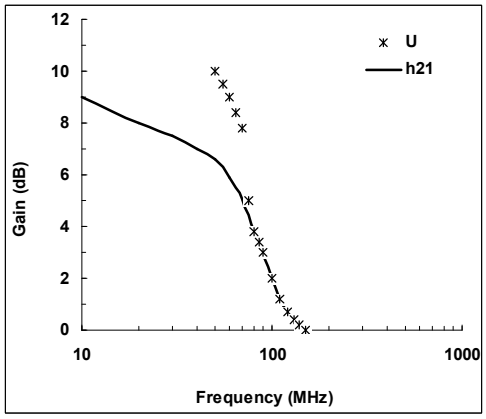

Fig. (9) The estimated (h_{21}) and unilateral power gain (U) of a typical InZnO TFT

A simplified equivalent T-model for the InZnO TFT, as shown in Fig. (10), was used to extract the device parameters. The extracted device parameters are listed in Table (1). The extracted source and drain resistance were consistent with the estimated resistance based on the transmission line measurements and drain I-V characteristics. The simulated intrinsic transconductance was very close to the measured extrinsic transconductance. The low cut-off frequency of the InZnO was limited by the fairly long transit time, 16ps, low transconductance, and high parasitic resistances, which were results of the low mobility and saturation velocity of the α-InZnO channel layer. However, this MHz-range switching performance is sufficient for many display applications.

An amorphous or polycrystalline Si:H layer as the channel have been commonly used for most conventional TFTs in display applications. The standard Si-based TFTs have drawbacks such as light sensitivity, light-induced degradation and low field effect mobility (<1cm^2/Vs) [3]. Therefore, Si:H TFT devices reduce the efficiency of light transmittance and brightness. Besides, both amorphous and polycrystalline Si:H TFTs require relatively high process temperatures (350°C and 450°C, respectively) [3] making it difficult to fabricate these TFTs on plastics. One of the methods to increase the efficiency and avoid high temperature is to use amorphous transparent oxides for the channels and electrodes, and fabricate TFTs at room temperature. Table (1) shows the major differences among α-InZnO, α-Si, and polycrystalline Si. Obviously, α-InZnO has the advantages of high field effect mobility, high transparency, room temperature compatible processing, large area deposition by sputtering, plastics substrate available, and is a cheaper process [3].

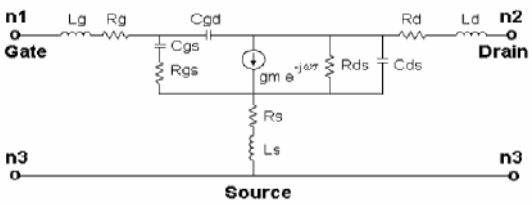

Fig. (10) A simplified equivalent T-model for the InZnO TFT

Table (1) Materials for TFTs used in display applications

Film type	α-InZnO Amorphous	α-Si Amorphous	Poly-Si Polycrystalline
Field effect mobility ($cm^2V^{-1}s^{-1}$)	10-50	0.5-1	30-300
Process temperature (°C)	20	350	450
Transparency (%)	>80	<20	<20
Substrate	Glass plastics	Low cost glass	Quartz

4. Conclusion

In this proposal, InZnO and InGaZnO were used as channel layers to fabricate depletion-mode TFTs and ring oscillators on glass and flexible transparent substrate (PET). The SiO_2-In_2O_3-ZnO system and N_2 plasma incorporated InZnO film were grown to get a better controllability of the carrier concentration during the film growth. Hydrogen plasma and oxygen plasma effects on the TCO films and the TFTs were investigated. The device reliability were tested to compare the effects from different TCO films and process treatments. Devices were simulated in a device model to extract the parasitic parameters. Devices were characterized in DC performance. The depletion-mode TFTs have been fabricated successfully on glass by using InZnO films as the channel layers.

References

[1] K.J. Allen, *Proc. IEEE*, 93 (2005) 1394.
[2] K. Jain *et al.*, *Proc. IEEE*, 93 (2005) 1500.
[3] Y. Sun and J.A. Rogers, *Adv. Mater.*, 19 (2007) 1897.
[4] H.C. Pan *et al.*, *J. Vac. Sci. Technol.*, A 23 (2005) 1187.
[5] T. Sasabayashi *et al.*, *Thin Solid Films*, 445 (2003) 219.
[6] M. Orita *et al.*, *Phil. Mag. B*, 81 (2001) 501.
[7] N.L. Dehuff *et al.*, *J. Appl. Phys.*, 97 (2005) 064505.
[8] R.E. Presley *et al.*, *J. Phys. D: Appl. Phys.*, 37 (2004) 2810.
[9] Dhananjay and C.W. Chu, *Appl. Phys. Lett.*, 91 (2007) 132111.
[10] R. Martins *et al.*, *J. Appl. Phys.*, 101 (2007) 044505.
[11] A. Sazonov and C. McArthur, *J. Vac. Sci. Technol.*, A 22 (2004) 2052.
[12] H. Hosono, *J. Non-Cryst. Solids*, 352 (2006) 851.
[13] K. Nomura *et al.*, *Jpn. J. Appl. Phys.*, 45 (2006) 4303.
[14] T. Kamiya *et al.*, *J. Electroceram.*, 17 (2006) 267.
[15] M.J. Lee, C.P. Judge and S.W. Wright, *Solid-State Electronics*, 44 (2000) 1431.
[16] K. Takechi *et al.*, *IEEE. Trans. Semi. Manuf.*, 18 (2005) 384.
[17] Y.-L. Wang *et al.*, *Appl. Phys. Lett.*, 90 (2007) 1.
[18] W. Lim *et al.*, *Electrochem. Solid-State Lett.*, 10 (2007) H267.
[19] C.L. Perkins *et al.*, *J. Appl. Phys.*, 97 (2005) 034907.
[20] S. Narushima *et al.*, *J. Non-Cryst. Solids*, 374 (2000) 313.

Paul A. Webb
Edward A. Essex

Cooperative Research Centre for Satellite Systems, Department of Physics, La Trobe University, Bundoora, Victoria 3083, Australia

Experimental Observations and Modelling of Electron Density of the Plasmasphere

The increasing use of Global Positioning System (GPS) satellites to determine the Total Electron Content (TEC) of the ionosphere has led to the question; what is the effect of the plasmasphere on these results? To estimate the size of this contribution, the Global Plasmasphere Ionosphere Density (GPID) model has been developed. This paper gives a brief overview of the GPID model, and comparisons between GPID TEC predictions and measurements from GPS receivers on board the Oersted and GFO Low Earth Orbit (LEO) satellites.

Keywords: Plasmasphere, Electron density, Global positioning system, Modelling
Received: 18 December 2009, **Revised**: 14 January 2010, **Accepted**: 21 January 2010

1. Introduction

The plasmasphere is a body of cold dense plasma located above the ionosphere, which extends out to a distance of four to six Earth radii. It consists primarily of H^+ produced in the topside ionosphere, which have been ejected outwards by the dominant heavier O^+ through ambipolar diffusion. At low and mid latitudes the magnetic field lines are closed and the upward flowing H^+ become trapped, collecting in a 'reservoir' of plasma that forms the plasmasphere.

A major data source used to investigate these ionized regions comes from studying their effects on radio signals transmitted to the ground from satellites in the Global Positioning System (GPS) constellation, orbiting at an altitude of 20,200 km. The increasing use of GPS radio signals to study the ionosphere has necessitated the development of a method to estimate the plasmaspheric contribution, so that if required it can be removed. Previous research has shown that the contribution from the plasmasphere amounts to ~10% of the total delay in a GPS signal during the day, and 30-35% at night [1]. Figure (1) shows the location of the GPS orbital plane and the electron densities along a magnetic longitude 'slice', calculated by the model to be discussed.

The time delay introduced in to a GPS signal is proportional to total plasma traversed along the signals ray path. Called the Total Electron Content (TEC), it is equal to the integral of the electron density multiplied by the distance. TEC is measured in TEC units (TECU), where one TECU is 10^{16} electrons/m^2.

The observed electron densities in the plasmasphere are one to four orders in magnitude less than the ionosphere. The greater distance travelled through the plasmasphere can partially negate this difference, so that the net contributions are of similar magnitude. The question is, how does the plasmaspheric TEC vary as a function of time and line of sight of the observation?

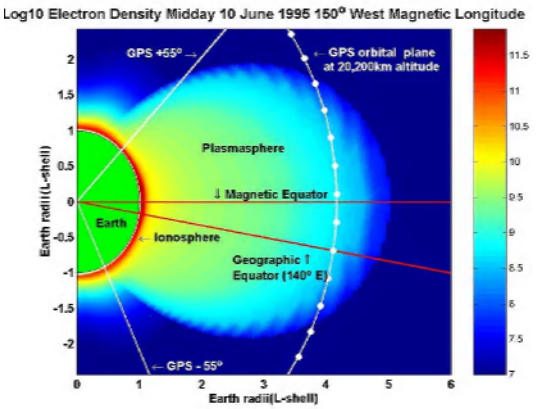

Fig. (1) Example of an Ionosphere - Plasmasphere density slice and the location of the GPS orbital plane.

2. Global Plasmaspheric Ionospheric Density model

To estimate the plasmaspheric contribution, the Global Plasmasphere Ionosphere Density (GPID) model has been developed. GPID is a global dynamic model that runs on a desktop PC. The major aim of GPID is to calculate the electron densities in the ionosphere and plasmasphere quickly and accurately, up to an altitude of 36,000km. GPID is a theoretical model that uses a simplified physical representation of the H^+ and O^+ distributions in a magnetic flux tube aligned along a given magnetic field line. GPID primary parameter of interest is the total number of H^+ in a given magnetic flux tube. From this other parameters, such as the ion densities, can be determined.

The ion density profiles are obtained by using diffusive equilibrium throughout the plasmasphere and chemical equilibrium in the

ionosphere, with the two being combined in the topside ionosphere. By including ionospheric H^+ flows and chemical processes, the temporal variation in the flux tubes H^+ total content can be determined. For details, see [2].

The approach used by GPID to generate ion density profiles is centred on reproducing profiles obtained from the more physically complete Field Line Interhemispheric Plasma (FLIP) plasmasphere model [3]. Figure (2) shows an example of the excellent comparisons than can be obtained between a FLIP profile and the GPID equivalent, when both models have the same equatorial H^+ density. Note that GPID uses the International Reference Ionosphere (IRI) [4] to determine the electron density below 50 km above the local HmF2, and that in Figure 2 the option to force FLIP to reproduce the IRIs HmF2 and NmF2 was selected.

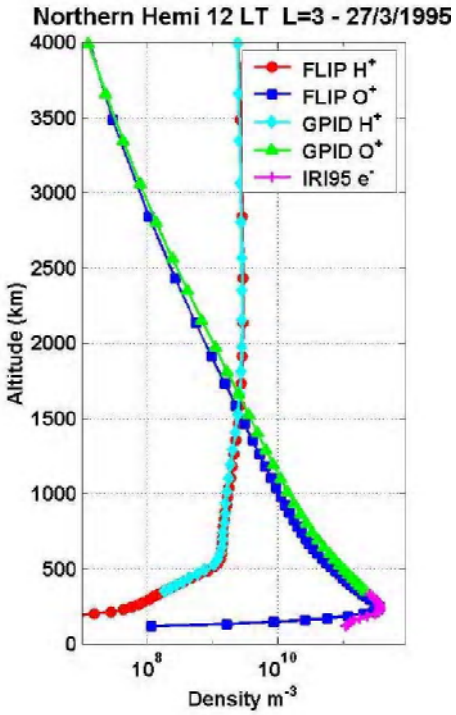

Fig (2) Example of FLIP - GPID ion density profile comparison

Figure (3) is an example of FLIP and GPID refilling predictions of a depleted magnetic flux tube. GPIDs initial tube content was set equal to the FLIP value at the 24 hour point, and then modelled separately. Very good agreement is obtained between the two models. The FLIP simulation took some 30min to run on a VAX Alpha computer using 15min time steps, while the GPID run took just under one minute using one hour time steps on a 550 MHz PC, i.e. GPID was roughly 6 times faster. The drop in tube content and density around the 310 hour mark was caused by a Kp=5 magnetic storm.

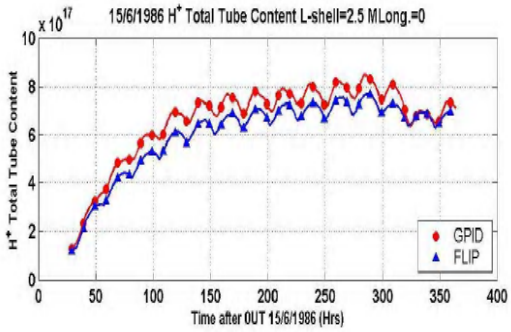

Fig. (3) Example of refilling comparison between GPID and FLIP

GPID obtains a global representation of the plasmasphere by following the dynamic evolution and motion of some 3000 magnetic flux tubes surrounding the Earth. The flux tube motion is controlled by geomagnetic storm activity, measured by the K_p index. During periods of increased K_p the plasma in the outer magnetic flux is swept away from the Earth, depleting the outer plasmasphere. When K_p decreases after a storm, the depleted outer tubes start to refill with plasma. By following this continuous cycle, the global evolution of the plasmasphere can be modelled. The results in the following sections were obtained from this full model.

3. Problems with comparing GPID TEC to ground based GPS observations

TEC measurements made using ground based GPS receivers have the fundamental problem that unless another separate ionospheric measurement can be made, then it is not possible to separate the ionospheric and plasmaspheric contributions. As shown in Fig. (4), different altitude segments make different contributions to the TEC, depending on the magnetic latitude. The ionosphere contributes the majority of the TEC observed, and the plasmaspheric contribution is centred on the magnetic equator. GPID uses the IRI to determine electron densities within the ionosphere. The IRI is based on monthly average observations, and so does not reproduce the daily observed ionospheric variations of ~±25% [5]. Comparing GPID TEC to observations by ground based receivers is therefore likely to produce large differences, unless results are averaged over a period of the order of a month.

4. Getting on top of the problem - GPS receivers on Low Earth Orbit Satellites

One way to make daily TEC comparisons is to place a GPS receiver on a Low Earth Orbit (LEO) satellite. This removes the bulk of the ionospheric TEC component from high elevation observations taken from the LEO, and this allows the plasmasphere to be observed directly.

Recently, TEC data from two different LEOs has become available for comparison to GPID. It should be noted that while GPID uses the monthly IRI values for the underlying ionosphere, the global motion of the plasmasphere is controlled by K_p that is followed at 3 hourly intervals. Hence, the day to day TEC variations measured by the LEOs should be predicted, on a global scale, by GPID.

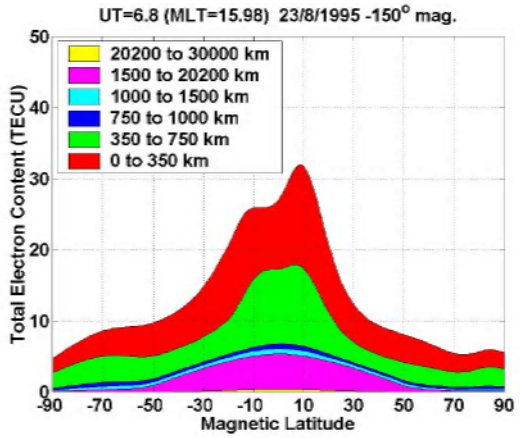

Fig. (4) Afternoon GPID example of the TEC altitude band contributions, as a function of magnetic latitude

Oersted is a 65 kg Danish LEO that was launched in early 1999 and is currently in near polar orbit with apogee 865 km and perigee 649 km. Oersted is run by the Danish Meteorological Institute (DMI), who provided the data presented here. Oersted's main boom failed to deploy properly after launch, resulting in the incorrect positioning of the GPS receiver's antenna. As a consequence, the on board GPS receiver is unable to measure absolute TEC, only relative TEC. This allows it to observe changes in TEC, but a constant TEC offset is required to give absolute measurements. The offset is a single TECU value for each continuous observation of a particular GPS satellite by Oersted, with a given observation being broken when signal drop out occurs. Oersted has made continuous TEC measurements from a single GPS satellite for periods of over two hours. Ironically, this ability to track a single GPS satellite for this length of time is due to the incomplete deployment of the boom, which resulted in the GPS antenna looking roughly 90° off centre relative to its direction of motion.

Figure (5) shows the orbital locations from 19th November 2009, when Oersted tracked a single GPS satellite for over two hours. Note the GPS satellite is roughly at right angles to the direction of motion of the polar orbiting Oersted. The TEC from this example is shown in Fig. (6). One way to estimate the required Oersted offset is to fit its observations to the GPID prediction. A least squares fit is done to the 15 smallest GPID TEC values for a given Oersted profile, since these most likely correspond to direct plasmaspheric TEC observations. Large TEC values will occur along lines of sight that pass near or through the ionosphere, producing ionospheric occultations. The occultation TECs will depend primarily on the monthly averaged IRI electron densities, and therefore at a daily level are potentially in error.

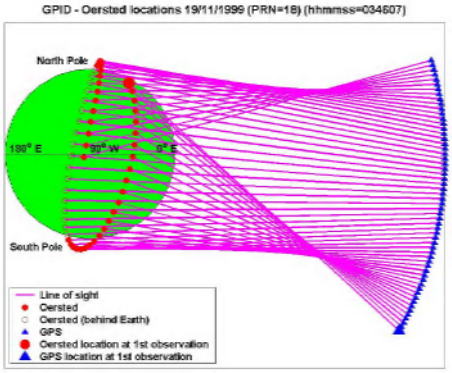

Fig. (5) Example of orbital location of the satellites during a continuous GPS satellite track by Oersted

Shown in Fig. (6) is an example of Oersted TEC profile fitted to the GPID prediction. As this shows, the GPID is successfully reproducing the major TEC features that were observed by Oersted. GPS TEC data have been provided from the U.S. Navy GFO (GEOSAT Follow On) LEO. GFO is a 370 kg LEO in a near polar orbit, at 800 km altitude. The GFO TEC measurements are absolute, and so data from observations of different GPS satellites can be combined and compared directly to GPID. The only unknown parameter is the GFO GPS receiver bias, which can be estimated by comparing the GPID predicted TEC with the GFO observations. A plot of GFO TEC *vs.* GPID TEC should return a slope of one, and a TEC offset corresponding to the receiver bias. The GFO data are from the 12th October 2009. Due to the near polar orbit of GFO, the majority of the GPS observations occur either near local midnight or midday. A linear fit to the full data set for the entire day returns a slope of 0.8, not the expected 1.0.

The variation with masking angle in the day and night slopes, and the fit to the complete data set, is shown in Fig. (7). While this indicates the obtained slope sometimes differs by up to 20% from unity during the day, overall the fits are much closer to 1.0 than the full fit, especially at night. Further, it should be noted that the weighted mean of the day and night fits are almost within one or two standard deviations of 1.0. Why this occurs is not currently known, but is currently being investigated.

ISSN 1813-2065 Printed in IRAQ

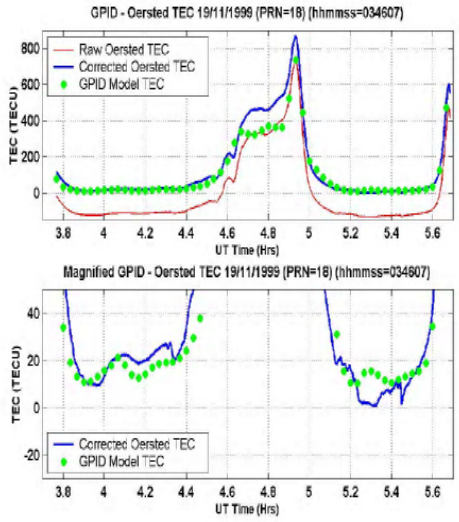

Fig. (6) Example of Oersted TEC and the GPID prediction, corresponding to the orbits shown in Fig. (5) 'Raw' is the relative TEC, while 'Corrected' denotes the fitted TEC with a 134 TECU offset. The lower plot is a magnified version of the upper plot at low TEC values. These TEC observations are direct plasmaspheric observations that contain little or no ionospheric component. This allows experimentally observed plasmaspheric features to be compared to the GPID predictions, which can not be seen in the upper plot because of the scale required to plot the high TEC that occurs due to ionospheric occultations

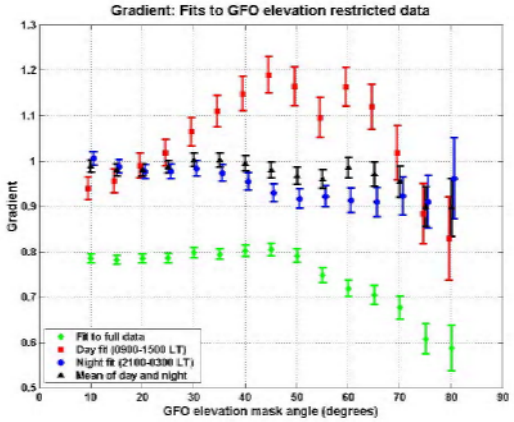

Fig. (7) Variation of fitted slope with masking angle, as observed by GFO on 12th October, 2009

Possible reasons for the apparent separate day and night data sets include on board satellite temperature variations affecting the receiver electronics, to errors introduced in the GPID model coming from incorrect ionospheric predictions from the IRI model. Another reason is that the 12th October 2009 and the several day preceding it where very geomagnetically activity, which may be partially responsible for the observed results. In the near future it is planned to look at GFO data measurements from several other days to see if these trends continue.

5. Conclusion

The aim of this short paper has been to introduce the reader to the GPID model. GPID is a flexible application, able to provide results in many different situations. While only several limited comparisons between GPID and LEO based plasmaspheric TEC data has been presented, they show that GPID is generally accurately reproducing various observed features of the plasmasphere. The results also show that work is till required to reconcile the differences between GPID and the plasmaspheric observations, such as the day and night discrepancies in the GFO data.

References

[1] J.A. Klobuchar, P.H. Doherty, G.J. Bailey and K. Davies, *Limitations in Determining Absolute Total Electron Content from Dual-Frequency GPS Group Delay Measurements*. Proceedings of the International Beacon Satellite Symposium, University of Wales, Aberystwyth UK, 11-15 July 1994.

[2] P.A. Webb and E.A. Essex, *J. Atmosphere. Solar Terrest. Phys.,* 63(11) (2001) 1249-1260.

[3] M.R. Torr et al., *J. Geophys. Res.*, 95(A12) (1990) 21,147-21,168.

[4] D. Bilitza et al., *Advances in Space Res.*, 13(3) (1993) 3-23.

[5] J.M. Forbes, S.E. Palo and X. Zhang, *J. Atmosphere. Solar Terrest. Phys.,* 62 (2000) 685-693.

THE IRAQI JOURNAL OF APPLIED PHYSICS
EDITORIAL BOARD

COPYRIGHT RELEASE
Iraqi Journal of Applied Physics (IJAP)

We, the undersigned, the author/authors of the article titled
……
……
……
……
……
……
that is presented to the Iraqi Journal of Applied Physics (IJAP) for publication, declare that we have neither taken part or full text from any published work by others, nor presented or published it elsewhere in any other journal. We also declare transferring copyrights and conduct of this article to the Iraqi Journal of Applied Physics (IJAP) after accepting it for publication.

The authors will keep the following rights:
1. **Possession of the article such as patent rights.**
2. **Free of charge use of the article or part of it in any future work by the authors such as books and lecture notes without referring to the IJAP.**
3. **Republishing the article for any personal purposes of the authors after taking journal permission.**

To be signed by all authors:

Signature:……..date: ……..

Printed name: ……

Signature:……..date: ……..

Printed name: ……..

Signature:……..date: ……..

Printed name: ……..

Correspondence address:
……
……
……
Address:……
……
……
Telephone:……..email: ……..

Note: Please complete and sign this form and mail it to the below address with your manuscript

The Iraqi Journal of Applied Physics
P. O. Box 55259, Baghdad 12001, IRAQ
Website: www.ijap.org
Email: editor@ijap.org
Phone: +964 7901274190

IRAQI JOURNAL OF APPLIED PHYSICS

CONTENTS